



Measurement of the total cross section from elastic scattering in pp collisions at $\sqrt{s} = 7$ TeV with the ATLAS detector

ATLAS Collaboration *

CERN, 1211 Geneva 23, Switzerland

Received 25 August 2014; received in revised form 17 October 2014; accepted 21 October 2014

Available online 28 October 2014

Editor: Valerie Gibson

Abstract

A measurement of the total pp cross section at the LHC at $\sqrt{s} = 7$ TeV is presented. In a special run with high- β^* beam optics, an integrated luminosity of $80 \mu\text{b}^{-1}$ was accumulated in order to measure the differential elastic cross section as a function of the Mandelstam momentum transfer variable t . The measurement is performed with the ALFA sub-detector of ATLAS. Using a fit to the differential elastic cross section in the $|t|$ range from 0.01 GeV^2 to 0.1 GeV^2 to extrapolate to $|t| \rightarrow 0$, the total cross section, $\sigma_{\text{tot}}(pp \rightarrow X)$, is measured via the optical theorem to be:

$$\sigma_{\text{tot}}(pp \rightarrow X) = 95.35 \pm 0.38 \text{ (stat.)} \pm 1.25 \text{ (exp.)} \pm 0.37 \text{ (extr.) mb,}$$

where the first error is statistical, the second accounts for all experimental systematic uncertainties and the last is related to uncertainties in the extrapolation to $|t| \rightarrow 0$. In addition, the slope of the elastic cross section at small $|t|$ is determined to be $B = 19.73 \pm 0.14 \text{ (stat.)} \pm 0.26 \text{ (syst.) GeV}^{-2}$.

© 2014 The Authors. Published by Elsevier B.V. This is an open access article under the CC BY license (<http://creativecommons.org/licenses/by/3.0/>). Funded by SCOAP³.

* E-mail address: atlas.publications@cern.ch.

1. Introduction

The total hadronic cross section is a fundamental parameter of strong interactions, setting the scale of the size of the interaction region at a given energy. A calculation of the total hadronic cross section from first principles, based upon quantum chromodynamics (QCD), is currently not possible. Large distances are involved in the collision process and thus perturbation theory is not applicable. Even though the total cross section cannot be directly calculated, it can be estimated or bounded by a number of fundamental relations in high-energy scattering theory which are model independent. The Froissart–Martin bound [1,2], which states that the total cross section cannot grow asymptotically faster than $\ln^2 s$, \sqrt{s} being the centre-of-mass energy, is based upon principles of axiomatic field theory. The optical theorem, which relates the imaginary part of the forward elastic-scattering amplitude to the total cross section, is a general theorem in quantum scattering theory. Dispersion relations, which connect the real part of the elastic-scattering amplitude to an integral of the total cross section over energy, are based upon the analyticity and crossing symmetry of the scattering amplitude. All of these relations lead to testable constraints on the total cross section.

The rise of the pp cross section with energy was first observed at the ISR [3,4]. The fact that the hadronic cross section continues to rise has been confirmed in every new energy regime made accessible by a new pp or $p\bar{p}$ collider (Sp \bar{p} S, Tevatron and LHC) [5–11]. However, the “asymptotic” energy dependence is yet to be determined. A still open question is whether the cross section indeed rises proportionally to $\ln^2 s$ in order to saturate the Froissart–Martin bound or whether the rise has e.g. a $\ln s$ dependence.

Traditionally, the total cross section at hadron colliders has been measured via elastic scattering using the optical theorem. This paper presents a measurement by the ATLAS experiment [12] at the LHC in pp collisions at $\sqrt{s} = 7$ TeV using this approach. The optical theorem states:

$$\sigma_{\text{tot}} \propto \text{Im}[f_{\text{el}}(t \rightarrow 0)] \quad (1)$$

where $f_{\text{el}}(t \rightarrow 0)$ is the elastic-scattering amplitude extrapolated to the forward direction, i.e. at $|t| \rightarrow 0$, t being the four-momentum transfer. Thus, a measurement of elastic scattering in the very forward direction gives information on the total cross section. An independent measurement of the luminosity is required. In this analysis, the luminosity is determined from LHC beam parameters using van der Meer scans [13]. Once the luminosity is known, the elastic cross section can be normalized. An extrapolation of the differential cross section to $|t| \rightarrow 0$ gives the total cross section through the formula:

$$\sigma_{\text{tot}}^2 = \frac{16\pi(\hbar c)^2}{1 + \rho^2} \left. \frac{d\sigma_{\text{el}}}{dt} \right|_{t \rightarrow 0}, \quad (2)$$

where ρ represents a small correction arising from the ratio of the real to imaginary part of the elastic-scattering amplitude in the forward direction and is taken from theory. In order to minimize the model dependence in the extrapolation to $|t| \rightarrow 0$, the elastic cross section has to be measured down to as small $|t|$ values as possible. Here, a fit in the range $0.01 \text{ GeV}^2 < -t < 0.1 \text{ GeV}^2$ is used to extract the total cross section, while the differential cross section is measured in the range $0.0025 \text{ GeV}^2 < -t < 0.38 \text{ GeV}^2$. The determination of the total cross section also implies a measurement of the nuclear slope parameter B , which describes the exponential t -dependence of the nuclear amplitude at small t -values. In a simple geometrical model of elastic scattering, B is related to the size of the proton and thus its energy dependence is strongly correlated with that of the total cross section.

The measurements of the total cross section and elastic scattering reported here are used to determine the inelastic cross section, as the difference between these two quantities. This measurement of the inelastic cross section is compared with a previous measurement by the ATLAS experiment using a complementary method based upon data from a minimum-bias trigger [14]. The ratio of the elastic to total cross section is also derived. In the black-disc limit, the limit in which the proton is completely opaque, this quantity goes at asymptotic energies to 0.5 and thus the measurement is directly sensitive to the hadron opacity. The quantities measured and reported here have also been measured at the LHC by the TOTEM experiment [15,16].

This paper is organized as follows. The experimental setup including a brief description of the ALFA sub-detector is given in Section 2, followed by a short description of the measurement method in Section 3. Section 4 summarizes theoretical predictions and Monte Carlo simulations. The data taking and trigger conditions are outlined in Section 5, followed by a description of the track reconstruction and alignment procedures in Section 6. The data analysis consisting of event selection, background determination and reconstruction efficiency is explained in Section 7. Section 8 describes the acceptance and unfolding corrections. The determination of the beam optics is summarized in Section 9 and of the luminosity in Section 10. Results for the differential elastic cross section are reported in Section 11 and the extraction of the total cross section in Section 12. The results are discussed in Section 13 with a summary in Section 14.

2. Experimental setup

ATLAS is a multi-purpose detector designed to study elementary processes in proton–proton interactions at the TeV energy scale. It consists of an inner tracking system, calorimeters and a muon spectrometer surrounding the interaction point of the colliding beams. The tracking system covers the pseudorapidity range $|\eta| < 2.5$ and the calorimetric measurements range to $|\eta| = 4.9$.¹ To improve the coverage in the forward direction three smaller detectors with specialized tasks are installed at large distance from the interaction point. The most forward detector, ALFA, is sensitive to particles in the range $|\eta| > 8.5$, while the two others have acceptance windows at $|\eta| \approx 5.8$ (LUCID) and $|\eta| \approx 8.2$ (ZDC). A detailed description of the ATLAS detector can be found in Ref. [12].

The ALFA detector (Absolute Luminosity For ATLAS) is designed to measure small-angle proton scattering. Two tracking stations are placed on each side of the central ATLAS detector at distances of 238 m and 241 m from the interaction point. The tracking detectors are housed in so-called Roman Pots (RPs) which can be moved close to the circulating proton beams. Combined with special beam optics, as introduced in Section 3, this allows the detection of protons at scattering angles down to 10 μrad .

Each station carries an upper and lower RP connected by flexible bellows to the primary LHC vacuum. The RPs are made of stainless steel with thin windows of 0.2 mm and 0.5 mm thickness at the bottom and front sides to reduce the interactions of traversing protons. Elastically scattered protons are detected in the main detectors (MDs) while dedicated overlap detectors (ODs) measure the distance between upper and lower MDs. The arrangement of the upper and lower MDs and ODs with respect to the beam is illustrated in Fig. 1.

¹ ATLAS uses a right-handed coordinate system with its origin at the nominal interaction point in the centre of the detector and the z -axis along the beam pipe. The x -axis points from the interaction point to the centre of the LHC ring and the y -axis points upwards. The pseudorapidity η is defined in terms of the polar angle θ as $\eta = -\ln \tan(\theta/2)$.

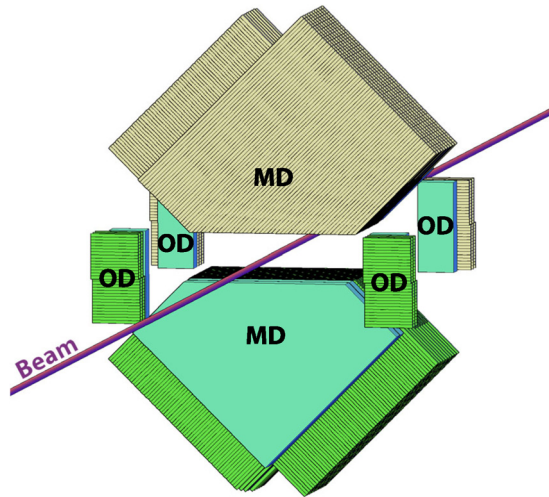


Fig. 1. A schematic view of a pair of ALFA tracking detectors in the upper and lower RPs. Although not shown, the ODs on either side of each MD are mechanically attached to them. The orientation of the scintillating fibres is indicated by dashed lines. The plain objects visible in front of the lower MD and ODs are the trigger counters. For upper MD and the lower ODs they are hidden at the opposite side of the fibre structures.

Each MD consists of 2 times 10 layers of 64 square scintillating fibres with 0.5 mm side length glued on titanium plates. The fibres on the front and back sides of each titanium plate are orthogonally arranged at angles of $\pm 45^\circ$ with respect to the y -axis. The projections perpendicular to the fibre axes define the u and v coordinates which are used in the track reconstruction described in Section 6.1. To minimize optical cross-talk, each fibre is coated with a thin aluminium film. The individual fibre layers are staggered by multiples of $1/10$ of the fibre size to improve the position resolution. The theoretical resolution of $14.4 \mu\text{m}$ per u or v coordinate is degraded due to imperfect staggering, cross-talk, noise and inefficient fibre channels. To reduce the impact of imperfect staggering on the detector resolution, all fibre positions were measured by microscope. In a test beam [17,18] with 120 GeV hadrons, the position resolution was measured to be between $30 \mu\text{m}$ and $35 \mu\text{m}$. The efficiency to detect a traversing proton in a single fibre layer is typically 93%, with layer-to-layer variations of about 1%. The overlap detectors consist of three layers of 30 scintillating fibres per layer measuring the vertical coordinate of traversing beam-halo particles or shower fragments.² Two independent ODs are attached at each side of both MDs, as sketched in Fig. 1. The alignment of the ODs with respect to the coordinate system of the MDs was performed by test-beam measurements using a silicon pixel telescope. A staggering by $1/3$ of the fibre size results in a single-track resolution of about $50 \mu\text{m}$. The signals from both types of tracking detectors are amplified by 64-channel multi-anode photomultipliers (MAPMTs). The scintillating fibres are directly coupled to the MAPMT photocathode. Altogether, 23 MAPMTs are used to read out each MD and its two adjacent ODs.

Both tracking detectors are completed by trigger counters which consist of 3 mm thick scintillator plates covering the active areas of MDs and ODs. Each MD is equipped with two trigger counters and their signals are used in coincidence to reduce noise contributions. The ODs are

² Halo particles originate from beam particles which left the bunch structure of the beam but still circulate in the beam pipe.

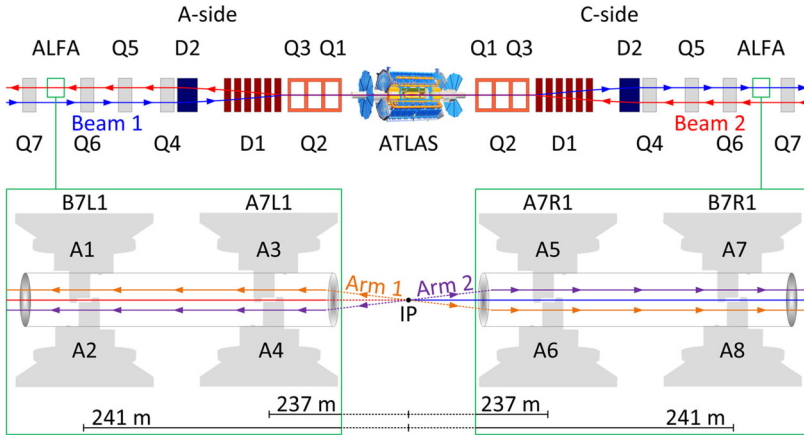


Fig. 2. A sketch of the experimental set-up, not to scale, showing the positions of the ALFA Roman Pot stations in the outgoing LHC beams, and the quadrupole (Q1–Q6) and dipole (D1–D2) magnets situated between the interaction point and ALFA. The ALFA detectors are numbered A1–A8, and are combined into inner stations A7R1 and A7L1, which are closer to the interaction point, and outer stations B7R1 and B7L1. The arrows indicate in the top panel the beam directions and in the bottom panel the scattered proton directions.

covered by single trigger counters and each signal is recorded. Clear-fibre bundles are used to guide all scintillation signals from the trigger counters to single-channel photomultipliers.

Before data taking, precision motors move the RPs vertically in 5 μm steps towards the beam. The position measurement is realized by inductive displacement sensors (LVDT) calibrated by a laser survey in the LHC tunnel. The internal precision of these sensors is 10 μm . In addition, the motor steps are used to cross-check the LVDT values.

The compact front-end electronics is assembled in a three-layer structure attached to the back side of each MAPMT. The three layers comprise a high-voltage divider board, a passive board for signal routing and an active board for signal amplification, discrimination and buffering using the MAROC chip [19,20]. The buffers of all 23 MAPMT readout chips of a complete detector are serially transmitted by five kapton cables to the mother-board. All digital signals are transmitted via a fibre optical link to the central ATLAS data acquisition system. The analogue trigger signals are sent by fast air-core cables to the central trigger processor.

The station and detector naming scheme is depicted in Fig. 2. The stations A7R1 and B7R1 are positioned at $z = -237.4$ m and $z = -241.5$ m respectively in the outgoing beam 1 (C side), while the stations A7L1 and B7L1 are situated symmetrically in the outgoing beam 2 (A side). The detectors A1–A8 are inserted in increasing order in stations B7L1, A7L1, A7R1 and B7R1 with even-numbered detectors in the lower RPs. Two spectrometer arms for elastic-scattering event topologies are defined by the following detector series: arm 1 comprising detectors A1, A3, A6, A8, and arm 2 comprising detectors A2, A4, A5, A7. The sequence of quadrupoles between the interaction point and ALFA is also shown in Fig. 2. Among them, the inner triplet Q1–Q3 is most important for the high- β^* beam optics necessary for this measurement.

3. Measurement method

The data were recorded with special beam optics characterized by a β^* of 90 m [21,22] at the interaction point resulting in a small divergence and providing parallel-to-point focusing in the

vertical plane.³ In parallel-to-point beam optics the betatron oscillation has a phase advance Ψ of 90° between the interaction point and the RPs, such that all particles scattered at the same angle are focused at the same position at the detector, independent of their production vertex position. This focusing is only achieved in the vertical plane.

The beam optics parameters are needed for the reconstruction of the scattering angle θ^* at the interaction point. The four-momentum transfer t is calculated from θ^* ; in elastic scattering at high energies this is given by:

$$-t = (\theta^* \times p)^2, \quad (3)$$

where p is the nominal beam momentum of the LHC of 3.5 TeV and θ^* is measured from the proton trajectories in ALFA. A formalism based on transport matrices allows positions and angles of particles at two different points of the magnetic lattice to be related.

The trajectory $(w(z), \theta_w(z))$, where $w \in \{x, y\}$ is the transverse position with respect to the nominal orbit at a distance z from the interaction point and θ_w is the angle between w and z , is given by the transport matrix \mathbf{M} and the coordinates at the interaction point (w^*, θ_w^*) :

$$\begin{pmatrix} w(z) \\ \theta_w(z) \end{pmatrix} = \mathbf{M} \begin{pmatrix} w^* \\ \theta_w^* \end{pmatrix} = \begin{pmatrix} M_{11} & M_{12} \\ M_{21} & M_{22} \end{pmatrix} \begin{pmatrix} w^* \\ \theta_w^* \end{pmatrix}, \quad (4)$$

where the elements of the transport matrix can be calculated from the optical function β and its derivative with respect to z and Ψ . The transport matrix \mathbf{M} must be calculated separately in x and y and depends on the longitudinal position z ; the corresponding indices have been dropped for clarity. While the focusing properties of the beam optics in the vertical plane enable a reconstruction of the scattering angle using only M_{12} with good precision, the phase advance in the horizontal plane is close to 180° and different reconstruction methods are investigated.

The ALFA detector was designed to use the “subtraction” method, exploiting the fact that for elastic scattering the particles are back-to-back, that the scattering angle at the A- and C-sides are the same in magnitude and opposite in sign, and that the protons originate from the same vertex. The beam optics was optimized to maximize the lever arm M_{12} in the vertical plane in order to access the smallest possible scattering angle. The positions measured with ALFA at the A- and C-side of ATLAS are roughly of the same size but opposite sign and in the subtraction method the scattering angle is calculated according to:

$$\theta_w^* = \frac{w_A - w_C}{M_{12,A} + M_{12,C}}. \quad (5)$$

This is the nominal method in both planes and yields the best t -resolution. An alternative method for the reconstruction of the horizontal scattering angle is to use the “local angle” θ_w measured by the two detectors on the same side:

$$\theta_w^* = \frac{\theta_{w,A} - \theta_{w,C}}{M_{22,A} + M_{22,C}}. \quad (6)$$

Another method performs a “local subtraction” of measurements at the inner station at 237 m and the outer station at 241 m, separately at the A- and C-side, before combining the two sides:

³ The β -function determines the variation of the beam envelope around the ring and depends on the focusing properties of the magnetic lattice.

$$\theta_{w,S}^* = \frac{M_{11,S}^{241} \times w_{237,S} - M_{11,S}^{237} \times w_{241,S}}{M_{11,S}^{241} \times M_{12,S}^{237} - M_{11,S}^{237} \times M_{12,S}^{241}}, \quad S = A, C. \quad (7)$$

Finally, the “lattice” method uses both the measured positions and the local angle to reconstruct the scattering angle by the inversion of the transport matrix

$$\begin{pmatrix} w^* \\ \theta_w^* \end{pmatrix} = \mathbf{M}^{-1} \begin{pmatrix} w \\ \theta_w \end{pmatrix}, \quad (8)$$

and from the second row of the inverted matrix the scattering angle is determined

$$\theta_w^* = M_{12}^{-1} \times w + M_{22}^{-1} \times \theta_w. \quad (9)$$

All methods using the local angle suffer from a poor resolution due to a moderate angular resolution of about 10 μrad . Nevertheless, these alternative methods are used to cross-check the subtraction method and determine beam optics parameters.

For all methods t is calculated from the scattering angles as follows:

$$-t = ((\theta_x^*)^2 + (\theta_y^*)^2) p^2, \quad (10)$$

where θ_y^* is always reconstructed with the subtraction method, because of the parallel-to-point focusing in the vertical plane, while all four methods are used for θ_x^* . Results on σ_{tot} using the four methods are discussed in Section 12.

4. Theoretical prediction and Monte Carlo simulation

Elastic scattering is related to the total cross section through the optical theorem (Eq. (1)) and the differential elastic cross section is obtained from the scattering amplitudes of the contributing diagrams:

$$\frac{d\sigma}{dt} = \frac{1}{16\pi} |f_N(t) + f_C(t)e^{i\alpha\phi(t)}|^2. \quad (11)$$

Here, f_N is the purely strongly interacting amplitude, f_C is the Coulomb amplitude and a phase ϕ is induced by long-range Coulomb interactions [23,24]. The individual amplitudes are given by

$$f_C(t) = -8\pi\alpha\hbar c \frac{G^2(t)}{|t|}, \quad (12)$$

$$f_N(t) = (\rho + i) \frac{\sigma_{\text{tot}}}{\hbar c} e^{-B|t|/2}, \quad (13)$$

where G is the electric form factor of the proton, B the nuclear slope and $\rho = \text{Re}(f_{\text{el}})/\text{Im}(f_{\text{el}})$. The expression for the nuclear amplitude f_N is an approximation valid at small $|t|$ only. This analysis uses the calculation of the Coulomb phase from Ref. [24] with a conventional dipole parameterization of the proton electric form factor from Ref. [25]. The theoretical form of the t -dependence of the cross section is obtained from the evaluation of the square of the complex amplitudes:

$$\begin{aligned} \frac{d\sigma}{dt} &= \frac{4\pi\alpha^2(\hbar c)^2}{|t|^2} \times G^4(t) - \sigma_{\text{tot}} \times \frac{\alpha G^2(t)}{|t|} [\sin(\alpha\phi(t)) + \rho \cos(\alpha\phi(t))] \times \exp\left(\frac{-B|t|}{2}\right) \\ &+ \sigma_{\text{tot}}^2 \frac{1 + \rho^2}{16\pi(\hbar c)^2} \times \exp(-B|t|), \end{aligned} \quad (14)$$

where the first term corresponds to the Coulomb interaction, the second to the Coulomb–nuclear interference and the last to the hadronic interaction. This parameterization is used to fit the differential elastic cross section to extract σ_{tot} and B . The inclusion of the Coulomb interaction in the fit of the total cross section increases the value of σ_{tot} by about 0.6 mb, compared with a fit with the nuclear term only.

The value of ρ is extracted from global fits performed by the COMPETE Collaboration to lower-energy elastic-scattering data comprising results from a variety of initial states [26, 27]. Systematic uncertainties originating from the choice of model are important and are addressed e.g. in Ref. [28]. Additionally, the inclusion of different data sets in the fit influences the value of ρ , as described in Refs. [29,30]. In this paper the value from Ref. [26] is used with a conservative estimate of the systematic uncertainty to account for the model dependence: $\rho = 0.140 \pm 0.008$. The theoretical prediction given by Eq. (14) also depends on the Coulomb phase ϕ and the form factor G . Uncertainties in the Coulomb phase are estimated by replacing the simple parameterization from Ref. [24] with alternative calculations from Refs. [25] and [31], which both predict a different t -dependence of the phase. Changing this has only a minor fractional impact of order 0.01 mb on the cross-section prediction.

The uncertainty on the electric form factor is derived from a comparison of the simple dipole parameterization used in this analysis to more sophisticated forms [32], which describe high-precision low-energy elastic electron–proton data better [33]. Replacing the dipole by other forms also has a negligible impact of order 0.01 mb on the total cross-section determination.

Alternative parameterizations of the nuclear amplitude which deviate from the simple exponential t -dependence are discussed in Section 12.3.

4.1. Monte Carlo simulation

Monte Carlo simulated events are used to calculate acceptance and unfolding corrections. The generation of elastic-scattering events is performed with PYTHIA8 [34,35] version 8.165, in which the t -spectrum is generated according to Eq. (14). The divergence of the incoming beams and the vertex spread are set in the simulation according to the measurements described in Section 5. After event generation, the elastically scattered protons are transported from the interaction point to the RPs, either by means of the transport matrix Eq. (4) or by the polymorphic tracking code module for the symplectic thick-lens tracking implemented in the MadX [36] beam optics calculation package.

A fast parameterization of the detector response is used for the detector simulation with the detector resolution tuned to the measured resolution. The resolution is measured by extrapolating tracks reconstructed in the inner stations to the outer stations using beam optics matrix-element ratios and comparing predicted positions with measured positions. It is thus a convolution of the resolutions in the inner and outer stations. The fast simulation is tuned to reproduce this convolved resolution. A full GEANT4 [37,38] simulation is used to set the resolution scale between detectors at the inner and outer stations, which cannot be determined from the data. The resolution of the detectors at the outer stations is slightly worse than for the detectors at the inner stations as multiple scattering and shower fragments from the latter degrade the performance of the former.

Systematic uncertainties from the resolution difference between the detectors at the inner and outer stations are assessed by fixing the resolution of the detectors at the inner stations either to the value from GEANT4 or to the measurement from the test beam [17,18] and matching the resolution at the outer stations to reproduce the measured convolved resolution. The resolution

depends slightly on the vertical track position on the detector surface; a further systematic uncertainty is assessed by replacing the constant resolution by a linear parameterization. The total systematic uncertainty on the resolution of about $\pm 10\%$ is dominated by the difference between the value from the test-beam measurement and from GEANT4 simulation.

5. Data taking

The data were recorded in a dedicated low-luminosity run using beam optics with a β^* of 90 m; details of the beam optics settings can be found in Refs. [21,22]. The duration of this run was four hours. For elastic-scattering events, the main pair of colliding bunches was used, which contained around 7×10^{10} protons per bunch. Several pairs of pilot bunches with lower intensity and unpaired bunches were used for the studies of systematic uncertainties. The rates of the head-on collisions were maximized using measurements from online luminosity monitors. The run used for data analysis was preceded by a run with identical beam optics to align the RPs.

5.1. Beam-based alignment

Very precise positioning of the RPs is mandatory to achieve the desired precision on the position measurement of 20–30 μm in both the horizontal and vertical dimensions. The first step is a beam-based alignment procedure to determine the position of the RPs with respect to the proton beams. One at a time, the eight pots are moved into the beam, ultimately by steps of 10 μm only, until the LHC beam-loss monitors give a signal well above threshold. The beam-based alignment procedure was performed in a dedicated fill with identical beam settings just before the data-taking run. The vertical positions of the beam envelopes were determined at each station by scraping the beam with the upper and lower RPs in turn.

From the positions of the upper and the lower RP windows with respect to the beam edges, the centre of the beam as well as the distance between the upper and lower pots were computed. For the two stations on side C the centres were off zero by typically 0.5–0.6 mm; for side A both were off by about -0.2 mm. On each side, the distances between the upper and the lower pots were measured to be 8.7 mm for the station nearer to the interaction point and 7.8 mm for the far one. This difference corresponds to the change in the nominal vertical beam widths (σ_y) between the two stations.

The data were collected with the pots at $6.5 \times \sigma_y$ from the beam centre, the closest possible distance with reasonable background rates. With a value of the nominal vertical beam spread, σ_y , of 897 μm (856 μm) for the inner (outer) stations, the $6.5 \times \sigma_y$ positions correspond to a typical distance of 5.83 mm (5.56 mm) from the beam line in the LHC reference frame.

5.2. Beam characteristics: stability and emittance

Beam position monitors, regularly distributed along the beam line between the interaction point and the RPs, were used to survey the horizontal and vertical positions of the beams. The variations in position throughout the duration of the data taking were of the order of 10 μm in both directions, which is equal to the precision of the measurement itself.

The vertical and horizontal beam emittances ϵ_y and ϵ_x , expressed in μm , are used in the simulation to track a scattered proton going from the interaction point to the RPs and therefore to determine the acceptance. These were measured at regular intervals during the fill using a

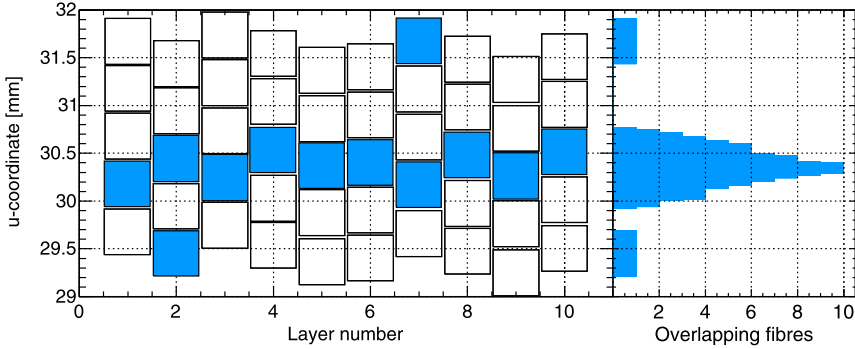


Fig. 3. Hit pattern of a proton trajectory in the ten fibre layers comprising the u coordinate. The superposition of fibre hits attributed to a track is shown in the histogram. The position of maximum overlap is used to determine the track position.

wire-scan method [39] and monitored bunch-by-bunch throughout the run using two beam synchrotron radiation monitor systems; the latter were calibrated to the wire-scan measurements at the start of the run. The emittances varied smoothly from $2.2 \mu\text{m}$ to $3.0 \mu\text{m}$ ($3.2 \mu\text{m}$ to $4.2 \mu\text{m}$) for beam 1 (beam 2) in the horizontal plane and from $1.9 \mu\text{m}$ to $2.2 \mu\text{m}$ ($2.0 \mu\text{m}$ to $2.2 \mu\text{m}$) for beam 1 (beam 2) in the vertical plane. The systematic uncertainty on the emittance is about 10%. A luminosity-weighted average emittance is used in the simulation, resulting in an angular beam divergence of about $3 \mu\text{rad}$.

5.3. Trigger conditions

To trigger on elastic-scattering events, two main triggers were used. The triggers required a coincidence of the main detector trigger scintillators between either of the two upper (lower) detectors on side A and either of the two lower (upper) detectors on side C. The elastic-scattering rate was typically 50 Hz in each arm. The trigger efficiency for elastic-scattering events was determined from a data stream in which all events with a hit in any one of the ALFA trigger counters were recorded. In the geometrical acceptance of the detectors, the efficiency of the trigger used to record elastic-scattering events is $99.96 \pm 0.01\%$.

6. Track reconstruction and alignment

6.1. Track reconstruction

The reconstruction of elastic-scattering events is based on local tracks of the proton trajectory in the RP stations. A well-reconstructed elastic-scattering event consists of local tracks in all four RP stations.

The local tracks in the MDs are reconstructed from the hit pattern of protons traversing the scintillating fibre layers. In each MD, 20 layers of scintillating fibres are arranged perpendicular to the beam direction. The hit pattern of elastically scattered protons is characterized by a straight trajectory, almost parallel to the beam direction. In elastic events the average multiplicity per detector is about 23 hits, where typically 18–19 are attributed to the proton trajectory while the remaining 4–5 hits are due to beam-related background, cross-talk and electronic noise.

The reconstruction assumes that the protons pass through the fibre detector perpendicularly. A small angle below 1 mrad with respect to the beam direction has no sizeable impact. The

first step of the reconstruction is to determine the u and v coordinates from the two sets of ten layers which have the same orientation. The best estimate of the track position is given by the overlap region of the fiducial areas of all hit fibres. As illustrated in Fig. 3, the staggering of the fibres narrows the overlap region and thereby improves the resolution. The centre of the overlap region gives the u or v coordinate, while the width determines the resolution. Pairs of u and v coordinates are transformed to spatial positions in the beam coordinate system.

To exclude events with hadronic showers and layers with a high noise level, fibre layers with more than ten hits are not used in track reconstruction. At least three layers out of the possible ten are required to have a hit multiplicity between one and three. Finally, the u and v coordinates accepted for spatial positions must be formed from at least three overlapping hit fibres.

If more than one particle passes through the detector in a single event, the orthogonal fibre geometry does not allow a unique formation of tracks. In elastic-scattering events, multiple tracks can originate from associated halo or shower particles as well as the overlap of two events. The first type of multiple tracks happens mostly at one side of the spectrometer arms and can be removed by track-matching with the opposite side. In the case of elastic pile-up, where multiple tracks are reconstructed in both arms, only the candidate with the best track-matching is accepted. The fraction of genuine pile-up is about 0.1% and is corrected by a global factor as described in Section 7.1.

The reconstruction of tracks in the ODs is based on the same method as described here for the MDs, but with reduced precision since only three fibre layers are available.

6.2. Alignment

The precise positions of the tracking detectors with respect to the circulating beams are crucial inputs for the reconstruction of the proton kinematics. For physics analysis, the detector positions are directly determined from the elastic-scattering data.

The alignment procedure is based on the distribution of track positions in the RP stations in the full elastic-scattering event sample. This distribution forms a narrow ellipse with its major axis in the vertical (y) direction, with an aperture gap between the upper and lower detectors. The measured distances between upper and lower MDs and the rotation symmetry of scattering angles are used as additional constraints.

Three parameters are necessary to align each MD: the horizontal and vertical positions and the rotation angle around the beam axis. A possible detector rotation around the horizontal or vertical axes can be of the order of a few mrad, as deduced from survey measurements and the alignment corrections for rotations around the beam axis. Such tiny deviations from the nominal angles result in small offsets which are effectively absorbed in the three alignment parameters.

The horizontal detector positions and the rotation angles are determined from a fit of a straight line to a profile histogram of the narrow track patterns in the upper and lower MDs. The uncertainties are 1–2 μm for the horizontal coordinate and 0.5 mrad for the angles.

For the vertical detector positioning, the essential input is the distance between the upper and lower MDs. Halo particles which pass the upper and lower ODs at the same time are used for this purpose. Combining the two y -coordinates allows this distance to be determined. Many halo events are used to improve the precision of the distance value by averaging over large samples. The associated systematic uncertainty in the distance value is derived from variations of the requirements on hit and track multiplicities in the ODs. The measured distances between the upper and lower MDs for the nominal position at $6.5 \times \sigma_y$ and related errors are shown in Table 1. The main contributions to the uncertainty on the distance are due to uncertainties in the fibre

Table 1

The distance between the upper and lower MDs and related vertical detector positions. The coordinates y_{meas} refer to the individual alignment per station while the coordinates y_{ref} are derived by extrapolation using beam optics from the detector positions in the reference station A7L1. The quoted errors include statistical and systematic contributions.

| Detector | Station | Distance [mm] | y_{meas} [mm] | y_{ref} [mm] |
|----------|---------|--------------------|------------------------|-----------------------|
| A1 | B7L1 | 11.962 ± 0.081 | 5.981 ± 0.093 | 5.934 ± 0.076 |
| A2 | | 11.962 ± 0.081 | -5.981 ± 0.093 | -5.942 ± 0.076 |
| A3 | A7L1 | 12.428 ± 0.022 | 6.255 ± 0.079 | 6.255 ± 0.078 |
| A4 | | 12.428 ± 0.022 | -6.173 ± 0.079 | -6.173 ± 0.080 |
| A5 | A7R1 | 12.383 ± 0.018 | 6.080 ± 0.078 | 6.036 ± 0.088 |
| A6 | | 12.383 ± 0.018 | -6.304 ± 0.078 | -6.273 ± 0.087 |
| A7 | B7R1 | 11.810 ± 0.031 | 5.765 ± 0.077 | 5.820 ± 0.083 |
| A8 | | 11.810 ± 0.031 | -6.045 ± 0.077 | -6.120 ± 0.084 |

positions and the relative alignment of the ODs with respect to the MDs, both typically $10 \mu\text{m}$. The most precise distance values, with uncertainties of about $20 \mu\text{m}$, are achieved for the two inner stations A7L1 and A7R1. The values for the outer stations are degraded by shower particles from interactions in the inner stations. The large error on the distance in station B7L1 is due to a detector which was not calibrated in a test beam.

The absolute vertical detector positions with respect to the beam are determined using the criterion of equal track densities in the upper and lower MDs at identical distances from the beam. The reconstruction efficiency in each spectrometer arm, as documented in Section 7.3, is taken into account. A sliding window technique is applied to find the positions with equal track densities. The resulting values y_{meas} are summarized in Table 1. The typical position error is about $80 \mu\text{m}$, dominated by the uncertainties on the reconstruction efficiency.

For the physics analysis, all vertical detector positions are derived from the detector positions in a single reference station by means of the beam optics. The measured lever arm ratios M_{12}^X/M_{12}^{A7L1} , with X labelling any other station, are used for the extrapolation from the reference station to the other stations. As a reference the detector positions y_{meas} of the inner station A7L1 with a small distance error were chosen. The resulting detector positions y_{ref} are also given in Table 1. Selecting the other inner station A7R1 as a reference indicates that the systematic uncertainty due to the choice of station is about $20 \mu\text{m}$, which is well covered by the total position error.

7. Data analysis

7.1. Event selection

All data used in this analysis were recorded in a single run and only events resulting from collisions of the bunch pair with about 7×10^{10} protons per bunch were selected; events from pilot bunches were discarded. Furthermore, only periods of the data taking where the dead-time fraction was below 5% are used. This requirement eliminates a few minutes of the run. The average dead-time fraction was 0.3% for the selected data.

Events are required to pass the trigger conditions for elastic-scattering events, and have a reconstructed track in all four detectors of the arm which fired the trigger. Events with additional tracks in detectors of the other arm arise from the overlap of halo protons with elastic-scattering protons and are retained. In the case of an overlap of halo and elastic-scattering protons in the

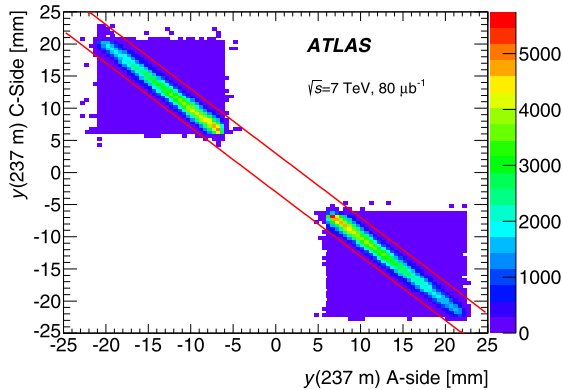


Fig. 4. The correlation of the y coordinate measured at the A- and C-side for the inner stations. Elastic-scattering candidates after data quality, trigger and bunch selection but before acceptance and background rejection cuts are shown. Identified elastic events are required to lie between the red lines. (For interpretation of the references to color in this figure legend, the reader is referred to the web version of this article.)

same detectors, which happens typically only on one side, a matching procedure between the detectors on each side is applied to identify the elastic-scattering track.

Further geometrical cuts on the left-right acollinearity are applied, exploiting the back-to-back topology of elastic-scattering events. The position difference between the left and the right sides is required to be within 3.5σ of its resolution determined from simulation, as shown in Fig. 4 for the vertical coordinate. An efficient cut against non-elastic background is obtained from the correlation of the local angle between two stations and the position in the horizontal plane, as shown in Fig. 5, where elastic-scattering events appear inside a narrow ellipse with positive slope, whereas beam-halo background is concentrated in a broad ellipse with negative slope or in an uncorrelated band.

Finally, fiducial cuts to ensure a good containment inside the detection area are applied to the vertical coordinate. It is required to be at least $60\ \mu\text{m}$ from the edge of the detector nearer the beam, where the full detection efficiency is reached. At large vertical distance, the vertical coordinate must be at least 1 mm away from the shadow of the beam screen, a protection element of the quadrupoles, in order to minimize the impact from showers generated in the beam screen.

The numbers of events in the two arms after each selection criterion are given in Table 2. At the end of the selection procedure 805 428 events survive all cuts. A small asymmetry is observed between the two arms, which arises from the detectors being at different vertical distances, asymmetric beam-screen positions and background distributions. A small number of elastic pile-up events corresponding to a 0.1% fraction is observed, where two elastic events from the same bunch crossing are reconstructed in two different arms. Elastic pile-up events can also occur with two protons in the same detectors; in this case only one event is counted as described in Section 6.1. A correction is applied for the pile-up events appearing in the same arms, by scaling the pile-up events in different arms by a factor of two.

7.2. Background determination

A small fraction of the background is expected to be inside the area defined by the elliptical contour used to reject background shown in Fig. 5. The background events peak at small values of x and y and thus constitute an irreducible background at small $|t|$. The background pre-

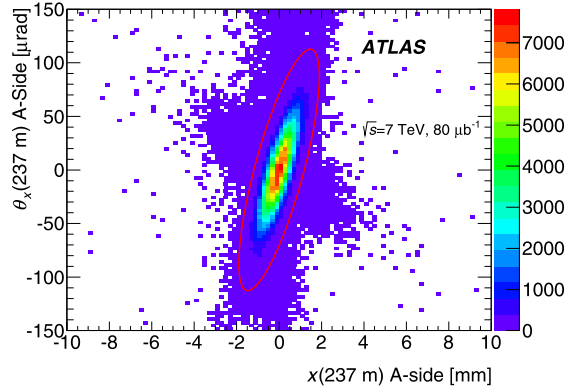


Fig. 5. The correlation between the horizontal coordinate, x , and the local horizontal angle, θ_x , on the A-side. Elastic-scattering candidates after data quality, trigger and bunch selection but before acceptance and background rejection cuts are shown. Identified elastic events are required to lie inside the red ellipse.

Table 2

Numbers of events after each stage of the selection. The fractions of events surviving the event-selection criterion with respect to the total number of reconstructed events are shown for each criterion. The last row gives the number of observed pile-up events.

| Selection criterion | Numbers of events | | | |
|--------------------------|-------------------|----------|---------|----------|
| Raw number of events | 6 620 953 | | | |
| Bunch group selection | 1 898 901 | | | |
| Data quality selection | 1 822 128 | | | |
| Trigger selection | 1 106 855 | | | |
| | Arm 1 | fraction | Arm 2 | fraction |
| Reconstructed tracks | 459 229 | | 428 213 | |
| Cut on x left vs right | 445 262 | 97.0% | 418 142 | 97.6% |
| Cut on y left vs right | 439 887 | 95.8% | 414 421 | 96.8% |
| Cut on x vs θ_x | 434 073 | 94.5% | 410 558 | 95.9% |
| Beam-screen cut | 419 890 | 91.4% | 393 320 | 91.9% |
| Edge cut | 415 965 | 90.6% | 389 463 | 91.0% |
| Total selected | 805 428 | | | |
| Elastic pile-up | 1060 | | | |

dominantly originates from accidental coincidences of beam-halo particles, but single diffractive protons in coincidence with a halo proton at the opposite side may also contribute.

While elastic-scattering events are selected in the “golden” topology with two tracks in opposite vertical detector positions on the left and right side, events in the “anti-golden” topology with two tracks in both upper or both lower detectors at the left and right side are pure background from accidental coincidences. After applying the event selection cuts, these events yield an estimate of background in the elastic sample with the golden topology. Furthermore, the anti-golden events can be used to calculate the form of the t -spectrum for background events by flipping the sign of the vertical coordinate on either side. As shown in Fig. 6, the background t -spectrum peaks strongly at small t and falls off steeply, distinguishably different from the distribution obtained for elastic events.

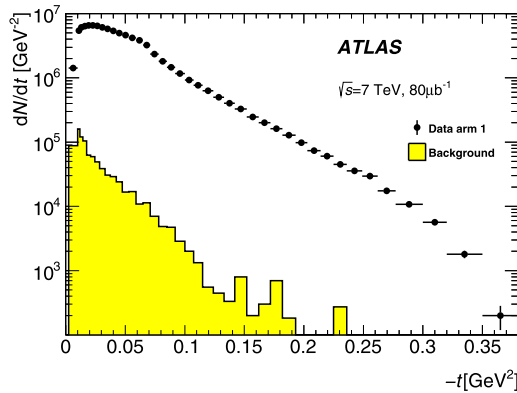


Fig. 6. The counting rate dN/dt , before corrections, as a function of t in arm 1 compared to the background spectrum determined using anti-golden events. The form of the distribution is modified by acceptance effects (see Fig. 9).

Table 3

Number of background events in each arm estimated with the anti-golden method and systematic uncertainties from the difference from the vertex method. The arm ++ comprises all four upper detectors, the arm -- all four lower detectors.

| | Arm ++ | Arm -- |
|------------------------------|------------|------------|
| Numbers of background events | 3329 | 1497 |
| Statistical error | ± 58 | ± 39 |
| Systematic error | ± 1100 | ± 1200 |

Alternatively, the amount of background per arm is determined from the distribution of the horizontal vertex position at the interaction point, reconstructed using the beam optics transport Eq. (4). For elastic scattering, the vertex position peaks at small values of x , whereas for background the shape is much broader since halo background does not originate from the interaction point. Hence the fraction of background events can be determined from a fit to the measured distribution using templates.

The anti-golden method is used to estimate the background. Systematic uncertainties in the normalization are taken from the difference between the anti-golden method and the vertex method, while the background shape uncertainty is obtained from variations of the flipping procedure used to transform the anti-golden events into elastic-like events. The expected numbers of background events are given in Table 3 together with their uncertainties. The total uncertainty on the background is dominated by the systematic uncertainty of 50–80%. Given the overall small background contamination of about 0.5%, the large systematic uncertainty has only a small impact on the total cross-section determination.

7.3. Event reconstruction efficiency

Elastic-scattering events inside the acceptance region are expected to have a proton track in each of the four detectors of the corresponding spectrometer arm. However, in the case of interactions of the protons or halo particles with the stations or detectors, which result in too large fibre hit multiplicities, the track reconstruction described in Section 6.1 may fail. The rate

of elastic-scattering events has to be corrected for losses due to such partly reconstructed events. This correction is defined as the event reconstruction efficiency.

A method based on a tag-and-probe approach is used to estimate the efficiency. Events are grouped into several reconstruction cases, for which different selection criteria and corrections are applied, to determine if an event is from elastically scattered protons, but was not fully reconstructed because of inefficiencies.

The reconstruction efficiency of elastic-scattering events is defined as $\varepsilon_{\text{rec}} = N_{\text{reco}}/(N_{\text{reco}} + N_{\text{fail}})$, where N_{reco} is the number of fully reconstructed elastic-scattering events, which have at least one reconstructed track in each of the four detectors of a spectrometer arm, and N_{fail} is the number of not fully reconstructed elastic-scattering events which have reconstructed tracks in fewer than four detectors. It does not include the efficiency of other selection cuts, which is discussed in Section 8, and is separate from any acceptance effects. Events of both classes need to have an elastic-scattering trigger signal and need to be inside the acceptance region, i.e. they have to fulfill the event selection criteria for elastic-scattering events. The efficiency is determined separately for the two spectrometer arms. Based on the number of detectors with at least one reconstructed track the events are grouped into six reconstruction cases 4/4, 3/4, 2/4, (1 + 1)/4, 1/4 and 0/4. Here the digit in front of the slash indicates the number of detectors with at least one reconstructed track. In the 2/4 case both detectors with tracks are on one side of the interaction point and in the (1 + 1)/4 case they are on different sides. With this definition one can write

$$\varepsilon_{\text{rec}} = \frac{N_{\text{reco}}}{N_{\text{reco}} + N_{\text{fail}}} = \frac{N_{4/4}}{N_{4/4} + N_{3/4} + N_{2/4} + N_{(1+1)/4} + N_{1/4} + N_{0/4}}, \quad (15)$$

where $N_{k/4}$ is the number of events with k detectors with at least one reconstructed track in a spectrometer arm. The event counts $N_{k/4}$ need to be corrected for background, which is described in the following.

Elastic-scattering events are selected for the various cases based on the event selection criteria described in Section 7.1. The proton with reconstructed tracks on one side of the interaction point is used as a tag and the one on the other side as a probe. Both tag and probe have to pass the event selection to be counted as an elastic-scattering event and to be classified as one of the reconstruction cases. Depending on the case, only a sub-set of the event selection criteria can be used, because just a limited number of detectors with reconstructed tracks is available. For example it is not possible to check for left-right acollinearity of 2/4 events, because tracks are only reconstructed on one side of the interaction point. To disentangle the efficiency from acceptance, the total fibre hit multiplicity (sum of all fibre hits in the 20 layers of a detector; maximum is 1280 hits) in all detectors without any reconstructed track has to have a minimum value of six. In this way, events where tracks could not be reconstructed due to too few fibre hits are excluded from the efficiency calculation and only handled by the acceptance, which is discussed in Section 8.

With events from the 3/4 case it is possible to apply most of the event selection criteria and reconstruct t well with the subtraction method. The position distribution of reconstructed tracks in 3/4 events agrees very well with that from 4/4 events, as shown in Fig. 7 for the vertical coordinate. Because of this good agreement and the ability to reconstruct t , a partial event reconstruction efficiency $\hat{\varepsilon}_{\text{rec}}(t) = N_{4/4}(t)/[N_{4/4}(t) + N_{3/4}(t)]$ as a function of t can be constructed, as shown in Fig. 8. Linear fits, applied to the partial efficiencies of each spectrometer arm, yield small residual slopes consistent with zero within uncertainties. This confirms that

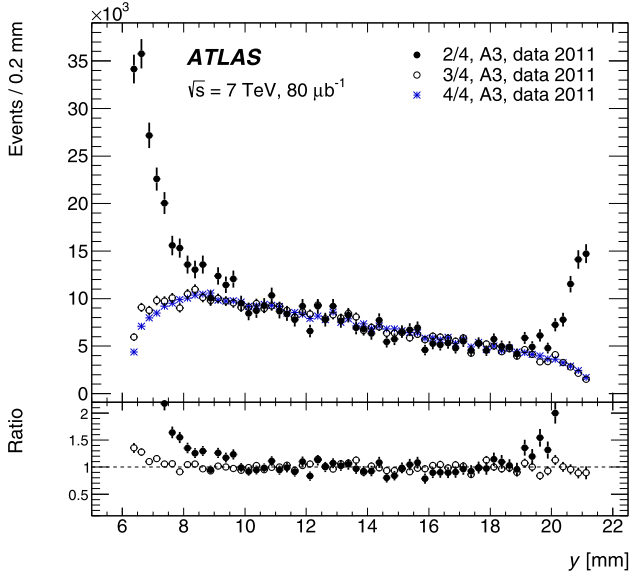


Fig. 7. Distribution of the vertical track position at the detector surface for detector A3 of the 2/4 case (●) where no track was reconstructed in A6 and A8, the 3/4 case (○) where no track was reconstructed in A8 and of the 4/4 case (✱). The distributions are normalized to the number of events in the 4/4 case. The bottom panel displays ratios between $k/4$ and 4/4 with statistical uncertainties.

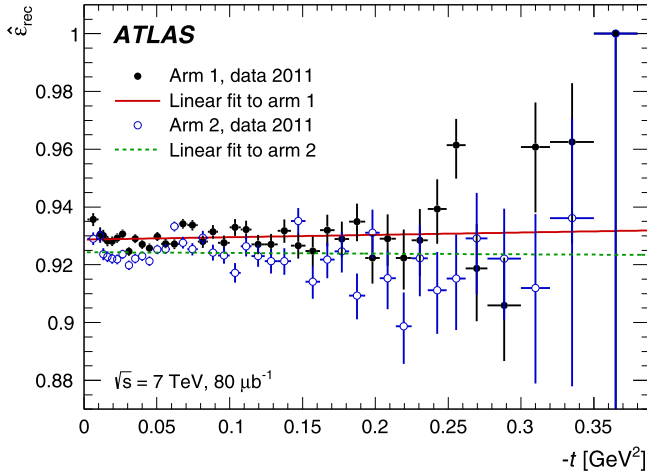


Fig. 8. Partial event reconstruction efficiency $\hat{\epsilon}_{\text{rec}}$ as a function of $-t$ for elastic arms 1 (●) and 2 (○). The solid line is a linear fit to arm 1 and the dashed one to arm 2.

the efficiency ϵ_{rec} in Eq. (15) is independent of t , as is expected from the uniform material distribution in the detector volume.

Two complications arise when counting 2/4 events. First, the vertical position distributions of the two detectors with reconstructed tracks do not agree with that from 4/4 events. As shown in Fig. 7 for A3, peaks appear at both edges of the distribution. These peaks are caused by

events where protons hit the beam screen or thin RP window on one side of the interaction point and tracks are therefore only reconstructed on the other side. Since these events would be excluded by acceptance cuts, they are removed from the efficiency calculation. This is achieved by extrapolating the vertical position distribution from the central region without the peaks to the full region using the shape of the distribution from 4/4 events.

The second complication arises from single-diffraction background, which has a similar event topology to the 2/4 events. This background is reduced by elastic-scattering trigger conditions, but an irreducible component remains. Therefore, the fraction of elastic-scattering events is determined with a fit, which uses two templates to fit the horizontal position distributions. Templates for elastic-scattering events and a combination of single diffraction and other backgrounds are both determined from data. For the elastic-scattering template, events are selected as described in Section 7.1. Events for the background template are selected based on various trigger signals that enhance the background and reduce the elastic-scattering contribution. The fit yields an elastic-scattering fraction in the range of $r_{el} = 0.88$ to 0.96 , depending on the detector.

Because about 95% of N_{fail} consists of 3/4 and 2/4 events, the other cases play only a minor role. For cases $(1 + 1)/4$ and $1/4$ an additional event selection criterion on the horizontal position distribution is applied to enhance the contribution from elastic scattering and suppress background. Edge peaks are present in the y -position distributions of $1/4$ events, and the extrapolation procedure, described above, is also applied. In the $0/4$ case no track is reconstructed in any detector and the event selection criteria cannot be applied. Therefore, the number of $0/4$ events is estimated from the probability to get a $2/4$ event, which is determined from the ratio of the number of $2/4$ to the number of $4/4$ events. The contribution to N_{fail} of this estimated number of $0/4$ events is only about 1%.

The systematic uncertainties on the reconstruction efficiency are determined by varying the event selection criteria. Additional uncertainties arise from the choice of central extrapolation region in y for $2/4$ and $1/4$ events and from the fraction fit. The uncertainties on the fraction fit are also determined by selection criteria variation and an additional uncertainty is attributed to the choice of background template.

The event reconstruction efficiencies in arm 1 and arm 2 are determined to be $\varepsilon_{rec,1} = 0.8974 \pm 0.0004$ (stat.) ± 0.0061 (syst.) and $\varepsilon_{rec,2} = 0.8800 \pm 0.0005$ (stat.) ± 0.0092 (syst.) respectively. The efficiency in arm 1 is slightly larger than in arm 2, due to differences in the detector configurations. In arm 1 the trigger plates are positioned after the scintillating tracking fibres and in arm 2 they are positioned in front of them. This orientation leads to a higher shower probability and a lower efficiency in arm 2.

8. Acceptance and unfolding

The acceptance is defined as the ratio of events passing all geometrical and fiducial acceptance cuts defined in Section 7.1 to all generated events and is calculated as a function of t . The calculation is carried out with PYTHIA8 as elastic-scattering event generator and MadX for beam transport based on the effective optics (see Section 9.2). The acceptance is shown in Fig. 9 for each arm.

The shape of the acceptance curve can be understood from the contributions of the vertical and horizontal scattering angles to t , $-t = ((\theta_x^*)^2 + (\theta_y^*)^2)p^2$. The smallest accessible value of t is obtained at the detector edge and set by the vertical distance of the detector from the beam. Close to the edge, the acceptance is small because a fraction of the events is lost due to beam divergence, i.e. events being inside the acceptance on one side but outside at the other side. At small $|t|$ up

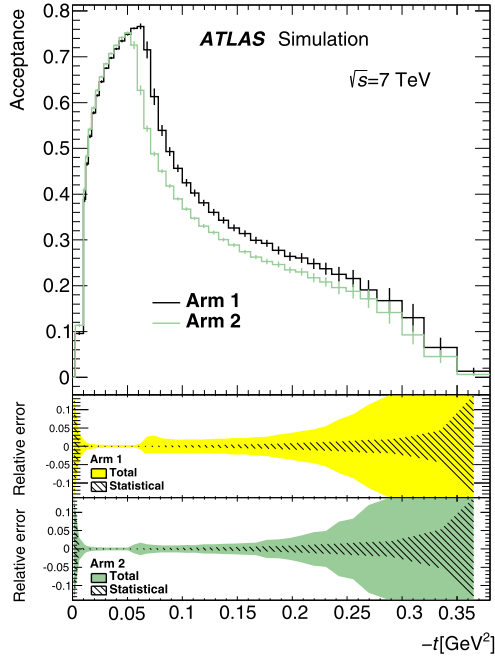


Fig. 9. The acceptance as a function of the true value of t for each arm with total uncertainties shown as error bars. The lower panels show relative total and statistical uncertainties.

to $-t \sim 0.07 \text{ GeV}^2$ vertical and horizontal scattering angles contribute about equally to a given value of t . Larger t -values imply larger vertical scattering angles and larger values of y , and with increasing y the fraction of events lost in the gap between the main detectors decreases. The maximum acceptance is reached for events occurring at the largest possible values of y within the beam-screen cut. Beyond that point the acceptance decreases steadily because the events are required to have larger values of x since these t -values are dominated by the horizontal scattering angle component. This also explains the difference between the two arms, which is dominated by the difference between the respective beam-screen cuts.

The measured t -spectrum is affected by detector resolution and beam smearing effects, including angular divergence, vertex smearing and energy smearing. These effects are visible in the t -resolution and the purity of the t -spectrum. The purity is defined as the ratio of the number of events generated and reconstructed in a particular bin to the total number of events reconstructed in that bin. The purity is about 60% for the subtraction method, and is about a factor of two worse for the local angle method. The limited t -resolution induces migration effects between bins, which reduces the purity. Fig. 10 shows the t -resolution for different t -reconstruction methods.

The resolution for the subtraction method improves from 12% at small $|t|$ to 3% at large $|t|$ and is about a factor three to four better than the other methods. The t -resolution differences arise because of differences in the spatial and angular resolution of the various reconstruction methods. The subtraction method is superior to the others because only the spatial resolution contributes, whereas the poor angular resolution in the horizontal plane degrades the resolution of the other methods.

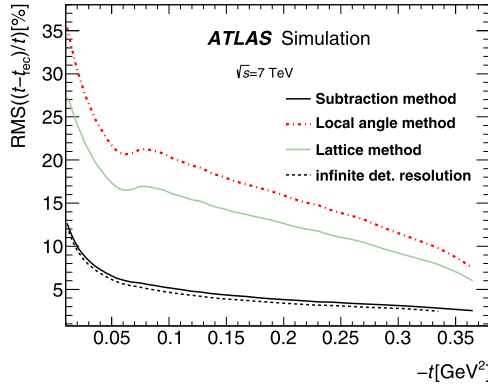


Fig. 10. The relative resolution $\text{RMS}((t - t_{\text{rec}})/t)$, where t_{rec} is the reconstructed value of t , for different reconstruction methods. The resolution for local subtraction is not shown as it is practically the same as for the lattice method. The dotted line shows the resolution without detector resolution, accounting only for beam effects. It is the same for all methods.

The measured t -spectrum in each arm, after background subtraction, is corrected for migration effects using an iterative, dynamically stabilized unfolding method [40]. Monte Carlo simulation is used to obtain the migration matrix used in the unfolding. The results are cross-checked using an unfolding based on the singular value decomposition method [41]. The unfolding procedure is applied to the distribution obtained using all selected events, after background subtraction in each elastic arm.

A data-driven closure test is used to evaluate any bias in the unfolded data spectrum shape due to mis-modelling of the reconstruction-level spectrum shape in the simulation. The simulation is reweighted at particle level such that the reconstructed simulation matches the data. The modified reconstruction-level simulation is unfolded using the original migration matrix, and the result is compared with the modified particle-level spectrum. The resulting bias is considered as a systematic uncertainty. An additional closure test, based on Monte Carlo simulation, was performed with independent Monte Carlo samples with a different physics model with different nuclear slopes.

Further systematic uncertainties are related to the simulation of the detector resolution and beam conditions, as discussed in Section 11. The systematic shifts are smaller than 0.5% in the $|t|$ -range below 0.2 GeV² and increase up to 3% at large $|t|$ for all methods of t -reconstruction.

The unfolding method introduces correlations between bins of the t -spectrum. These correlations are calculated using simulated pseudo-experiments with the same number of events as the data. The resulting statistical covariance matrix is included in the fits for the total cross section.

9. Beam optics

The precision of the t -reconstruction depends on knowledge of the elements of the transport matrix. From the design of the 90 m beam optics along with the alignment parameters of the magnets, the magnet currents and the field calibrations, all transport matrix elements can be calculated. This initial set of matrix elements is referred to as “design optics”. Small corrections, allowed within the range of the systematic uncertainties, need to be applied to the design optics for the measurement of σ_{tot} . In particular, corrections are needed in the horizontal plane where the phase advance is close to 180°, because the lever arm $M_{12} = \sqrt{\beta \times \beta^*} \sin \Psi$ is rather sensitive to the value of Ψ .

Constraints on beam optics parameters are derived from the ALFA data, exploiting the fact that the reconstructed scattering angle must be the same for different reconstruction methods using different transport matrix elements. The beam optics parameters are determined from a global fit, using these constraints, with the design optics as a starting value.

9.1. ALFA constraints

The reconstructed tracks from elastic collisions can be used to derive certain constraints on the beam optics directly from the data. Two classes of constraints are distinguished:

- Correlations between positions or angles measured either at the A-side and C-side or at inner and outer stations of ALFA. These are used to infer the ratio of matrix elements in the beam transport matrix. The resulting constraints are independent of any optics input.
- Correlations between the reconstructed scattering angles. These are calculated using different methods to derive further constraints on matrix elements as scaling factors. These factors indicate the amount of scaling needed for a given matrix element ratio in order to equalize the measurement of the scattering angle. These constraints depend on the given optics model. The design beam optics with quadrupole currents measured during the run is used as reference to calculate the constraints.

With parallel-to-point focusing the measured position at the RP is to a first approximation related to the scattering angle by $w = M_{12,w} \times \theta_w^*$, $w \in \{x, y\}$, up to a small contribution from the vertex term in M_{11} in the horizontal plane. The ratio of A-side to the C-side track positions is thus on average equal to the ratio of the lever arms M_{12}^A/M_{12}^C , because the scattering angle at the A-side is the same as at the C-side for elastic scattering, up to beam divergence effects. In a similar way, the ratio of the M_{22} matrix elements is obtained from the correlation between the angles measured in the two stations on one side. In the vertical plane the ratio of M_{12} between the inner and outer station is also measured, whereas in the horizontal plane the correlation between positions cannot be translated into a measurement of the M_{12} ratio because of the contribution from the vertex term in M_{11} , which is different for the inner and outer detectors.

The second class of constraints is derived from the assumption that the reconstructed scattering angle must be the same for different methods for a consistent beam optics model. The best example is the comparison of the scattering angle in the horizontal plane reconstructed with the subtraction method, Eq. (5), which is based on the position and $M_{12,x}$, and the local angle method, Eq. (6), which is based on the local angle and $M_{22,x}$. The scaling factor for the matrix element ratio M_{12}/M_{22} is derived from the slope of the difference of the scattering angle between the two methods as a function of the scattering angle determined with the subtraction method, as shown in Fig. 11. Here the slope of about 5% indicates that the design optics ratio $M_{12,x}/M_{22,x}$ needs to be increased by 5% in order to obtain from the data, on average, the same scattering angle from both methods. As discussed in Section 9.2 such an increase in the ratio is compatible with realistic deviations of the quadrupole strengths from nominal. Constraints of this type are obtained for inner and outer detectors in both the vertical and horizontal planes independently.

Finally, a constraint on the ratio of the M_{12} matrix element in the vertical plane to that in the horizontal plane is derived from the isotropy of the scattering angle in the transverse plane. Here 2D-patterns of the horizontal and vertical scattering angle components reconstructed with the subtraction method are analyzed by selecting regions with approximately constant density, which appear as sections of a circle in the case of perfect optics. A scaling factor for $M_{12,y}/M_{12,x}$

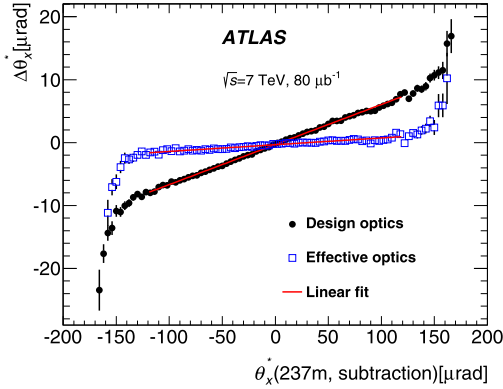


Fig. 11. The difference in reconstructed scattering angle $\Delta\theta_x^*$ between the subtraction and local angle methods as a function of the scattering angle from subtraction method for the inner detectors. In each bin of the scattering angle the points show the mean value of $\Delta\theta_x^*$ and the error bar represents the RMS. The line represents the result of a linear fit. Values obtained using the effective optics (see Section 9.2) are also shown for comparison.

Table 4

Summary of the ALFA constraints on beam optics with uncertainties. The first group of constraints are for transport matrix element ratios, the second group comprises scaling factors for matrix element ratios with respect to design optics. B_1 and B_2 represent beam 1 and beam 2.

| Constraint | Value | Stat. | Syst. | Total |
|--------------------------------------|--------|--------|--------|--------|
| $M_{12,x}(237\text{ m})B_2/B_1$ | 1.0063 | 0.0015 | 0.0041 | 0.0044 |
| $M_{12,x}(241\text{ m})B_2/B_1$ | 1.0034 | 0.0010 | 0.0041 | 0.0042 |
| $M_{22,x}B_2/B_1$ | 0.9932 | 0.0007 | 0.0041 | 0.0042 |
| $M_{12,y}(237\text{ m})B_2/B_1$ | 0.9951 | 0.0001 | 0.0026 | 0.0026 |
| $M_{12,y}(241\text{ m})B_2/B_1$ | 0.9972 | 0.0001 | 0.0026 | 0.0026 |
| $M_{12,y}237/241B_2$ | 1.0491 | 0.0001 | 0.0007 | 0.0008 |
| $M_{12,y}237/241B_1$ | 1.0481 | 0.0001 | 0.0007 | 0.0008 |
| $M_{22,y}B_2/B_1$ | 0.9830 | 0.0002 | 0.0180 | 0.0180 |
| $R(M_{12,x}/M_{22,x})(237\text{ m})$ | 1.0551 | 0.0003 | 0.0022 | 0.0023 |
| $R(M_{12,x}/M_{22,x})(241\text{ m})$ | 1.0453 | 0.0002 | 0.0013 | 0.0014 |
| $R(M_{12,y}/M_{22,y})(237\text{ m})$ | 1.0045 | 0.0001 | 0.0061 | 0.0061 |
| $R(M_{12,y}/M_{22,y})(241\text{ m})$ | 1.0046 | 0.0001 | 0.0065 | 0.0065 |
| $R(M_{12,y}/M_{12,x})(237\text{ m})$ | 0.9736 | 0.0052 | 0.0104 | 0.0116 |
| $R(M_{12,y}/M_{12,x})(241\text{ m})$ | 0.9886 | 0.0057 | 0.0072 | 0.0092 |

is inferred from a fit of an ellipse to these patterns, and the ratio of matrix elements is taken from the ratio of the major to minor axis of the ellipse. All ALFA constraints on the beam optics are summarized in Table 4.

Systematic uncertainties are obtained from several variations of the analysis and dominate the precision of the constraints. An important uncertainty is deduced from the difference between the constraints for the two arms, i.e. the difference between the upper and lower detectors for which the optics must be the same. A variation of the selection cuts is used to probe the possible influence of background. All constraints are obtained from fits and a variation of the fit range allows potential biases related to acceptance effects to be tested. All alignment parameters are varied within their systematic uncertainties and the constraint analysis repeated. The observed maximum change in each constraint is taken as the corresponding systematic uncertainty. The limited

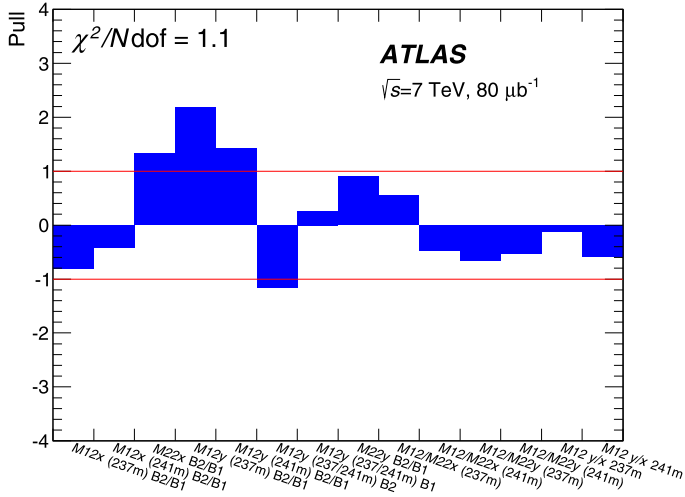


Fig. 12. Pulls from the beam optics fit to the ALFA constraints which are given in Table 4.

detector resolution induces in the scaling factors a small bias of about 0.5% even with perfect optics. This is estimated with simulation and subtracted. This correction depends on the physics model and detector resolution used in the simulation. The simulation was repeated with a variation of the nuclear slope $B = 19.5 \pm 1.0 \text{ GeV}^{-2}$ and separately with a variation of the detector resolution according to the procedure outlined in Section 4.1. In both cases the maximum change of the constraints with the alternative bias corrections is taken as a systematic uncertainty. For some of the constraints with a similar type of uncertainty the systematic errors are averaged to suppress statistical fluctuations.

9.2. Beam optics fit

The constraints described in the previous section are combined in a fit used to determine the beam optics. The free parameters of the fit are the quadrupole strengths in both beams. All ALFA constraints are treated as uncorrelated. The effect of the longitudinal quadrupole position is negligible when varied by its uncertainty, though this is considered in the total systematic uncertainties (see Section 11.1). In the minimization procedure, the beam optics calculation program MadX is used to extract the optics parameters and to calculate the matrix element ratios for a given set of magnet strengths.

The ALFA detection system provides precise constraints on the matrix element ratios, but cannot probe the deviation of single magnets. Therefore several sets of optics parameters exist that minimize the χ^2 , arising from different combinations of magnet strengths. The chosen configuration, called the effective optics, is one solution among many. This solution is obtained by allowing only the inner triplet magnets Q1 and Q3 to vary coherently from their nominal strength. Q1 and Q3 were manufactured at a different site from the other quadrupoles, and relative calibration differences are possible. Other alternatives are taken into account in the total systematic uncertainties (see Section 11.1).

Fig. 12 shows the pull of the ALFA constraints after the minimization, which resulted in an offset of approximately 0.3% for the strength of Q1 and Q3, with a difference of about 10% between the two beams. The χ^2 of the fit includes the systematic uncertainties of the constraints and

is of good quality with $\chi^2/N_{\text{dof}} = 13.2/12$. No measurement deviates from the fit by more than about two standard deviations; the largest deviation is observed for the high-precision constraint on M_{12} in the vertical plane. This solution was cross-checked using the LHC measurements of the phase advance. This effective optics is used for the total cross-section measurement.

10. Luminosity determination

In normal running conditions at high luminosity ($L > 10^{33} \text{ cm}^{-2} \text{ s}^{-1}$), ATLAS exploits several detectors and algorithms to determine the luminosity and evaluate the related systematic uncertainty. These include LUCID (luminosity measurement with a Cherenkov integrating detector), BCM (beam conditions monitor) and the inner detector, for the bunch-by-bunch luminosity determination, and the tile and forward calorimeters, for bunch-integrated luminosity measurements. Details of the ATLAS luminosity measurement can be found in Ref. [42], which includes a description of all the detectors and algorithms, the calibration procedure, the background evaluation and subtraction and the estimation of the systematic uncertainties.

The conditions in the low-luminosity run analyzed here are very different from those in high-luminosity runs. The instantaneous luminosity is about six orders of magnitude lower ($L \sim 5 \times 10^{27} \text{ cm}^{-2} \text{ s}^{-1}$) which makes the calorimeter methods unusable due to the lack of sensitivity. An additional method based on vertex counting in the inner detector (ID) was included; this method is most effective at low pile-up. Another difference with respect to the normal high-luminosity conditions is the background composition: the beam–gas contribution, normally negligible, can become competitive with the collision rate in the low-luminosity regime. The background due to slowly decaying, collision-induced radiation (often called “afterglow” [42]) becomes conversely less important, because of the presence of only a few colliding bunches.

In the 2011 data taking, the BCM was used as the baseline detector for the luminosity determination. It consists of four independent detectors grouped into two sets of two, vertical (BCMV) and horizontal (BCMH), located on each side of the interaction point and made of diamond sensors. For the high- β^* run, an inclusive-OR of the two sides was used to define an event with activity in the detector. The luminosity is determined with the event-counting method based on this definition (BCMV_EventOR, BCMH_EventOR). LUCID is also located on both sides of the interaction point and detects charged particles produced in the forward direction by collecting, with photomultipliers, the Cherenkov light produced. It measures luminosity with the same definition as used for BCM (LUCID_EventOR), with the addition of an event-counting algorithm, requiring a coincidence between the two sides (LUCID_EventAND), and a hit-counting algorithm (LUCID_HitOR), in which the number of photomultipliers providing a signal above threshold is counted. A third method for measuring the per-bunch luminosity is provided by the inner detector. This method counts the number of primary vertices per event, which is proportional to the luminosity. The vertex selection criteria required a minimum of five good-quality tracks with transverse momentum larger than 400 MeV, forming a common vertex [42]. As about 12% of the high- β^* run data were acquired when the high voltage of the ID was lowered for detector-protection reasons, the vertex-based algorithm is not available for that part of the run.

The absolute luminosity scale of each algorithm was calibrated [42] by the van der Meer (*vdM*) method in an intermediate luminosity regime ($L \sim 5 \times 10^{30} \text{ cm}^{-2} \text{ s}^{-1}$). Table 5 lists the integrated luminosity reported by the BCM, LUCID and vertex-based luminosity algorithms (VTX5) during the run analyzed here, both for the full sample and for the fraction during which the ID was fully operational. As for the standard running conditions, BCMV_EventOR was chosen as the preferred algorithm for the luminosity determination, as its response is stable and

Table 5

Integrated luminosity measured using the different algorithms and deviations from the reference value (BCM_V_EventOR). The results are reported for the full data set and for the subset thereof during which the ATLAS ID was fully operational. The uncertainties are statistical only. For LUCID_EventAND, no error is assigned as the luminosity is numerically determined from a formula dependent on the measured event rate.

| Algorithm | $L_{\text{int}} [\mu\text{b}^{-1}]$ | Deviation (%) | $L_{\text{int}} [\mu\text{b}^{-1}]$ | Deviation (%) |
|---------------------------|-------------------------------------|---------------|-------------------------------------|---------------|
| | Full data set | | Data with ID on | |
| BCM _V _EventOR | 78.72 ± 0.13 | – | 69.48 ± 0.12 | – |
| BCM _H _EventOR | 78.10 ± 0.13 | –0.80 | 68.94 ± 0.12 | –0.78 |
| LUCID_EventOR | 77.63 ± 0.04 | –1.38 | 68.55 ± 0.04 | –1.34 |
| LUCID_EventAND | 77.49 | –1.57 | 68.42 | –1.53 |
| LUCID_HitOR | 78.71 ± 0.03 | –0.01 | 69.49 ± 0.03 | +0.01 |
| VTX5 | | | 68.93 ± 0.13 | –0.79 |

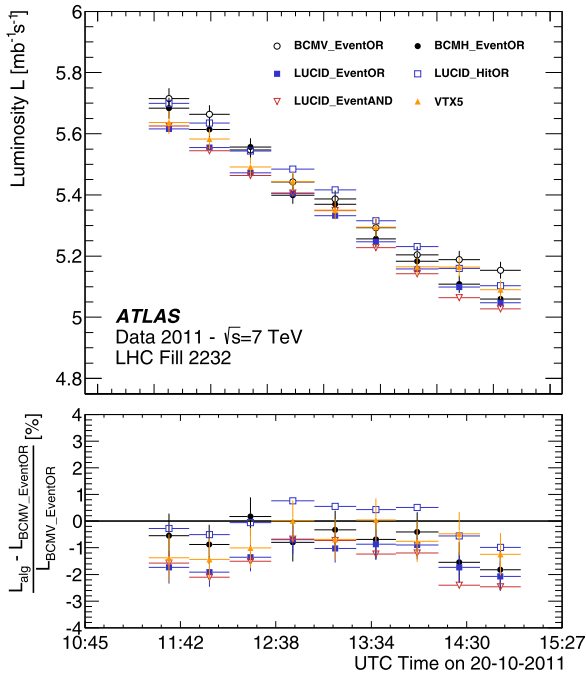


Fig. 13. Luminosity measured by the various algorithms (top) and relative deviations from the reference BCM_V_EventOR algorithm (bottom), as a function of time.

independent of the luminosity scale, from $\sqrt{s}=7$ TeV to high luminosity [42] conditions. Table 5 also reports the fractional deviation of each measurement from the reference value; the largest such difference is 1.6%. In Fig. 13 the luminosity measurements from the various algorithms are shown as a function of time (top), together with the percent deviations from the reference algorithm (bottom).

The contributions to the systematic uncertainty affecting the absolute integrated luminosity during the high- β^* run can be categorized as follows.

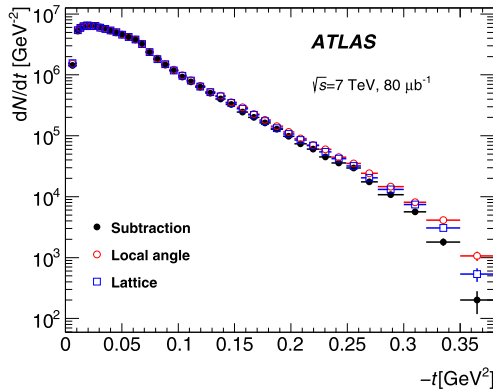


Fig. 14. Counting rate dN/dt as a function of t in arm 1 for different reconstruction methods before corrections. The error bars represent the statistical uncertainty only. The local subtraction method is not shown as it is indistinguishable from the lattice method.

- The uncertainty on the absolute luminosity scale, as determined by the vdM method, amounts to 1.53% [42]. Because it is dominated by beam conditions rather than by instrumental effects, this “scale uncertainty” is common to all luminosity algorithms.
- The “calibration-transfer” uncertainty, associated with transferring the absolute luminosity scale from the intermediate-luminosity regime of the vdM scans to the very low-luminosity conditions of elastic-scattering measurements five months later. It is discussed more extensively below.
- The uncertainty related to the subtraction of beam-associated background during the high- β^* run is estimated to be 0.20%, which results from varying the magnitude of the background correction for the reference algorithm by 80%.

The calibration-transfer uncertainty reflects the uncertainty in the potential shift in BCM response from vdM to high-luminosity conditions (0.25%), the relative long-term stability (0.70%) of the BCM during the several months of high-luminosity running that separate the vdM calibration period from the high- β^* run, and the stability of the LUCID and BCM calibration transfer from the high- to the very low-luminosity regime. While the former two are extensively documented in Ref. [42], the latter is more difficult to assess. The consistency between independent estimates of the integrated luminosity, as quantified in Table 5 by the largest deviation from the reference value (1.6%), is therefore conservatively taken as an upper limit on the systematic uncertainty associated with the third step (high to very-low luminosity) of this calibration transfer.

The total systematic uncertainty on the integrated luminosity L_{int} during the high- β^* run is computed as the sum in quadrature of the scale uncertainty, the overall calibration-transfer uncertainty and the background uncertainty; it amounts to 2.3%. The final result for the selected running period is:

$$L_{\text{int}} = 78.7 \pm 0.1 \text{ (stat.)} \pm 1.9 \text{ (syst.)} \mu\text{b}^{-1}.$$

11. The differential elastic cross section

The raw t -spectrum of elastic-scattering candidates in one detector arm after the event selection is shown in Fig. 14. Different t -reconstruction methods using the effective optics are

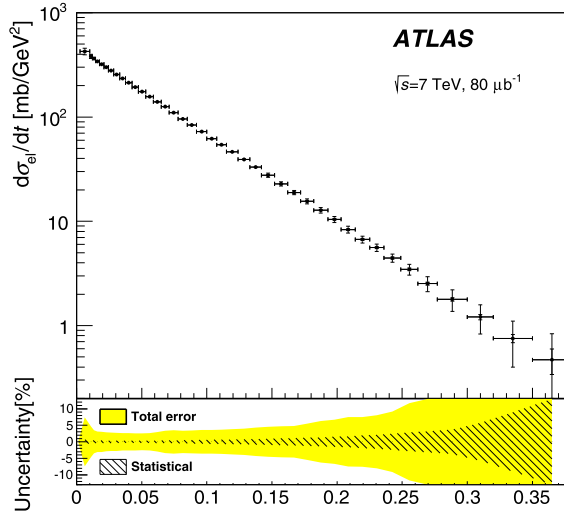


Fig. 15. The differential elastic cross section measured using the subtraction method. The outer error bars indicate the total experimental uncertainty and the inner error bars the statistical uncertainty. The lower panel shows the relative total and statistical uncertainties.

compared. Differences between the methods are visible at large $|t|$, where the resolution effects for methods using the local angle are most important. In order to calculate the differential elastic cross section, several corrections are applied. The corrections are done individually per detector arm and the corrected spectra from the two arms are combined. In a given bin t_i the cross section is calculated according to the following formula:

$$\frac{d\sigma}{dt_i} = \frac{1}{\Delta t_i} \times \frac{\mathcal{M}^{-1}[N_i - B_i]}{A_i \times \epsilon^{\text{reco}} \times \epsilon^{\text{trig}} \times \epsilon^{\text{DAQ}} \times L_{\text{int}}}, \quad (16)$$

where Δt_i is the bin width, \mathcal{M}^{-1} represents the unfolding procedure applied to the background-subtracted number of events $N_i - B_i$, A_i is the acceptance, ϵ^{reco} is the event reconstruction efficiency, ϵ^{trig} is the trigger efficiency, ϵ^{DAQ} is the dead-time correction and L_{int} is the integrated luminosity used for this analysis.

The binning in t is appropriate for the experimental resolution and statistics. At small t the selected bin width is 1.5 times the resolution. At larger $|t|$ the bin width is increased to compensate for the lower number of events from the exponentially falling distribution. The resulting differential elastic cross section using the subtraction method is shown in Fig. 15 with statistical and systematic uncertainties. The numerical values for all bins are summarized in Table 6.

An overview of the contributions to the total uncertainty is given in Fig. 16. Inside the fit range used to extract the total cross section, indicated by vertical lines, the dominant contribution to the uncertainty is the t -independent luminosity error. The statistical error is only a small contribution to the total error. The experimental uncertainty comprises various contributions which are discussed in the following.

11.1. Systematic uncertainties

The following uncertainties are propagated to the differential elastic cross section:

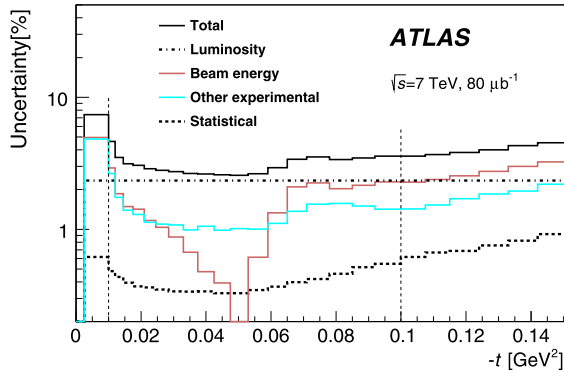


Fig. 16. Relative statistical and systematic uncertainties for the differential elastic cross section for different groups of uncertainties. Only the t -range relevant to the extraction of the total cross section is shown; the vertical lines indicate the fit range.

- The amount of background is varied by the difference between the yields obtained from the anti-golden and the vertex methods. The background shape is varied by the inversion of the sign of the vertical coordinate y on one side of the anti-golden arm, combined with an inversion of the x -coordinate (see Section 7.1).
- The impact of alignment uncertainties is estimated from different sets of the alignment parameter values (see Section 6.2).
- The uncertainties related to the effective optics are obtained by varying the optics constraints, changing the strength of the quadrupoles Q2, Q4, Q5 and Q6 by $\pm 1\%$ and changing only Q5 and Q6 by -2% , as suggested by LHC constraints on the phase advance. Additional uncertainties are determined by varying the quadrupole alignment according to its uncertainty, propagating the fit uncertainties for the strength of Q1 and Q3 to the resulting optics and by taking the difference between the transfer-matrix-based beam transport used in the optics fit and the MadX beam transport (see Section 9).
- The nuclear slope used in the simulation is varied conservatively by $\pm 1 \text{ GeV}^{-2}$ around 19.5 GeV^{-2} (see Section 4).
- The detector resolution is varied, replacing the resolution determined from collision data with values $3\text{--}4 \text{ }\mu\text{m}$ smaller, as predicted from the GEANT4 simulation, and $4\text{--}5 \text{ }\mu\text{m}$ larger, as measured using test-beam data. Additionally, a y -dependent resolution is used instead of a constant value (see Section 4.1).
- The emittance used to calculate the angular divergence in the simulation is varied by $\pm 10\%$ (see Section 5.2).
- The event reconstruction efficiency is varied by its uncertainty discussed in Section 7.3.
- For the tracking efficiency the minimum number of fibre layers required to reconstruct a track is varied between three and six (see Section 6.1).
- The intrinsic unfolding uncertainty is determined from the data-driven closure test in Section 8.
- The impact of a residual beam crossing angle in the horizontal plane of $\pm 10 \text{ }\mu\text{rad}$ is taken into account. This variation is derived from the precision of the beam position monitors.
- The nominal beam energy used in the t -reconstruction according to Eq. (3) is changed by 0.65% [43].
- The luminosity uncertainty of 2.3% is propagated to the cross section (see Section 10).

Table 6

The measured values of the differential elastic cross section with statistical and systematic uncertainties. The central t -values in each bin are calculated from simulation, in which a slope parameter of $B = 19.5 \text{ GeV}^{-2}$ is used.

| Low $ t $ edge [GeV ²] | High $ t $ edge [GeV ²] | Central $ t $ [GeV ²] | $d\sigma_{\text{el}}/dt$ [mb/GeV ²] | Stat. uncert. [mb/GeV ²] | Syst. uncert. [mb/GeV ²] | Total uncert. [mb/GeV ²] |
|---------------------------------------|--|--------------------------------------|--|---|---|---|
| 0.0025 | 0.0100 | 0.0062 | 425.8 | 2.6 | 31.3 | 31.4 |
| 0.0100 | 0.0120 | 0.0110 | 382.6 | 1.9 | 17.7 | 17.8 |
| 0.0120 | 0.0145 | 0.0132 | 363.2 | 1.6 | 12.6 | 12.7 |
| 0.0145 | 0.0175 | 0.0160 | 342.0 | 1.4 | 10.6 | 10.7 |
| 0.0175 | 0.0210 | 0.0192 | 320.9 | 1.2 | 9.7 | 9.8 |
| 0.0210 | 0.0245 | 0.0227 | 300.3 | 1.1 | 8.6 | 8.6 |
| 0.0245 | 0.0285 | 0.0265 | 279.4 | 1.0 | 7.8 | 7.8 |
| 0.0285 | 0.0330 | 0.0307 | 256.1 | 0.9 | 7.0 | 7.0 |
| 0.0330 | 0.0375 | 0.0352 | 234.3 | 0.8 | 6.2 | 6.2 |
| 0.0375 | 0.0425 | 0.0400 | 213.2 | 0.7 | 5.5 | 5.6 |
| 0.0425 | 0.0475 | 0.0450 | 193.3 | 0.6 | 5.0 | 5.0 |
| 0.0475 | 0.0530 | 0.0502 | 175.1 | 0.6 | 4.5 | 4.5 |
| 0.0530 | 0.0590 | 0.0559 | 156.5 | 0.5 | 4.1 | 4.1 |
| 0.0590 | 0.0650 | 0.0619 | 139.8 | 0.5 | 4.1 | 4.1 |
| 0.0650 | 0.0710 | 0.0679 | 125.5 | 0.5 | 4.2 | 4.3 |
| 0.0710 | 0.0780 | 0.0744 | 110.2 | 0.5 | 3.9 | 3.9 |
| 0.0780 | 0.0850 | 0.0814 | 95.8 | 0.4 | 3.2 | 3.2 |
| 0.0850 | 0.0920 | 0.0884 | 83.9 | 0.4 | 2.9 | 2.9 |
| 0.0920 | 0.1000 | 0.0959 | 72.4 | 0.4 | 2.6 | 2.6 |
| 0.1000 | 0.1075 | 0.1037 | 62.0 | 0.4 | 2.2 | 2.2 |
| 0.1075 | 0.1150 | 0.1112 | 54.1 | 0.4 | 2.0 | 2.0 |
| 0.1150 | 0.1240 | 0.1194 | 46.4 | 0.3 | 1.8 | 1.8 |
| 0.1240 | 0.1330 | 0.1284 | 39.2 | 0.3 | 1.5 | 1.6 |
| 0.1330 | 0.1420 | 0.1374 | 33.0 | 0.3 | 1.4 | 1.4 |
| 0.1420 | 0.1520 | 0.1468 | 27.7 | 0.3 | 1.2 | 1.3 |
| 0.1520 | 0.1620 | 0.1568 | 22.8 | 0.2 | 1.1 | 1.1 |
| 0.1620 | 0.1720 | 0.1668 | 18.88 | 0.21 | 0.88 | 0.91 |
| 0.1720 | 0.1820 | 0.1768 | 15.58 | 0.19 | 0.83 | 0.85 |
| 0.1820 | 0.1930 | 0.1873 | 12.77 | 0.17 | 0.79 | 0.80 |
| 0.1930 | 0.2030 | 0.1978 | 10.45 | 0.16 | 0.68 | 0.70 |
| 0.2030 | 0.2140 | 0.2083 | 8.33 | 0.14 | 0.61 | 0.62 |
| 0.2140 | 0.2250 | 0.2193 | 6.70 | 0.13 | 0.49 | 0.50 |
| 0.2250 | 0.2360 | 0.2303 | 5.60 | 0.12 | 0.43 | 0.45 |
| 0.2360 | 0.2490 | 0.2422 | 4.45 | 0.11 | 0.39 | 0.41 |
| 0.2490 | 0.2620 | 0.2553 | 3.46 | 0.10 | 0.39 | 0.40 |
| 0.2620 | 0.2770 | 0.2691 | 2.53 | 0.08 | 0.41 | 0.41 |
| 0.2770 | 0.3000 | 0.2877 | 1.78 | 0.07 | 0.41 | 0.42 |
| 0.3000 | 0.3200 | 0.3094 | 1.21 | 0.07 | 0.37 | 0.38 |
| 0.3200 | 0.3500 | 0.3335 | 0.75 | 0.07 | 0.35 | 0.35 |
| 0.3500 | 0.3800 | 0.3636 | 0.47 | 0.13 | 0.34 | 0.36 |

The systematic uncertainties related to the sources above are calculated by the offset method. In this method, the nominal value of a certain parameter in the analysis chain is varied according to the assigned uncertainty. The shift in bin i for systematic uncertainty source k , $\delta_k(i) = d\sigma_k(i)/dt - d\sigma_{\text{nominal}}(i)/dt$ is recorded, keeping track of the sign and thereby accounting for correlations across the t -spectrum. In total 24 systematic shifts are considered and numerical tables with the shifts can be found in HepData [44]. Systematic shifts are included in the fit used to determine the total cross section, as outlined in Section 12. The most important t -dependent

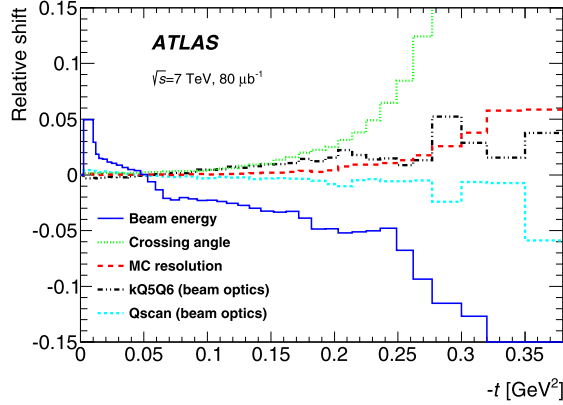


Fig. 17. Relative systematic shifts in the differential elastic cross section as a function of t for selected uncertainty sources. Shown are the uncertainties related to the beam optics (kQ5Q6 and Qscan), to the modelling of the detector resolution in the simulation (MC resolution), to the crossing angle, and to the beam energy. Here kQ5Q6 refers to changing the strength of Q5 and Q6 by -2% and Qscan refers to changing the strength of Q2, Q4, Q5, Q6 by $\pm 1\%$.

shifts are shown in Fig. 17 for the entire range of the t -spectrum; the range used to fit σ_{tot} is from $t = -0.01 \text{ GeV}^2$ to $t = -0.1 \text{ GeV}^2$.

12. The total cross section

The total cross section and the slope parameter B are obtained from a fit of the theoretical spectrum (Eq. (14)), including the Coulomb–nuclear interference term, to the measured differential cross section. The electric form factor $G(t)$, the Coulomb phase $\phi(t)$ and the ρ -parameter are fixed to the nominal values as discussed in Section 4. Both the statistical and systematic uncertainties as well as their correlations are taken into account in the fit. The statistical correlations are included in the covariance matrix calculated in the unfolding procedure. The correlations of systematic uncertainties are taken into account by using a profile minimization procedure [45], where nuisance parameters corresponding to all 24 systematic shifts are included, and the χ^2 is given by:

$$\chi^2 = \sum_{i,j} \left[\left(D(i) - \left(1 + \sum_{l=1}^2 \alpha_l \right) \times T(i) - \sum_{k=1}^{22} \beta_k \times \delta_k(i) \right) \times V^{-1}(i, j) \right. \\ \left. \times \left(D(j) - \left(1 + \sum_{l=1}^2 \alpha_l \right) \times T(j) - \sum_{k=1}^{22} \beta_k \times \delta_k(j) \right) \right] + \sum_{k=1}^{22} \beta_k^2 + \sum_{l=1}^2 \frac{\alpha_l^2}{\epsilon_l^2}, \quad (17)$$

where $D(i)$ is the measured value of the elastic cross section in bin i , $T(i)$ the theoretical prediction and $V(i, j)$ the statistical covariance matrix. For each systematic uncertainty which changes the shape of the t -spectrum, a nuisance parameter β_k multiplying the corresponding shift δ_k is fitted as a free parameter and a penalty term $\sum_k \beta_k^2$ is added to the χ^2 . Two scale parameters, α_l , are used to describe the rescaling of the normalization of the theoretical prediction due to t -independent uncertainties in the luminosity and the reconstruction efficiency. The sum in quadrature of these two scale factors divided by their uncertainties results in a second penalty term, $\sum_l (\alpha_l^2 / \epsilon_l^2)$. Some nuisance parameters in the fit comprise a group of parameter variations. For example, 256 variations of ALFA data constraints by one standard deviation and 256

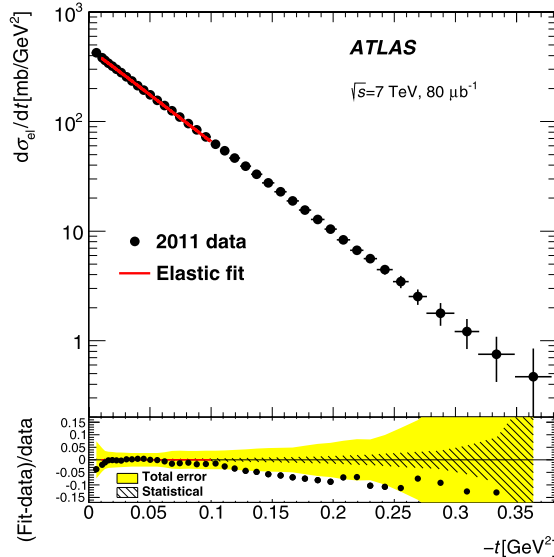


Fig. 18. A fit of the theoretical prediction with σ_{tot} and B as free parameters to the differential elastic cross section reconstructed with the subtraction method. In the lower panel the points represent the normalized difference between fit and data, the yellow area represents the total experimental uncertainty and the hatched area the statistical component. The red line indicates the fit range, the fit result is extrapolated in the lower panel outside the fit range. (For interpretation of the references to color in this figure legend, the reader is referred to the web version of this article.)

quadrupole field variations by $\pm 1\%$ are performed as part of the beam optics uncertainty estimate and are each merged into a single nuisance parameter.

The differential cross section and the fitted theoretical prediction are shown in Fig. 18. The fit range is chosen from $t = -0.01 \text{ GeV}^2$ to $t = -0.1 \text{ GeV}^2$. The lower t value is chosen to be as close as possible to $t = 0$ to reduce the extrapolation uncertainty while having an acceptance above 10%. The choice of the upper limit is motivated by theoretical considerations not to extend the fit into the region where deviations from the single exponential function are expected [46]. The fit yields:

$$\sigma_{\text{tot}} = 95.35 \pm 1.30 \text{ mb}, \quad B = 19.73 \pm 0.24 \text{ GeV}^{-2},$$

where the errors include all statistical and experimental systematic contributions. Systematic uncertainties associated with theoretical parameters and the extrapolation $|t| \rightarrow 0$ are discussed below. The best fit χ^2 is found to be 7.4 for 16 degrees of freedom. Important contributions to the χ^2 are related to the alignment, the beam optics and the nominal beam energy. The results obtained for all t -reconstruction methods are compiled in Table 7 for σ_{tot} and in Table 8 for B .

12.1. Systematic uncertainties

The fit to the t -spectrum accounts for the statistical errors in data and Monte Carlo simulation combined with 24 systematic shifts. The statistical component of the errors given in Table 7 for the total cross section and in Table 8 for B is estimated using pseudo-experiments. The main contributions to the experimental systematic error for the total cross section are the luminosity, nominal beam energy and reconstruction efficiency uncertainties. For B the experimental systematic uncertainty is dominated by the beam energy uncertainty, whereas other experimental

Table 7

The total cross section and uncertainties for four different t -reconstruction methods.

| | σ_{tot} [mb] | | | |
|---------------------|----------------------------|-------------|---------|-------------------|
| | Subtraction | Local angle | Lattice | Local subtraction |
| Total cross section | 95.35 | 95.57 | 95.03 | 94.98 |
| Statistical error | 0.38 | 0.38 | 0.33 | 0.31 |
| Experimental error | 1.25 | 1.36 | 1.30 | 1.30 |
| Extrapolation error | 0.37 | 0.27 | 0.50 | 0.33 |
| Total error | 1.36 | 1.44 | 1.43 | 1.38 |

Table 8

The nuclear slope and uncertainties for four different t -reconstruction methods.

| | B [GeV^{-2}] | | | |
|---------------------|---------------------------|-------------|---------|-------------------|
| | Subtraction | Local angle | Lattice | Local subtraction |
| Nuclear slope | 19.73 | 19.67 | 19.48 | 19.48 |
| Statistical error | 0.14 | 0.15 | 0.14 | 0.15 |
| Experimental error | 0.19 | 0.26 | 0.22 | 0.21 |
| Extrapolation error | 0.17 | 0.17 | 0.26 | 0.18 |
| Total error | 0.29 | 0.35 | 0.37 | 0.31 |

errors such as the luminosity uncertainty change only the normalization and have no impact on the slope.

Additional uncertainties arise from the extrapolation $|t| \rightarrow 0$. These are estimated from a variation of the upper end of the fit range from $-t = 0.1 \text{ GeV}^2$ to $-t = 0.15 \text{ GeV}^2$. The upper end at $-t = 0.15 \text{ GeV}^2$ is chosen in order to remain in a range where a simple exponential is still a reasonable assumption [46]. The upper fit-range edge is also decreased by the same number of bins (six) to $|t| = 0.059 \text{ GeV}^2$ and the symmetrized change is adopted as a systematic uncertainty of approximately 0.4 mb for σ_{tot} and 0.17 GeV^{-2} for B . The fit-range dependence is the dominant source of uncertainty in the extrapolation. As a stability check, the lower end of the fit range is varied, leading to a smaller change of the total cross section, which is not included in the systematic error. Other extrapolation errors are determined from: the variation of the ρ -parameter by ± 0.008 , the replacement of the dipole by a double dipole parameterization for the electric form factor and the replacement of the Coulomb phase from West and Yennie [24] by parameterizations from Refs. [25,31]. All these contributions are small compared to the fit-range variation. The total extrapolation uncertainty is about 0.4 mb for σ_{tot} and 0.2 GeV^{-2} for B . The total errors given in Table 7 for all t -reconstruction methods are very similar and amount to 1.5% of the cross-section value.

Several stability tests were carried out to substantiate the nominal result and its associated uncertainty.

- A fit with only the statistical covariance matrix but ignoring all nuisance parameter contributions was performed. The resulting values are given in Table 9. Because the fit ignores systematic errors the χ^2 is larger.
- The independent samples in each detector arm were corrected and analyzed independently.

Table 9

Fitted values of the total cross section and nuclear slope when only statistical errors are included.

| | Subtraction | Local angle | Lattice | Local subtraction |
|----------------------------|------------------|------------------|------------------|-------------------|
| σ_{tot} [mb] | 95.31 ± 0.12 | 94.96 ± 0.12 | 95.06 ± 0.12 | 95.03 ± 0.11 |
| B [GeV^{-2}] | 19.62 ± 0.05 | 19.44 ± 0.05 | 19.50 ± 0.05 | 19.49 ± 0.05 |
| χ^2/N_{dof} | 2.8 | 1.07 | 1.2 | 1.4 |

- An alternative procedure was performed where all t -dependent corrections and migration effects are applied to the theoretical prediction, which is then fit to the measured raw data.
- The data are split into several sub-samples ordered by time to investigate a potential time dependence of the results.

None of the checks have shown a significant deviation from the nominal results.

12.2. Total inelastic and elastic cross sections

The total elastic cross section is derived from the nuclear scattering term under the assumption that the slope B remains constant over the full t -range. The Coulomb and interference terms are not taken into account. With this approximation the differential elastic cross section is reduced to the exponential form:

$$\frac{d\sigma_{\text{el}}}{dt} = \frac{d\sigma_{\text{el}}}{dt} \Big|_{t=0} \exp(-B|t|) \quad \text{with} \quad \frac{d\sigma_{\text{el}}}{dt} \Big|_{t=0} = \sigma_{\text{tot}}^2 \frac{1 + \rho^2}{16\pi(\hbar c)^2}. \quad (18)$$

The differential cross section at the optical point, $|t| \rightarrow 0$, derived from the total cross-section fit, is: $d\sigma_{\text{el}}/dt|_{t \rightarrow 0} = 474 \pm 4$ (stat.) ± 13 (syst.) mb/GeV^2 , where the systematic uncertainty includes all experimental and extrapolation uncertainties. Integrating the parameterized form of the differential cross section over the full t -range yields the total elastic cross section:

$$\sigma_{\text{el}} = 24.00 \pm 0.19 \text{ (stat.)} \pm 0.57 \text{ (syst.) mb,}$$

where the correlation between σ_{tot} and B , determined from the fit to be approximately 40%, is taken into account in the error calculation. The measured integrated elastic cross section in the fiducial range from $-t = 0.0025 \text{ GeV}^2$ to $-t = 0.38 \text{ GeV}^2$ corresponds to 90% of the total elastic cross section:

$$\sigma_{\text{el}}^{\text{observed}} = 21.66 \pm 0.02 \text{ (stat.)} \pm 0.58 \text{ (syst.) mb.}$$

The total elastic cross section is used to determine the total inelastic cross section by subtraction from the total cross section. The resulting value is:

$$\sigma_{\text{inel}} = 71.34 \pm 0.36 \text{ (stat.)} \pm 0.83 \text{ (syst.) mb.}$$

A summary of the derived quantities with uncertainties is given in [Table 10](#).

12.3. Model dependence of the nuclear amplitude

Traditionally, the nuclear amplitude at small t is parameterized by a single exponential function. This is the canonical form of the t -evolution of the nuclear amplitude and was used by several previous experiments [8–10] to extract the total cross section. At larger t , approaching

Table 10

Measured values of the optical point, extrapolated elastic cross section, inelastic cross section, and observed elastic cross section within fiducial cuts.

| | Optical point [mb/GeV ²] | σ_{el} [mb] | σ_{inel} [mb] | $\sigma_{\text{el}}^{\text{observed}}$ [mb] |
|---------------------|--------------------------------------|---------------------------|-----------------------------|---|
| Result | 474 | 24.00 | 71.34 | 21.66 |
| Statistical error | 4 | 0.19 | 0.36 | 0.02 |
| Experimental error | 12 | 0.57 | 0.72 | 0.58 |
| Extrapolation error | 4 | 0.03 | 0.40 | – |
| Total error | 13 | 0.60 | 0.90 | 0.58 |

Table 11

Fit results for the total cross section for different parameterizations of the t -dependence described in the text. The errors comprise all experimental uncertainties but no theoretical or extrapolation uncertainties.

| | σ_{tot} [mb] | Reference |
|--------------|----------------------------|---------------|
| Nominal | 95.35 ± 1.30 | Eq. (14) |
| Ct^2 | 95.49 ± 1.27 | Refs. [24,49] |
| $c\sqrt{-t}$ | 96.03 ± 1.31 | Ref. [50] |
| SVM | 94.90 ± 1.23 | Ref. [31] |
| BP | 95.49 ± 1.54 | Refs. [51,52] |
| BSW | 95.53 ± 1.38 | Ref. [53] |

the dip around $-t = 0.5 \text{ GeV}^2$ [47], deviations from the exponential form are expected. In order to assess the impact of using a simple exponential for the nuclear amplitude, several alternative forms are investigated. One of the simplest extensions providing a t -dependent slope was used by previous experiments [48] and discussed in Refs. [24,49], and consists of an additional term Ct^2 in the exponential. Another parameterization was recently proposed [50], which considers hadron spin non-flip amplitudes contributing to a non-exponential form through an additional term scaling with $\sqrt{-t}$ in the exponential. The stochastic vacuum model (SVM) [31], which provides an expression for the Coulomb phase, also proposes a parametric form for the differential elastic cross section, assuming constant but possibly different slopes for the real and imaginary amplitudes. While the three forms above are to be used in conjunction with the Coulomb amplitude, other parameterizations exist with even more model-independent parametric forms, partially absorbing Coulomb effects in the parameterization with the use of more free parameters. One of these forms (BP) was proposed in Ref. [51] and more recently modified [52] for the analysis of LHC data, where in total five free parameters are fit. Another model-independent parameterization (BSW) with six free parameters, which allow for normalization, offset and slopes separately for real and imaginary amplitudes, was suggested in Ref. [53].

Since the deviations from the exponential form are expected to increase at larger t , the upper limit of the fit range is increased to $-t = 0.3 \text{ GeV}^2$ when fitting the alternative forms. Only parametric models have been chosen in order to apply the same fit techniques as for the standard analysis.

All alternative forms have at least one more free parameter which improves the quality of the fits at larger t , where best sensitivity for additional parameters is obtained. The various fit results using alternative parameterizations are summarized in Table 11. The profile fit (17) including all systematic errors was used to evaluate the total cross sections. The RMS of the values is in good agreement with the value of 0.4 mb assigned to the extrapolation uncertainty obtained with

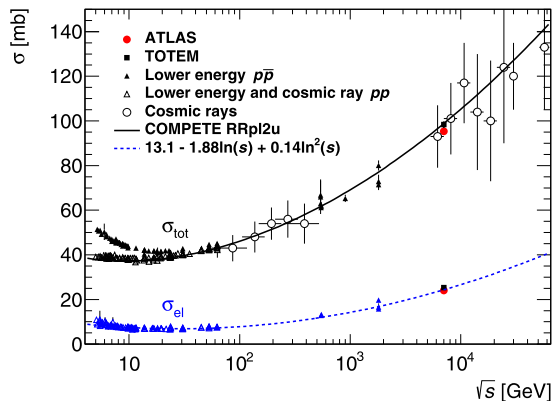


Fig. 19. Comparison of total and elastic cross-section measurements presented here with other published measurements [11,29,55–58] and model predictions as function of the centre-of-mass energy.

the simple exponential form as described in Section 12.1. Similar results are obtained for all t -reconstruction methods.

13. Discussion

The result for the total hadronic cross section presented here, $\sigma_{\text{tot}} = 95.35 \pm 1.36$ mb, can be compared to the most precise value measured by TOTEM, in the same LHC fill using a luminosity-dependent analysis, $\sigma_{\text{tot}} = 98.6 \pm 2.2$ mb [11]. Assuming the uncertainties are uncorrelated, the difference between the ATLAS and TOTEM values corresponds to 1.3σ . The uncertainty on the TOTEM result is dominated by the luminosity uncertainty of $\pm 4\%$, giving a ± 2 mb contribution to σ_{tot} through the square root dependence of σ_{tot} on luminosity. The measurement reported here profits from a smaller luminosity uncertainty of only $\pm 2.3\%$. In subsequent publications [16,54] TOTEM has used the same data to perform a luminosity-independent measurement of the total cross section using a simultaneous determination of elastic and inelastic event yields. In addition, TOTEM made a ρ -independent measurement without using the optical theorem by summing directly the elastic and inelastic cross sections [16]. The three TOTEM results are consistent with one another.

The results presented here are compared in Fig. 19 to the result of TOTEM and are also compared with results of experiments at lower energy [29] and with cosmic ray experiments [55–58]. The measured total cross section is furthermore compared to the best fit to the energy evolution of the total cross section from the COMPETE Collaboration [26] assuming an energy dependence of $\ln^2 s$. The elastic measurement is in turn compared to a second order polynomial fit in $\ln s$ of the elastic cross sections. The value of σ_{tot} reported here is two standard deviations below the COMPETE parameterization. Some other models prefer a somewhat slower increase of the total cross section with energy, predicting values below 95 mb, and thus agree slightly better with the result reported here [59–61].

The value of the nuclear slope parameter $B = 19.73 \pm 0.29$ GeV^{-2} reported here is in good agreement with the TOTEM measurement of 19.89 ± 0.27 GeV^{-2} [11]. These large values of the B -parameter confirm that elastically scattered protons continue to be confined to a gradually narrowing cone as the energy increases as can be seen from Fig. 20. The B -parameter is related to the proton radius and as for the total cross section an increase can be expected at higher energies.

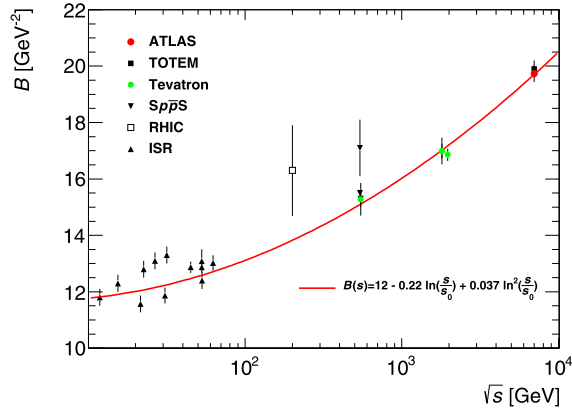


Fig. 20. Comparison of the measurement of the nuclear slope B presented here with other published measurements at the ISR [63–66], at the Sp \bar{p} S [67–69], at RHIC [70], at the Tevatron [9,71,72] and with the measurement from TOTEM [11] at the LHC. The red line shows the calculation from Ref. [62], which contains a linear and quadratic term in $\ln s$.

As outlined in Ref. [62], the evolution of B from ISR to LHC energies is more compatible with a quadratic than a linear dependence in $\ln s$.

The elastic cross section is measured to be 24.0 ± 0.6 mb. This is in agreement with the TOTEM result of 25.4 ± 1.1 mb within 1.1σ . The ratio of the elastic cross section to the total cross section is often taken as a measure of the opacity of the proton. Measurements shed light on whether the black disc limit of a ratio of 0.5 is being approached. It is interesting to note that although there are some small differences between ATLAS and TOTEM for the total and elastic cross sections, the ratio $\sigma_{\text{el}}/\sigma_{\text{tot}}$ is very similar. The TOTEM value is $\sigma_{\text{el}}/\sigma_{\text{tot}} = 0.257 \pm 0.005$ [16,54], while the measurement reported here gives $\sigma_{\text{el}}/\sigma_{\text{tot}} = 0.252 \pm 0.004$. All derived measurements depend on σ_{tot} and B and are therefore highly correlated.

Finally, various total inelastic cross-section measurements, either using only elastic data as in the present analysis and in the corresponding analysis of TOTEM [11], or using elastic and inelastic data in the luminosity-independent method [16], are compared in Fig. 21 to direct measurements by TOTEM [54], ALICE [73] and an ATLAS [14] result based upon an analysis of minimum bias events. In general, the direct measurements have a larger uncertainty because of the model dependence when extrapolating to the unobservable cross section at low diffractive masses. A measurement from CMS [74] was not extrapolated to the total inelastic cross section and is therefore not included in Fig. 21. The measurement of $\sigma_{\text{inel}} = 71.34 \pm 0.90$ mb reported here improves considerably the previous measurement of ATLAS: $\sigma_{\text{inel}} = 69.4 \pm 7.3$ mb [14].

As mentioned above, the previous ATLAS result for the inelastic cross section has a large uncertainty because of the uncertainty in the extrapolation to low diffractive masses outside the fiducial region. The fiducial region covers only dissociative processes with the diffractive invariant mass, M_X , larger than 15.7 GeV. However, the precision of the measurement in the fiducial region is good, with an uncertainty on the fiducial cross section roughly three times smaller than on the extrapolated inelastic cross section. Thus by taking the difference of the present measurement of the total inelastic cross section and the previous measurement by ATLAS in the fiducial region the size of the cross section for invariant masses below 15.7 GeV can be estimated and compared with existing models. The cross section measured by ATLAS corresponding to masses above 15.7 GeV is 60.3 ± 2.1 mb [14]. Thus the cross section in which the dissociative systems have an invariant mass M_X less than 15.7 GeV is estimated to be 11.0 ± 2.3 mb. Both

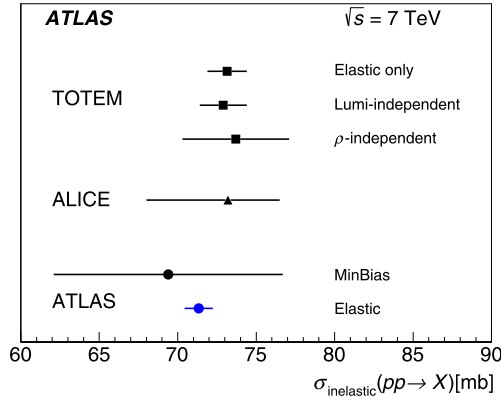


Fig. 21. Comparison of the inelastic cross section presented here with the earlier ATLAS measurement [14] and published data from ALICE [73] and TOTEM [11,16,54].

PYTHIA and PHOJET [75,76] predict significantly lower contributions to the inelastic cross section in this range of invariant masses, approximately 6 mb and 3 mb respectively. The model of Ref. [60] gives a better description of the data with values in the range 11–14 mb (see discussion in Ref. [77]).

14. Summary

In this paper a measurement of the elastic pp cross section and the determination of the total cross section using the optical theorem at $\sqrt{s} = 7$ TeV by the ATLAS experiment at the LHC with the ALFA sub-detector is presented. The data were recorded in 2011 during a special run with high- β^* optics, where an integrated luminosity of $80 \mu\text{b}^{-1}$ was accumulated. The analysis uses data-driven methods to determine relevant beam optics parameters, event reconstruction efficiency and to tune the simulation. A key element of this analysis is the determination of the effective beam optics, which takes into account measurements from ALFA that are sensitive to ratios of transport matrix elements and calibration uncertainties of the quadrupoles. A detailed evaluation of the associated systematic uncertainties includes the comparison of different t -reconstruction methods that are sensitive to different transport matrix elements. A dedicated effort was made to determine the absolute luminosity for this run while taking into account the special conditions with a very low number of interactions per bunch crossing. From a fit to the differential elastic cross section, using the optical theorem, the total cross section is determined to be:

$$\sigma_{\text{tot}}(pp \rightarrow X) = 95.35 \pm 0.38 \text{ (stat.)} \pm 1.25 \text{ (exp.)} \pm 0.37 \text{ (extr.) mb,}$$

where the first error is statistical, the second accounts for all experimental systematic uncertainties and the last is related to uncertainties on the extrapolation to $|t| \rightarrow 0$. The experimental systematic uncertainty is dominated by the uncertainty on the luminosity and on the nominal beam energy. Further experimental uncertainties including those associated with beam optics and detector modelling contribute less. Alternative models for the nuclear amplitude parameterization with non-exponential contributions were investigated using an extended fit range and the resulting values of the total cross section range from 94.9 mb to 96.0 mb.

In addition the slope of the elastic differential cross section at small t was determined to be:

$$B = 19.73 \pm 0.14 \text{ (stat.)} \pm 0.26 \text{ (syst.) GeV}^{-2}.$$

From the fitted parameterization of the elastic cross section the total elastic cross section is extracted:

$$\sigma_{\text{el}}(pp \rightarrow pp) = 24.00 \pm 0.19 \text{ (stat.)} \pm 0.57 \text{ (syst.) mb,}$$

and by subtraction from the total cross section the inelastic cross section is determined to be:

$$\sigma_{\text{inel}} = 71.34 \pm 0.36 \text{ (stat.)} \pm 0.83 \text{ (syst.) mb,}$$

which is significantly more precise than the previous direct ATLAS measurement.

Acknowledgements

We thank CERN for the very successful operation of the LHC, as well as the support staff from our institutions without whom ATLAS could not be operated efficiently. We are indebted to the beam optics development team, led by H. Burkhardt, for the design, commissioning and thorough operation of the high- β^* optics in dedicated LHC fills.

We acknowledge the support of ANPCyT, Argentina; YerPhI, Armenia; ARC, Australia; BMFWF and FWF, Austria; ANAS, Azerbaijan; SSTC, Belarus; CNPq and FAPESP, Brazil; NSERC, NRC and CFI, Canada; CERN; CONICYT, Chile; CAS, MOST and NSFC, China; COLCIENCIAS, Colombia; MSMT CR, MPO CR and VSC CR, Czech Republic; DNRF, DNSRC and Lundbeck Foundation, Denmark; EPLANET, ERC and NSRF, European Union; IN2P3-CNRS, CEA-DSM/IRFU, France; GNSF, Georgia; BMBF, DFG, HGF, MPG and AvH Foundation, Germany; GSRT and NSRF, Greece; ISF, MINERVA, GIF, I-CORE and Benozzi Center, Israel; INFN, Italy; MEXT and JSPS, Japan; CNRST, Morocco; FOM and NWO, Netherlands; BRF and RCN, Norway; MNiSW and NCN, Poland; GRICES and FCT, Portugal; MNE/IFA, Romania; MES of Russia and ROSATOM, Russian Federation; JINR; MSTD, Serbia; MSSR, Slovakia; ARRS and MIZŠ, Slovenia; DST/NRF, South Africa; MINECO, Spain; SRC and Wallenberg Foundation, Sweden; SER, SNSF and Cantons of Bern and Geneva, Switzerland; NSC, Taiwan; TAEK, Turkey; STFC, the Royal Society and Leverhulme Trust, United Kingdom; DOE and NSF, United States of America.

The crucial computing support from all WLCG partners is acknowledged gratefully, in particular from CERN and the ATLAS Tier-1 facilities at TRIUMF (Canada), NDGF (Denmark, Norway, Sweden), CC-IN2P3 (France), KIT/GridKA (Germany), INFN-CNAF (Italy), NL-T1 (Netherlands), PIC (Spain), ASGC (Taiwan), RAL (UK) and BNL (USA) and in the Tier-2 facilities worldwide.

References

- [1] M. Froissart, *Phys. Rev.* 123 (1961) 1053.
- [2] A. Martin, *Nuovo Cimento A* 10 (42) (1966) 930.
- [3] S.R. Amendolia, et al., *Phys. Lett. B* 44 (1973) 119.
- [4] U. Amaldi, et al., *Phys. Lett. B* 44 (1973) 112.
- [5] M. Bozzo, et al., UA4 Collaboration, *Phys. Lett. B* 147 (1984) 392.
- [6] C. Augier, et al., UA4/2 Collaboration, *Phys. Lett. B* 344 (1995) 451.
- [7] N.A. Amos, et al., E710 Collaboration, *Phys. Lett. B* 243 (1990) 158.
- [8] C. Avila, et al., E811 Collaboration, *Phys. Lett. B* 445 (1999) 419.
- [9] F. Abe, et al., CDF Collaboration, *Phys. Rev. D* 50 (1994) 5518.
- [10] G. Antchev, et al., TOTEM Collaboration, *Europhys. Lett.* 96 (2011) 21002, arXiv:1110.1395.

- [11] G. Antchev, et al., TOTEM Collaboration, *Europhys. Lett.* 101 (2013) 21002.
- [12] ATLAS Collaboration, *J. Instrum.* 3 (2008) S08003.
- [13] S. van der Meer, *ISR-PO-68-31*, <http://cds.cern.ch/record/296752>, 1968.
- [14] ATLAS Collaboration, *Nat. Commun.* 2 (2011) 463, arXiv:1104.0326.
- [15] G. Antchev, et al., TOTEM Collaboration, *Phys. Rev. Lett.* 111 (2013) 012001, arXiv:1308.6722.
- [16] G. Antchev, et al., TOTEM Collaboration, *Europhys. Lett.* 101 (2013) 21004.
- [17] F. Anghinolfi, et al., *J. Instrum.* 2 (2007) P07004, arXiv:0706.3316.
- [18] S. Ask, et al., *Nucl. Instrum. Methods Phys. Res., Sect. A, Accel. Spectrom. Detect. Assoc. Equip.* 568 (2006) 588, arXiv:physics/0605127.
- [19] P. Barrillon, et al., *Nucl. Instrum. Methods Phys. Res., Sect. A, Accel. Spectrom. Detect. Assoc. Equip.* 623 (2010) 463.
- [20] S. Blin, P. Barrillon, C. de La Taille, *IEEE Nucl. Sci. Symp. Conf. Rec.* 2010 (2010) 1690–1693.
- [21] H. Burkhardt, et al., *Conf. Proc. C* 1205201 (2012) 130.
- [22] H. Burkhardt, S. Cavalier, P. Puzo, A. Peskov, *Conf. Proc. C* 110904 (2011) 1798.
- [23] H.A. Bethe, *Ann. Phys.* 3 (1958) 190.
- [24] G.B. West, D.R. Yennie, *Phys. Rev.* 172 (1968) 1413.
- [25] R.N. Cahn, *Z. Phys. C* 15 (1982) 253.
- [26] J. Cudell, et al., COMPETE Collaboration, *Phys. Rev. Lett.* 89 (2002) 201801, arXiv:hep-ph/0206172.
- [27] W.M. Yao, et al., Particle Data Group, *J. Phys. G* 33 (2006) 1.
- [28] A. Alkin, J.R. Cudell, E. Martinov, *Few-Body Syst.* 53 (2012) 87, arXiv:1109.1306.
- [29] J. Beringer, et al., Particle Data Group, *Phys. Rev. D* 86 (2012) 010001.
- [30] M.J. Menon, P.V.R.G. Silva, *J. Phys. G* 40 (2013) 125001, arXiv:1305.2947;
M.J. Menon, P.V.R.G. Silva, *J. Phys. G* 41 (2014) 019501 (Erratum).
- [31] A.K. Kohara, E. Ferreira, T. Kodama, *Eur. Phys. J. C* 73 (2013) 2326, arXiv:1212.3652.
- [32] G.G. Simon, C. Schmitt, F. Borkowski, V.H. Walther, *Nucl. Phys. A* 333 (1980) 381.
- [33] J.C. Bernauer, et al., A1 Collaboration, *Phys. Rev. C* 90 (2014) 015206, arXiv:1307.6227.
- [34] T. Sjöstrand, S. Mrenna, P. Skands, *Comput. Phys. Commun.* 178 (2008) 852, arXiv:0710.3820.
- [35] T. Sjöstrand, S. Mrenna, P. Skands, *J. High Energy Phys.* 05 (2006) 026, arXiv:hep-ph/0603175.
- [36] CERN Accelerator Beam Physics Group, MAD – methodical accelerator design, <http://mad.web.cern.ch/mad/>, 2014.
- [37] J. Allison, et al., *IEEE Trans. Nucl. Sci.* 53 (2006) 270.
- [38] S. Agostinelli, et al., GEANT4, *Nucl. Instrum. Methods Phys. Res., Sect. A, Accel. Spectrom. Detect. Assoc. Equip.* 506 (2003) 250.
- [39] G. Baud, et al., CERN-ACC-2013-0308, <http://cds.cern.ch/record/1638354>, 2013.
- [40] B. Malaescu, CERN-PH-EP-2011-111, <http://cds.cern.ch/record/1365693>, arXiv:1106.3107, 2011.
- [41] A. Höcker, V.G. Kartvelishvili, *Nucl. Instrum. Methods Phys. Res., Sect. A, Accel. Spectrom. Detect. Assoc. Equip.* 372 (1996) 469, arXiv:hep-ph/9509307.
- [42] ATLAS Collaboration, *Eur. Phys. J. C* 73 (2013) 2518, arXiv:1302.4393.
- [43] J. Wenninger, Energy calibration of the LHC beams at 4 TeV, CERN-ATS-2013-040, <http://cds.cern.ch/record/1546734>, 2013.
- [44] The Durham HepData Project, <http://hepdata.cedar.ac.uk/>, 2014.
- [45] V. Blobel, eConf C 030908 (2003), MOET002, <http://www.slac.stanford.edu/econf/C030908/proceedings.html>.
- [46] V.A. Khoze, A.D. Martin, M.G. Ryskin, *Eur. Phys. J. C* 18 (2000) 167, arXiv:hep-ph/0007359.
- [47] G. Antchev, et al., TOTEM Collaboration, *Europhys. Lett.* 95 (2011) 41001, arXiv:1110.1385.
- [48] N.A. Amos, et al., E710 Collaboration, *Phys. Lett. B* 247 (1990) 127.
- [49] M.M. Block, R.N. Cahn, *Czechoslov. J. Phys.* 40 (1990) 164.
- [50] O.V. Selyugin, *Nucl. Phys. A* 922 (2014) 180, arXiv:1312.1271.
- [51] R.J.N. Phillips, V.D. Barger, *Phys. Lett. B* 46 (1973) 412.
- [52] D.A. Fagundes, et al., *Phys. Rev. D* 88 (2013) 094019, arXiv:1306.0452.
- [53] C. Bourrely, J. Soffer, T.T. Wu, *Eur. Phys. J. C* 71 (2011) 1601, arXiv:1011.1756.
- [54] G. Antchev, et al., TOTEM Collaboration, *Europhys. Lett.* 101 (2013) 21003.
- [55] P. Abreu, et al., Pierre Auger Collaboration, *Phys. Rev. Lett.* 109 (2012) 062002, arXiv:1208.1520.
- [56] G. Aielli, et al., ARGO-YBJ Collaboration, *Phys. Rev. D* 80 (2009) 092004, arXiv:0904.4198.
- [57] M. Honda, et al., *Phys. Rev. Lett.* 70 (1993) 525.
- [58] R.M. Baltrusaitis, et al., *Phys. Rev. Lett.* 52 (1984) 1380.
- [59] M.M. Block, F. Halzen, *Phys. Rev. D* 86 (2012) 051504, arXiv:1208.4086.

- [60] M.G. Ryskin, A.D. Martin, V.A. Khoze, *Eur. Phys. J. C* 71 (2011) 1617, arXiv:1102.2844.
 [61] J. Soffer, *AIP Conf. Proc.* 1523 (2013) 115, arXiv:1302.5045.
 [62] V.A. Schegelsky, M.G. Ryskin, *Phys. Rev. D* 85 (2012) 094024, arXiv:1112.3243.
 [63] U. Amaldi, et al., CERN–Pisa–Rome–Stony Brook Collaboration, *Phys. Lett. B* 62 (1976) 460.
 [64] G. Barbiellini, et al., *Phys. Lett. B* 39 (1972) 663.
 [65] N.A. Amos, et al., *Nucl. Phys. B* 262 (1985) 689.
 [66] M. Ambrosio, et al., CERN–Naples–Pisa–Stony Brook Collaboration, *Phys. Lett. B* 115 (1982) 495.
 [67] M. Bozzo, et al., UA4 Collaboration, *Phys. Lett. B* 147 (1984) 385.
 [68] G. Arnison, et al., UA1 Collaboration, *Phys. Lett. B* 128 (1983) 336.
 [69] C. Augier, et al., UA4/2 Collaboration, *Phys. Lett. B* 316 (1993) 448.
 [70] S.L. Bueltmann, et al., PP2PP Collaboration, *Phys. Lett. B* 579 (2004) 245, arXiv:nucl-ex/0305012.
 [71] N.A. Amos, et al., E710 Collaboration, *Phys. Rev. Lett.* 68 (1992) 2433.
 [72] V.M. Abazov, et al., D0 Collaboration, *Phys. Rev. D* 86 (2012) 012009.
 [73] B. Abelev, et al., ALICE Collaboration, *Eur. Phys. J. C* 73 (2013) 2456, arXiv:1208.4968.
 [74] CMS Collaboration, *Phys. Lett. B* 722 (2013) 5, arXiv:1210.6718.
 [75] R. Engel, *Z. Phys. C* 66 (1995) 203.
 [76] F.W. Bopp, R. Engel, J. Ranft, *Conf. Proc. LISHEP98* (1998) 729, arXiv:hep-ph/9803437.
 [77] ATLAS Collaboration, *Eur. Phys. J. C* 72 (2012) 1926, arXiv:1201.2808.

ATLAS Collaboration

G. Aad⁸⁴, B. Abbott¹¹², J. Abdallah¹⁵², S. Abdel Khalek¹¹⁶,
 O. Abidinov¹¹, R. Aben¹⁰⁶, B. Abi¹¹³, M. Abolins⁸⁹, O.S. AbouZeid¹⁵⁹,
 H. Abramowicz¹⁵⁴, H. Abreu¹⁵³, R. Abreu³⁰, Y. Abulaiti^{147a,147b},
 B.S. Acharya^{165a,165b,a}, L. Adamczyk^{38a}, D.L. Adams²⁵, J. Adelman¹⁷⁷,
 S. Adomeit⁹⁹, T. Adye¹³⁰, T. Agatonovic-Jovin^{13a},
 J.A. Aguilar-Saavedra^{125a,125f}, M. Agustoni¹⁷, S.P. Ahlen²²,
 F. Ahmadov^{64,b}, G. Aielli^{134a,134b}, H. Akerstedt^{147a,147b}, T.P.A. Åkesson⁸⁰,
 G. Akimoto¹⁵⁶, A.V. Akimov⁹⁵, G.L. Alberghi^{20a,20b}, J. Albert¹⁷⁰,
 S. Albrand⁵⁵, M.J. Alconada Verzini⁷⁰, M. Aleksa³⁰, I.N. Aleksandrov⁶⁴,
 C. Alexa^{26a}, G. Alexander¹⁵⁴, G. Alexandre⁴⁹, T. Alexopoulos¹⁰,
 M. Alhroob^{165a,165c}, G. Alimonti^{90a}, L. Alio⁸⁴, J. Alison³¹,
 B.M.M. Allbrooke¹⁸, L.J. Allison⁷¹, P.P. Allport⁷³, J. Almond⁸³,
 A. Aloisio^{103a,103b}, A. Alonso³⁶, F. Alonso⁷⁰, C. Alpigiani⁷⁵,
 A. Altheimer³⁵, B. Alvarez Gonzalez⁸⁹, M.G. Alviggi^{103a,103b},
 K. Amako⁶⁵, Y. Amaral Coutinho^{24a}, C. Amelung²³, D. Amidei⁸⁸,
 S.P. Amor Dos Santos^{125a,125c}, A. Amorim^{125a,125b}, S. Amoroso⁴⁸,
 N. Amram¹⁵⁴, G. Amundsen²³, C. Anastopoulos¹⁴⁰, L.S. Ancu⁴⁹,
 N. Andari³⁰, T. Andeen³⁵, C.F. Anders^{58b}, G. Anders³⁰, K.J. Anderson³¹,
 A. Andreazza^{90a,90b}, V. Andrei^{58a}, X.S. Anduaga⁷⁰, S. Angelidakis⁹,
 I. Angelozzi¹⁰⁶, P. Anger⁴⁴, A. Angerami³⁵, F. Anghinolfi³⁰,
 A.V. Anisenkov^{108,c}, N. Anjos^{125a}, A. Annovi⁴⁷, A. Antonaki⁹,
 M. Antonelli⁴⁷, A. Antonov⁹⁷, J. Antos^{145b}, F. Anulli^{133a}, M. Aoki⁶⁵,
 L. Aperio Bella¹⁸, R. Apolle^{119,d}, G. Arabidze⁸⁹, I. Aracena¹⁴⁴, Y. Arai⁶⁵,
 J.P. Araque^{125a}, A.T.H. Arce⁴⁵, J-F. Arguin⁹⁴, S. Argyropoulos⁴²,

M. Arik ^{19a}, A.J. Armbruster ³⁰, O. Arnaez ³⁰, V. Arnal ⁸¹, H. Arnold ⁴⁸,
 M. Arratia ²⁸, O. Arslan ²¹, A. Artamonov ⁹⁶, G. Artoni ²³, S. Asai ¹⁵⁶,
 N. Asbah ⁴², A. Ashkenazi ¹⁵⁴, B. Åsman ^{147a,147b}, L. Asquith ⁶,
 K. Assamagan ²⁵, R. Astalos ^{145a}, M. Atkinson ¹⁶⁶, N.B. Atlay ¹⁴²,
 B. Auerbach ⁶, K. Augsten ¹²⁷, M. Auresseau ^{146b}, G. Avolio ³⁰,
 G. Azuelos ^{94,e}, Y. Azuma ¹⁵⁶, M.A. Baak ³⁰, A.E. Baas ^{58a},
 C. Bacci ^{135a,135b}, H. Bachacou ¹³⁷, K. Bachas ¹⁵⁵, M. Backes ³⁰,
 M. Backhaus ³⁰, J. Backus Mayes ¹⁴⁴, E. Badescu ^{26a}, P. Bagiacchi ^{133a,133b},
 P. Bagnaia ^{133a,133b}, Y. Bai ^{33a}, T. Bain ³⁵, J.T. Baines ¹³⁰, O.K. Baker ¹⁷⁷,
 P. Balek ¹²⁸, F. Balli ¹³⁷, E. Banas ³⁹, Sw. Banerjee ¹⁷⁴, A.A.E. Bannoura ¹⁷⁶,
 V. Bansal ¹⁷⁰, H.S. Bansil ¹⁸, L. Barak ¹⁷³, S.P. Baranov ⁹⁵, E.L. Barberio ⁸⁷,
 D. Barberis ^{50a,50b}, M. Barbero ⁸⁴, T. Barillari ¹⁰⁰, M. Barisonzi ¹⁷⁶,
 T. Barklow ¹⁴⁴, N. Barlow ²⁸, B.M. Barnett ¹³⁰, R.M. Barnett ¹⁵,
 Z. Barnovska ⁵, A. Baroncelli ^{135a}, G. Barone ⁴⁹, A.J. Barr ¹¹⁹,
 F. Barreiro ⁸¹, J. Barreiro Guimarães da Costa ⁵⁷, R. Bartoldus ¹⁴⁴,
 A.E. Barton ⁷¹, P. Bartos ^{145a}, V. Bartsch ¹⁵⁰, A. Bassalat ¹¹⁶, A. Basye ¹⁶⁶,
 R.L. Bates ⁵³, J.R. Batley ²⁸, M. Battaglia ¹³⁸, M. Battistin ³⁰, F. Bauer ¹³⁷,
 H.S. Bawa ^{144,f}, M.D. Beattie ⁷¹, T. Beau ⁷⁹, P.H. Beauchemin ¹⁶²,
 R. Beccherle ^{123a,123b}, P. Bechtel ²¹, H.P. Beck ^{17,g}, K. Becker ¹⁷⁶,
 S. Becker ⁹⁹, M. Beckingham ¹⁷¹, C. Becot ¹¹⁶, A.J. Beddall ^{19c},
 A. Beddall ^{19c}, S. Bedikian ¹⁷⁷, V.A. Bednyakov ⁶⁴, C.P. Bee ¹⁴⁹,
 L.J. Beemster ¹⁰⁶, T.A. Beermann ¹⁷⁶, M. Begel ²⁵, K. Behr ¹¹⁹,
 C. Belanger-Champagne ⁸⁶, P.J. Bell ⁴⁹, W.H. Bell ⁴⁹, G. Bella ¹⁵⁴,
 L. Bellagamba ^{20a}, A. Bellerive ²⁹, M. Bellomo ⁸⁵, K. Belotskiy ⁹⁷,
 O. Beltramello ³⁰, O. Benary ¹⁵⁴, D. Benchekroun ^{136a}, K. Bendtz ^{147a,147b},
 N. Benekos ¹⁶⁶, Y. Benhammou ¹⁵⁴, E. Benhar Noccioli ⁴⁹,
 J.A. Benitez Garcia ^{160b}, D.P. Benjamin ⁴⁵, J.R. Bensinger ²³,
 K. Benslama ¹³¹, S. Bentvelsen ¹⁰⁶, D. Berge ¹⁰⁶,
 E. Bergeaas Kuutmann ¹⁶⁷, N. Berger ⁵, F. Berghaus ¹⁷⁰, J. Beringer ¹⁵,
 C. Bernard ²², P. Bernat ⁷⁷, C. Bernius ⁷⁸, F.U. Bernlochner ¹⁷⁰, T. Berry ⁷⁶,
 P. Berta ¹²⁸, C. Bertella ⁸⁴, G. Bertoli ^{147a,147b}, F. Bertolucci ^{123a,123b},
 C. Bertsche ¹¹², D. Bertsche ¹¹², M.I. Besana ^{90a}, G.J. Besjes ¹⁰⁵,
 O. Bessidskaia ^{147a,147b}, M. Bessner ⁴², N. Besson ¹³⁷, C. Betancourt ⁴⁸,
 S. Bethke ¹⁰⁰, W. Bhimji ⁴⁶, R.M. Bianchi ¹²⁴, L. Bianchini ²³,
 M. Bianco ³⁰, O. Biebel ⁹⁹, S.P. Bieniek ⁷⁷, K. Bierwagen ⁵⁴, J. Biesiada ¹⁵,
 M. Biglietti ^{135a}, J. Bilbao De Mendizabal ⁴⁹, H. Bilokon ⁴⁷, M. Bindi ⁵⁴,
 S. Binet ¹¹⁶, A. Bingul ^{19c}, C. Bini ^{133a,133b}, C.W. Black ¹⁵¹, J.E. Black ¹⁴⁴,

K.M. Black²², D. Blackburn¹³⁹, R.E. Blair⁶, J.-B. Blanchard¹³⁷,
 T. Blazek^{145a}, I. Bloch⁴², C. Blocker²³, W. Blum^{82,*}, U. Blumenschein⁵⁴,
 G.J. Bobbink¹⁰⁶, V.S. Bobrovnikov^{108,c}, S.S. Bocchetta⁸⁰, A. Bocci⁴⁵,
 C. Bock⁹⁹, C.R. Boddy¹¹⁹, M. Boehler⁴⁸, T.T. Boek¹⁷⁶, J.A. Bogaerts³⁰,
 A.G. Bogdanchikov¹⁰⁸, A. Bogouch^{91,*}, C. Bohm^{147a}, J. Bohm¹²⁶,
 V. Boisvert⁷⁶, T. Bold^{38a}, V. Boldea^{26a}, A.S. Boldyrev⁹⁸, M. Bomben⁷⁹,
 M. Bona⁷⁵, M. Boonekamp¹³⁷, A. Borisov¹²⁹, G. Borissov⁷¹, M. Borri⁸³,
 S. Borroni⁴², J. Bortfeldt⁹⁹, V. Bortolotto^{135a,135b}, K. Bos¹⁰⁶,
 D. Boscherini^{20a}, M. Bosman¹², H. Boterenbrood¹⁰⁶, J. Boudreau¹²⁴,
 J. Bouffard², E.V. Bouhova-Thacker⁷¹, D. Boumediene³⁴,
 C. Bourdarios¹¹⁶, N. Bousson¹¹³, S. Boutouil^{136d}, A. Boveia³¹, J. Boyd³⁰,
 I.R. Boyko⁶⁴, I. Bozic^{13a}, J. Bracinik¹⁸, A. Brandt⁸, G. Brandt¹⁵,
 O. Brandt^{58a}, U. Bratzler¹⁵⁷, B. Brau⁸⁵, J.E. Brau¹¹⁵, H.M. Braun^{176,*},
 S.F. Brazzale^{165a,165c}, B. Brelier¹⁵⁹, K. Brendlinger¹²¹, A.J. Brennan⁸⁷,
 R. Brenner¹⁶⁷, S. Bressler¹⁷³, K. Bristow^{146c}, T.M. Bristow⁴⁶,
 D. Britton⁵³, F.M. Brochu²⁸, I. Brock²¹, R. Brock⁸⁹, C. Bromberg⁸⁹,
 J. Bronner¹⁰⁰, G. Brooijmans³⁵, T. Brooks⁷⁶, W.K. Brooks^{32b},
 J. Brosamer¹⁵, E. Brost¹¹⁵, J. Brown⁵⁵, P.A. Bruckman de Renstrom³⁹,
 D. Bruncko^{145b}, R. Bruneliere⁴⁸, S. Brunet⁶⁰, A. Bruni^{20a}, G. Bruni^{20a},
 M. Bruschi^{20a}, L. Bryngemark⁸⁰, T. Buanes¹⁴, Q. Buat¹⁴³, F. Bucci⁴⁹,
 P. Buchholz¹⁴², R.M. Buckingham¹¹⁹, A.G. Buckley⁵³, S.I. Buda^{26a},
 I.A. Budagov⁶⁴, F. Buehrer⁴⁸, L. Bugge¹¹⁸, M.K. Bugge¹¹⁸,
 O. Bulekov⁹⁷, A.C. Bundock⁷³, H. Burckhart³⁰, S. Burdin⁷³,
 B. Burghgrave¹⁰⁷, S. Burke¹³⁰, I. Burmeister⁴³, E. Busato³⁴,
 D. Büscher⁴⁸, V. Büscher⁸², P. Bussey⁵³, C.P. Buszello¹⁶⁷, B. Butler⁵⁷,
 J.M. Butler²², A.I. Butt³, C.M. Buttar⁵³, J.M. Butterworth⁷⁷, P. Butti¹⁰⁶,
 W. Buttinger²⁸, A. Buzatu⁵³, M. Byszewski¹⁰, S. Cabrera Urbán¹⁶⁸,
 D. Caforio^{20a,20b}, O. Cakir^{4a}, P. Calafiura¹⁵, A. Calandri¹³⁷,
 G. Calderini⁷⁹, P. Calfayan⁹⁹, R. Calkins¹⁰⁷, L.P. Caloba^{24a}, D. Calvet³⁴,
 S. Calvet³⁴, R. Camacho Toro⁴⁹, S. Camarda⁴², D. Cameron¹¹⁸,
 L.M. Caminada¹⁵, R. Caminal Armadans¹², S. Campana³⁰,
 M. Campanelli⁷⁷, A. Campoverde¹⁴⁹, V. Canale^{103a,103b}, A. Canepa^{160a},
 M. Cano Bret⁷⁵, J. Cantero⁸¹, R. Cantrill^{125a}, T. Cao⁴⁰,
 M.D.M. Capeans Garrido³⁰, I. Caprini^{26a}, M. Caprini^{26a}, M. Capua^{37a,37b},
 R. Caputo⁸², R. Cardarelli^{134a}, T. Carli³⁰, G. Carlino^{103a},
 L. Carminati^{90a,90b}, S. Caron¹⁰⁵, E. Carquin^{32a},
 G.D. Carrillo-Montoya^{146c}, J.R. Carter²⁸, J. Carvalho^{125a,125c},

D. Casadei ⁷⁷, M.P. Casado ¹², M. Casolino ¹², E. Castaneda-Miranda ^{146b},
 A. Castelli ¹⁰⁶, V. Castillo Gimenez ¹⁶⁸, N.F. Castro ^{125a}, P. Catastini ⁵⁷,
 A. Catinaccio ³⁰, J.R. Catmore ¹¹⁸, A. Cattai ³⁰, G. Cattani ^{134a,134b},
 J. Caudron ⁸², V. Cavaliere ¹⁶⁶, D. Cavalli ^{90a}, M. Cavalli-Sforza ¹²,
 V. Cavasinni ^{123a,123b}, F. Ceradini ^{135a,135b}, B.C. Cerio ⁴⁵, K. Cerny ¹²⁸,
 A.S. Cerqueira ^{24b}, A. Cerri ¹⁵⁰, L. Cerrito ⁷⁵, F. Cerutti ¹⁵, M. Cerv ³⁰,
 A. Cervelli ¹⁷, S.A. Cetin ^{19b}, A. Chafaq ^{136a}, D. Chakraborty ¹⁰⁷,
 I. Chalupkova ¹²⁸, S. Chance ¹¹⁶, P. Chang ¹⁶⁶, B. Chapleau ⁸⁶,
 J.D. Chapman ²⁸, D. Charfeddine ¹¹⁶, D.G. Charlton ¹⁸, C.C. Chau ¹⁵⁹,
 C.A. Chavez Barajas ¹⁵⁰, S. Cheatham ¹⁵³, A. Chegwidden ⁸⁹,
 S. Chekanov ⁶, S.V. Chekulaev ^{160a}, G.A. Chelkov ^{64,h},
 M.A. Chelstowska ⁸⁸, C. Chen ⁶³, H. Chen ²⁵, K. Chen ¹⁴⁹, L. Chen ^{33d,i},
 S. Chen ^{33c}, X. Chen ^{146c}, Y. Chen ⁶⁶, Y. Chen ³⁵, H.C. Cheng ⁸⁸,
 Y. Cheng ³¹, A. Cheplakov ⁶⁴, R. Cherkaoui El Moursli ^{136e},
 V. Chernyatin ^{25,*}, E. Cheu ⁷, L. Chevalier ¹³⁷, V. Chiarella ⁴⁷,
 G. Chiefari ^{103a,103b}, J.T. Childers ⁶, A. Chilingarov ⁷¹, G. Chiodini ^{72a},
 A.S. Chisholm ¹⁸, R.T. Chislett ⁷⁷, A. Chitan ^{26a}, M.V. Chizhov ⁶⁴,
 S. Chouridou ⁹, B.K.B. Chow ⁹⁹, D. Chromek-Burckhart ³⁰, M.L. Chu ¹⁵²,
 J. Chudoba ¹²⁶, J.J. Chwastowski ³⁹, L. Chytka ¹¹⁴, G. Ciapetti ^{133a,133b},
 A.K. Ciftci ^{4a}, R. Ciftci ^{4a}, D. Cinca ⁵³, V. Cindro ⁷⁴, A. Ciocio ¹⁵,
 P. Cirkovic ^{13b}, Z.H. Citron ¹⁷³, M. Citterio ^{90a}, M. Ciubancan ^{26a},
 A. Clark ⁴⁹, P.J. Clark ⁴⁶, R.N. Clarke ¹⁵, W. Cleland ¹²⁴, J.C. Clemens ⁸⁴,
 C. Clement ^{147a,147b}, Y. Coadou ⁸⁴, M. Cobal ^{165a,165c}, A. Coccaro ¹³⁹,
 J. Cochran ⁶³, L. Coffey ²³, J.G. Cogan ¹⁴⁴, J. Coggeshall ¹⁶⁶, B. Cole ³⁵,
 S. Cole ¹⁰⁷, A.P. Colijn ¹⁰⁶, J. Collot ⁵⁵, T. Colombo ^{58c}, G. Colon ⁸⁵,
 G. Compostella ¹⁰⁰, P. Conde Muiño ^{125a,125b}, E. Coniavitis ⁴⁸,
 M.C. Conidi ¹², S.H. Connell ^{146b}, I.A. Connelly ⁷⁶, S.M. Consonni ^{90a,90b},
 V. Consorti ⁴⁸, S. Constantinescu ^{26a}, C. Conta ^{120a,120b}, G. Conti ⁵⁷,
 F. Conventi ^{103a,j}, M. Cooke ¹⁵, B.D. Cooper ⁷⁷, A.M. Cooper-Sarkar ¹¹⁹,
 N.J. Cooper-Smith ⁷⁶, K. Copic ¹⁵, T. Cornelissen ¹⁷⁶, M. Corradi ^{20a},
 F. Corriveau ^{86,k}, A. Corso-Radu ¹⁶⁴, A. Cortes-Gonzalez ¹²,
 G. Cortiana ¹⁰⁰, G. Costa ^{90a}, M.J. Costa ¹⁶⁸, D. Costanzo ¹⁴⁰, D. Côté ⁸,
 G. Cottin ²⁸, G. Cowan ⁷⁶, B.E. Cox ⁸³, K. Cranmer ¹⁰⁹, G. Cree ²⁹,
 S. Crépe-Renaudin ⁵⁵, F. Crescioli ⁷⁹, W.A. Cribbs ^{147a,147b},
 M. Crispin Ortuzar ¹¹⁹, M. Cristinziani ²¹, V. Croft ¹⁰⁵, G. Crosetti ^{37a,37b},
 C.-M. Cuciuc ^{26a}, T. Cuhadar Donszelmann ¹⁴⁰, J. Cummings ¹⁷⁷,
 M. Curatolo ⁴⁷, C. Cuthbert ¹⁵¹, H. Czirr ¹⁴², P. Czodrowski ³,

Z. Czyczula¹⁷⁷, S. D’Auria⁵³, M. D’Onofrio⁷³,
M.J. Da Cunha Sargedas De Sousa^{125a,125b}, C. Da Via⁸³,
W. Dabrowski^{38a}, A. Dafinca¹¹⁹, T. Dai⁸⁸, O. Dale¹⁴, F. Dallaire⁹⁴,
C. Dallapiccola⁸⁵, M. Dam³⁶, A.C. Daniells¹⁸, M. Dano Hoffmann¹³⁷,
V. Dao⁴⁸, G. Darbo^{50a}, S. Darmora⁸, J. Dassoulas⁴², A. Dattagupta⁶⁰,
W. Davey²¹, C. David¹⁷⁰, T. Davidek¹²⁸, E. Davies^{119,d}, M. Davies¹⁵⁴,
O. Davignon⁷⁹, A.R. Davison⁷⁷, P. Davison⁷⁷, Y. Davygora^{58a},
E. Dawe¹⁴³, I. Dawson¹⁴⁰, R.K. Daya-Ishmukhametova⁸⁵, K. De⁸,
R. de Asmundis^{103a}, S. De Castro^{20a,20b}, S. De Cecco⁷⁹, N. De Groot¹⁰⁵,
P. de Jong¹⁰⁶, H. De la Torre⁸¹, F. De Lorenzi⁶³, L. De Nooij¹⁰⁶,
D. De Pedis^{133a}, A. De Salvo^{133a}, U. De Sanctis¹⁵⁰, A. De Santo¹⁵⁰,
J.B. De Vivie De Regie¹¹⁶, W.J. Dearnaley⁷¹, R. Debbé²⁵,
C. Debenedetti¹³⁸, B. Dechenaux⁵⁵, D.V. Dedovich⁶⁴, I. Deigaard¹⁰⁶,
J. Del Peso⁸¹, T. Del Prete^{123a,123b}, F. Deliot¹³⁷, C.M. Delitzsch⁴⁹,
M. Deliyergiyev⁷⁴, A. Dell’Acqua³⁰, L. Dell’Asta²²,
M. Dell’Orso^{123a,123b}, M. Della Pietra^{103a,j}, D. della Volpe⁴⁹,
M. Delmastro⁵, P.A. Delsart⁵⁵, C. Deluca¹⁰⁶, S. Demers¹⁷⁷,
M. Demichev⁶⁴, A. Demilly⁷⁹, S.P. Denisov¹²⁹, D. Derendarz³⁹,
J.E. Derkaoui^{136d}, F. Derue⁷⁹, P. Dervan⁷³, K. Desch²¹, C. Deterre⁴²,
P.O. Deviveiros¹⁰⁶, A. Dewhurst¹³⁰, S. Dhaliwal¹⁰⁶, A. Di Ciaccio^{134a,134b},
L. Di Ciaccio⁵, A. Di Domenico^{133a,133b}, C. Di Donato^{103a,103b},
A. Di Girolamo³⁰, B. Di Girolamo³⁰, A. Di Mattia¹⁵³,
B. Di Micco^{135a,135b}, R. Di Nardo⁴⁷, A. Di Simone⁴⁸, R. Di Sipio^{20a,20b},
D. Di Valentino²⁹, F.A. Dias⁴⁶, M.A. Diaz^{32a}, E.B. Diehl⁸⁸, J. Dietrich⁴²,
T.A. Dietzsch^{58a}, S. Diglio⁸⁴, A. Dimitrievska^{13a}, J. Dingfelder²¹,
C. Dionisi^{133a,133b}, P. Dita^{26a}, S. Dita^{26a}, F. Dittus³⁰, F. Djama⁸⁴,
T. Djobava^{51b}, J.I. Djuvsland^{58a}, M.A.B. do Vale^{24c},
A. Do Valle Wemans^{125a,125g}, D. Dobos³⁰, C. Doglioni⁴⁹, T. Doherty⁵³,
T. Dohmae¹⁵⁶, J. Dolejsi¹²⁸, Z. Dolezal¹²⁸, B.A. Dolgoshein^{97,*},
M. Donadelli^{24d}, S. Donati^{123a,123b}, P. Dondero^{120a,120b}, J. Donini³⁴,
J. Dopke¹³⁰, A. Doria^{103a}, M.T. Dova⁷⁰, A.T. Doyle⁵³, M. Dris¹⁰,
J. Dubbert⁸⁸, S. Dube¹⁵, E. Dubreuil³⁴, E. Duchovni¹⁷³, G. Duckeck⁹⁹,
O.A. Ducu^{26a}, D. Duda¹⁷⁶, A. Dudarev³⁰, F. Dudziak⁶³, L. Duflost¹¹⁶,
L. Duguid⁷⁶, M. Dührssen³⁰, M. Dunford^{58a}, H. Duran Yildiz^{4a},
M. Düren⁵², A. Durglishvili^{51b}, M. Dwuznik^{38a}, M. Dyndal^{38a}, J. Ebke⁹⁹,
W. Edson², N.C. Edwards⁴⁶, W. Ehrenfeld²¹, T. Eifert¹⁴⁴, G. Eigen¹⁴,
K. Einsweiler¹⁵, T. Ekelof¹⁶⁷, M. El Kacimi^{136c}, M. Ellert¹⁶⁷, S. Elles⁵,

F. Ellinghaus⁸², N. Ellis³⁰, J. Elmsheuser⁹⁹, M. Elsing³⁰,
 D. Emeliyanov¹³⁰, Y. Enari¹⁵⁶, O.C. Endner⁸², M. Endo¹¹⁷,
 R. Engelmann¹⁴⁹, J. Erdmann¹⁷⁷, A. Ereditato¹⁷, D. Eriksson^{147a},
 G. Ernis¹⁷⁶, J. Ernst², M. Ernst²⁵, J. Ernwein¹³⁷, D. Errede¹⁶⁶,
 S. Errede¹⁶⁶, E. Ertel⁸², M. Escalier¹¹⁶, H. Esch⁴³, C. Escobar¹²⁴,
 B. Esposito⁴⁷, A.I. Etienvre¹³⁷, E. Etzion¹⁵⁴, H. Evans⁶⁰, A. Ezhilov¹²²,
 L. Fabbri^{20a,20b}, G. Facini³¹, R.M. Fakhruddinov¹²⁹, S. Falciano^{133a},
 R.J. Falla⁷⁷, J. Faltova¹²⁸, Y. Fang^{33a}, M. Fanti^{90a,90b}, A. Farbin⁸,
 A. Farilla^{135a}, T. Farooque¹², S. Farrell¹⁵, S.M. Farrington¹⁷¹,
 P. Farthouat³⁰, F. Fassi^{136e}, P. Fassnacht³⁰, D. Fassouliotis⁹,
 A. Favareto^{50a,50b}, L. Fayard¹¹⁶, P. Federic^{145a}, O.L. Fedin^{122,l},
 W. Fedorko¹⁶⁹, M. Fehling-Kaschek⁴⁸, S. Feigl³⁰, L. Feligioni⁸⁴,
 C. Feng^{33d}, E.J. Feng⁶, H. Feng⁸⁸, A.B. Fenyuk¹²⁹, S. Fernandez Perez³⁰,
 S. Ferrag⁵³, J. Ferrando⁵³, A. Ferrari¹⁶⁷, P. Ferrari¹⁰⁶, R. Ferrari^{120a},
 D.E. Ferreira de Lima⁵³, A. Ferrer¹⁶⁸, D. Ferrere⁴⁹, C. Ferretti⁸⁸,
 A. Ferretto Parodi^{50a,50b}, M. Fiascaris³¹, F. Fiedler⁸², A. Filipčič⁷⁴,
 M. Filipuzzi⁴², F. Filthaut¹⁰⁵, M. Fincke-Keeler¹⁷⁰, K.D. Finelli¹⁵¹,
 M.C.N. Fiolhais^{125a,125c}, L. Fiorini¹⁶⁸, A. Firan⁴⁰, A. Fischer²,
 J. Fischer¹⁷⁶, W.C. Fisher⁸⁹, E.A. Fitzgerald²³, M. Flechl⁴⁸, I. Fleck¹⁴²,
 P. Fleischmann⁸⁸, S. Fleischmann¹⁷⁶, G.T. Fletcher¹⁴⁰, G. Fletcher⁷⁵,
 T. Flick¹⁷⁶, A. Floderus⁸⁰, L.R. Flores Castillo^{174,m},
 A.C. Florez Bustos^{160b}, M.J. Flowerdew¹⁰⁰, A. Formica¹³⁷, A. Forti⁸³,
 D. Fortin^{160a}, D. Fournier¹¹⁶, H. Fox⁷¹, S. Fracchia¹², P. Francavilla⁷⁹,
 M. Franchini^{20a,20b}, S. Franchino³⁰, D. Francis³⁰, L. Franconi¹¹⁸,
 M. Franklin⁵⁷, S. Franz⁶¹, M. Fraternali^{120a,120b}, S.T. French²⁸,
 C. Friedrich⁴², F. Friedrich⁴⁴, D. Froidevaux³⁰, J.A. Frost²⁸,
 C. Fukunaga¹⁵⁷, E. Fullana Torregrosa⁸², B.G. Fulsom¹⁴⁴, J. Fuster¹⁶⁸,
 C. Gabaldon⁵⁵, O. Gabizon¹⁷⁶, A. Gabrielli^{20a,20b}, A. Gabrielli^{133a,133b},
 S. Gadatsch¹⁰⁶, S. Gadomski⁴⁹, G. Gagliardi^{50a,50b}, P. Gagnon⁶⁰,
 C. Galea¹⁰⁵, B. Galhardo^{125a,125c}, E.J. Gallas¹¹⁹, V. Gallo¹⁷,
 B.J. Gallop¹³⁰, P. Gallus¹²⁷, G. Galster³⁶, K.K. Gan¹¹⁰, J. Gao^{33b,i},
 Y.S. Gao^{144,f}, F.M. Garay Walls⁴⁶, F. Garbersson¹⁷⁷, C. García¹⁶⁸,
 J.E. García Navarro¹⁶⁸, M. Garcia-Sciveres¹⁵, R.W. Gardner³¹,
 N. Garelli¹⁴⁴, V. Garonne³⁰, C. Gatti⁴⁷, G. Gaudio^{120a}, B. Gaur¹⁴²,
 L. Gauthier⁹⁴, P. Gauzzi^{133a,133b}, I.L. Gavrilenko⁹⁵, C. Gay¹⁶⁹,
 G. Gaycken²¹, E.N. Gazis¹⁰, P. Ge^{33d}, Z. Gece¹⁶⁹, C.N.P. Gee¹³⁰,
 D.A.A. Geerts¹⁰⁶, Ch. Geich-Gimbel²¹, K. Gellerstedt^{147a,147b},

C. Gemme^{50a}, A. Gemmell⁵³, M.H. Genest⁵⁵, S. Gentile^{133a,133b},
 M. George⁵⁴, S. George⁷⁶, D. Gerbaudo¹⁶⁴, A. Gershon¹⁵⁴,
 H. Ghazlane^{136b}, N. Ghodbane³⁴, B. Giacobbe^{20a}, S. Giagu^{133a,133b},
 V. Giangiobbe¹², P. Giannetti^{123a,123b}, F. Gianotti³⁰, B. Gibbard²⁵,
 S.M. Gibson⁷⁶, M. Gilchriese¹⁵, T.P.S. Gillam²⁸, D. Gillberg³⁰,
 G. Gilles³⁴, D.M. Gingrich^{3,e}, N. Giokaris⁹, M.P. Giordani^{165a,165c},
 R. Giordano^{103a,103b}, F.M. Giorgi^{20a}, F.M. Giorgi¹⁶, P.F. Giraud¹³⁷,
 D. Giugni^{90a}, C. Giuliani⁴⁸, M. Giulini^{58b}, B.K. Gjelsten¹¹⁸,
 S. Gkaitatzis¹⁵⁵, I. Gkialas¹⁵⁵, L.K. Gladilin⁹⁸, C. Glasman⁸¹,
 J. Glatzer³⁰, P.C.F. Glaysher⁴⁶, A. Glazov⁴², G.L. Glonti⁶⁴,
 M. Goblirsch-Kolb¹⁰⁰, J.R. Goddard⁷⁵, J. Godlewski³⁰, C. Goeringer⁸²,
 S. Goldfarb⁸⁸, T. Golling¹⁷⁷, D. Golubkov¹²⁹, A. Gomes^{125a,125b,125d},
 L.S. Gomez Fajardo⁴², R. Gonçalo^{125a},
 J. Goncalves Pinto Firmino Da Costa¹³⁷, L. Gonella²¹,
 S. González de la Hoz¹⁶⁸, G. Gonzalez Parra¹², S. Gonzalez-Sevilla⁴⁹,
 L. Goossens³⁰, P.A. Gorbounov⁹⁶, H.A. Gordon²⁵, I. Gorelov¹⁰⁴,
 B. Gorini³⁰, E. Gorini^{72a,72b}, A. Gorišek⁷⁴, E. Gornicki³⁹, A.T. Goshaw⁶,
 C. Gössling⁴³, M.I. Gostkin⁶⁴, M. Gouighri^{136a}, D. Goujdami^{136c},
 M.P. Goulette⁴⁹, A.G. Goussiou¹³⁹, C. Goy⁵, S. Gozpinar²³,
 H.M.X. Grabas¹³⁷, L. Graber⁵⁴, I. Grabowska-Bold^{38a},
 P. Grafström^{20a,20b}, K.-J. Grahm⁴², J. Gramling⁴⁹, E. Gramstad¹¹⁸,
 S. Grancagnolo¹⁶, V. Grassi¹⁴⁹, V. Gratchev¹²², H.M. Gray³⁰,
 E. Graziani^{135a}, O.G. Grebenyuk¹²², Z.D. Greenwood^{78,n},
 K. Gregersen⁷⁷, I.M. Gregor⁴², P. Grenier¹⁴⁴, J. Griffiths⁸,
 A.A. Grillo¹³⁸, K. Grimm⁷¹, S. Grinstein^{12,o}, Ph. Gris³⁴,
 Y.V. Grishkevich⁹⁸, J.-F. Grivaz¹¹⁶, J.P. Grohs⁴⁴, A. Grohsjean⁴²,
 E. Gross¹⁷³, J. Grosse-Knetter⁵⁴, G.C. Grossi^{134a,134b}, J. Groth-Jensen¹⁷³,
 Z.J. Grout¹⁵⁰, L. Guan^{33b}, J. Guenther¹²⁷, F. Guescini⁴⁹, D. Guest¹⁷⁷,
 O. Gueta¹⁵⁴, C. Guicheney³⁴, E. Guido^{50a,50b}, T. Guillemin¹¹⁶,
 S. Guindon², U. Gul⁵³, C. Gumpert⁴⁴, J. Guo³⁵, S. Gupta¹¹⁹,
 P. Gutierrez¹¹², N.G. Gutierrez Ortiz⁵³, C. Gutsche⁷⁷, N. Guttman¹⁵⁴,
 C. Guyot¹³⁷, C. Gwenlan¹¹⁹, C.B. Gwilliam⁷³, A. Haas¹⁰⁹, C. Haber¹⁵,
 H.K. Hadavand⁸, N. Haddad^{136e}, P. Haefner²¹, S. Hageböck²¹,
 M. Haguenaue¹¹⁶, Z. Hajduk³⁹, H. Hakobyan¹⁷⁸, M. Haleem⁴²,
 D. Hall¹¹⁹, G. Halladjian⁸⁹, K. Hamacher¹⁷⁶, P. Hamal¹¹⁴, K. Hamano¹⁷⁰,
 M. Hamer⁵⁴, A. Hamilton^{146a}, S. Hamilton¹⁶², G.N. Hamity^{146c},
 P.G. Hamnett⁴², L. Han^{33b}, K. Hanagaki¹¹⁷, K. Hanawa¹⁵⁶, M. Hance¹⁵,

P. Hanke^{58a}, R. Hanna¹³⁷, J.B. Hansen³⁶, J.D. Hansen³⁶, P.H. Hansen³⁶,
 K. Hara¹⁶¹, A.S. Hard¹⁷⁴, T. Harenberg¹⁷⁶, F. Hariri¹¹⁶, S. Harkusha⁹¹,
 D. Harper⁸⁸, R.D. Harrington⁴⁶, O.M. Harris¹³⁹, P.F. Harrison¹⁷¹,
 F. Hartjes¹⁰⁶, M. Hasegawa⁶⁶, S. Hasegawa¹⁰², Y. Hasegawa¹⁴¹,
 A. Hasib¹¹², S. Hassani¹³⁷, S. Haug¹⁷, M. Hauschild³⁰, R. Hauser⁸⁹,
 M. Havranek¹²⁶, C.M. Hawkes¹⁸, R.J. Hawkins³⁰, A.D. Hawkins⁸⁰,
 T. Hayashi¹⁶¹, D. Hayden⁸⁹, C.P. Hays¹¹⁹, H.S. Hayward⁷³,
 S.J. Haywood¹³⁰, S.J. Head¹⁸, T. Heck⁸², V. Hedberg⁸⁰, L. Heelan⁸,
 S. Heim¹²¹, T. Heim¹⁷⁶, B. Heinemann¹⁵, L. Heinrich¹⁰⁹, J. Hejbal¹²⁶,
 L. Helary²², C. Heller⁹⁹, M. Heller³⁰, S. Hellman^{147a,147b}, D. Hellmich²¹,
 C. Helsen³⁰, J. Henderson¹¹⁹, R.C.W. Henderson⁷¹, Y. Heng¹⁷⁴,
 C. Hengler⁴², A. Henrichs¹⁷⁷, A.M. Henriques Correia³⁰,
 S. Henrot-Versille¹¹⁶, C. Hensel⁵⁴, G.H. Herbert¹⁶,
 Y. Hernández Jiménez¹⁶⁸, R. Herrberg-Schubert¹⁶, G. Herten⁴⁸,
 R. Hertenberger⁹⁹, L. Hervas³⁰, G.G. Hesketh⁷⁷, N.P. Hessey¹⁰⁶,
 R. Hickling⁷⁵, E. Higón-Rodríguez¹⁶⁸, E. Hill¹⁷⁰, J.C. Hill²⁸,
 K.H. Hiller⁴², S. Hillert²¹, S.J. Hillier¹⁸, I. Hinchliffe¹⁵, E. Hines¹²¹,
 M. Hirose¹⁵⁸, D. Hirschbuehl¹⁷⁶, J. Hobbs¹⁴⁹, N. Hod¹⁰⁶,
 M.C. Hodgkinson¹⁴⁰, P. Hodgson¹⁴⁰, A. Hoecker³⁰,
 M.R. Hoferkamp¹⁰⁴, F. Hoenig⁹⁹, J. Hoffman⁴⁰, D. Hoffmann⁸⁴,
 M. Hohlfeld⁸², T.R. Holmes¹⁵, T.M. Hong¹²¹,
 L. Hooft van Huysduynen¹⁰⁹, W.H. Hopkins¹¹⁵, Y. Horii¹⁰²,
 J.-Y. Hostachy⁵⁵, S. Hou¹⁵², A. Hoummada^{136a}, J. Howard¹¹⁹,
 J. Howarth⁴², M. Hrabovsky¹¹⁴, I. Hristova¹⁶, J. Hrivnac¹¹⁶,
 T. Hryn'ova⁵, C. Hsu^{146c}, P.J. Hsu⁸², S.-C. Hsu¹³⁹, D. Hu³⁵, X. Hu⁸⁸,
 Y. Huang⁴², Z. Hubacek³⁰, F. Hubaut⁸⁴, F. Huegging²¹, T.B. Huffman¹¹⁹,
 E.W. Hughes³⁵, G. Hughes⁷¹, M. Huhtinen³⁰, T.A. Hülsing⁸²,
 M. Hurwitz¹⁵, N. Huseynov^{64,b}, J. Huston⁸⁹, J. Huth⁵⁷, G. Iacobucci⁴⁹,
 G. Iakovidis¹⁰, I. Ibragimov¹⁴², L. Iconomidou-Fayard¹¹⁶, E. Ideal¹⁷⁷,
 P. Iengo^{103a}, O. Igonkina¹⁰⁶, T. Iizawa¹⁷², Y. Ikegami⁶⁵, K. Ikematsu¹⁴²,
 M. Ikeno⁶⁵, Y. Ilchenko^{31,p}, D. Iliadis¹⁵⁵, N. Ilic¹⁵⁹, Y. Inamaru⁶⁶,
 T. Ince¹⁰⁰, P. Ioannou⁹, M. Iodice^{135a}, K. Iordanidou⁹, V. Ippolito⁵⁷,
 A. Irls Quiles¹⁶⁸, C. Isaksson¹⁶⁷, M. Ishino⁶⁷, M. Ishitsuka¹⁵⁸,
 R. Ishmukhametov¹¹⁰, C. Issever¹¹⁹, S. Istin^{19a}, J.M. Iturbe Ponce⁸³,
 R. Iuppa^{134a,134b}, J. Ivarsson⁸⁰, W. Iwanski³⁹, H. Iwasaki⁶⁵, J.M. Izen⁴¹,
 V. Izzo^{103a}, B. Jackson¹²¹, M. Jackson⁷³, P. Jackson¹, M.R. Jaekel³⁰,
 V. Jain², K. Jakobs⁴⁸, S. Jakobsen³⁰, T. Jakoubek¹²⁶, J. Jakubek¹²⁷,

D.O. Jamin ¹⁵², D.K. Jana ⁷⁸, E. Jansen ⁷⁷, H. Jansen ³⁰, J. Janssen ²¹,
 M. Janus ¹⁷¹, G. Jarlskog ⁸⁰, N. Javadov ^{64,b}, T. Javůrek ⁴⁸, L. Jeanty ¹⁵,
 J. Jejelava ^{51a,q}, G.-Y. Jeng ¹⁵¹, D. Jennens ⁸⁷, P. Jenni ^{48,r}, J. Jentsch ⁴³,
 C. Jeske ¹⁷¹, S. Jézéquel ⁵, H. Ji ¹⁷⁴, J. Jia ¹⁴⁹, Y. Jiang ^{33b},
 M. Jimenez Belenguer ⁴², S. Jin ^{33a}, A. Jinaru ^{26a}, O. Jinnouchi ¹⁵⁸,
 M.D. Joergensen ³⁶, K.E. Johansson ^{147a,147b}, P. Johansson ¹⁴⁰,
 K.A. Johns ⁷, K. Jon-And ^{147a,147b}, G. Jones ¹⁷¹, R.W.L. Jones ⁷¹,
 T.J. Jones ⁷³, J. Jongmanns ^{58a}, P.M. Jorge ^{125a,125b}, K.D. Joshi ⁸³,
 J. Jovicevic ¹⁴⁸, X. Ju ¹⁷⁴, C.A. Jung ⁴³, R.M. Jungst ³⁰, P. Jussel ⁶¹,
 A. Juste Rozas ^{12,o}, M. Kaci ¹⁶⁸, A. Kaczmarska ³⁹, M. Kado ¹¹⁶,
 H. Kagan ¹¹⁰, M. Kagan ¹⁴⁴, E. Kajomovitz ⁴⁵, C.W. Kalderon ¹¹⁹,
 S. Kama ⁴⁰, A. Kamenshchikov ¹²⁹, N. Kanaya ¹⁵⁶, M. Kaneda ³⁰,
 S. Kaneti ²⁸, V.A. Kantserov ⁹⁷, J. Kanzaki ⁶⁵, B. Kaplan ¹⁰⁹, A. Kapliy ³¹,
 D. Kar ⁵³, K. Karakostas ¹⁰, N. Karastathis ¹⁰, M.J. Kareem ⁵⁴,
 M. Karnevskiy ⁸², S.N. Karpov ⁶⁴, Z.M. Karpova ⁶⁴, K. Karthik ¹⁰⁹,
 V. Kartvelishvili ⁷¹, A.N. Karyukhin ¹²⁹, L. Kashif ¹⁷⁴, G. Kasieczka ^{58b},
 R.D. Kass ¹¹⁰, A. Kastanas ¹⁴, Y. Kataoka ¹⁵⁶, A. Katre ⁴⁹, J. Katzy ⁴²,
 V. Kaushik ⁷, K. Kawagoe ⁶⁹, T. Kawamoto ¹⁵⁶, G. Kawamura ⁵⁴,
 S. Kazama ¹⁵⁶, V.F. Kazanin ¹⁰⁸, M.Y. Kazarinov ⁶⁴, R. Keeler ¹⁷⁰,
 R. Kehoe ⁴⁰, M. Keil ⁵⁴, J.S. Keller ⁴², J.J. Kempster ⁷⁶, H. Keoshkerian ⁵,
 O. Kepka ¹²⁶, B.P. Kerševan ⁷⁴, S. Kersten ¹⁷⁶, K. Kessoku ¹⁵⁶, J. Keung ¹⁵⁹,
 F. Khalil-zada ¹¹, H. Khandanyan ^{147a,147b}, A. Khanov ¹¹³, A. Khodinov ⁹⁷,
 A. Khomich ^{58a}, T.J. Khoo ²⁸, G. Khoriauli ²¹, A. Khoroshilov ¹⁷⁶,
 V. Khovanskiy ⁹⁶, E. Khramov ⁶⁴, J. Khubua ^{51b}, H.Y. Kim ⁸,
 H. Kim ^{147a,147b}, S.H. Kim ¹⁶¹, N. Kimura ¹⁵⁵, O. Kind ¹⁶, B.T. King ⁷³,
 M. King ¹⁶⁸, R.S.B. King ¹¹⁹, S.B. King ¹⁶⁹, J. Kirk ¹³⁰, A.E. Kiryunin ¹⁰⁰,
 T. Kishimoto ⁶⁶, D. Kisielewska ^{38a}, F. Kiss ⁴⁸, T. Kittelmann ¹²⁴,
 K. Kiuchi ¹⁶¹, E. Kladiva ^{145b}, M. Klein ⁷³, U. Klein ⁷³, K. Kleinknecht ⁸²,
 P. Klimek ^{147a,147b}, A. Klimentov ²⁵, R. Klingenberg ⁴³, J.A. Klinger ⁸³,
 T. Klioutchnikova ³⁰, P.F. Klok ¹⁰⁵, E.-E. Kluge ^{58a}, P. Kluit ¹⁰⁶, S. Kluth ¹⁰⁰,
 E. Kneringer ⁶¹, E.B.F.G. Knoops ⁸⁴, A. Knue ⁵³, D. Kobayashi ¹⁵⁸,
 T. Kobayashi ¹⁵⁶, M. Kobel ⁴⁴, M. Kocian ¹⁴⁴, P. Kodys ¹²⁸, P. Koevesarki ²¹,
 T. Koffas ²⁹, E. Koffeman ¹⁰⁶, L.A. Kogan ¹¹⁹, S. Kohlmann ¹⁷⁶,
 Z. Kohout ¹²⁷, T. Kohriki ⁶⁵, T. Koi ¹⁴⁴, H. Kolanoski ¹⁶, I. Koletsou ⁵,
 J. Koll ⁸⁹, A.A. Komar ^{95,*}, Y. Komori ¹⁵⁶, T. Kondo ⁶⁵, N. Kondrashova ⁴²,
 K. Köneke ⁴⁸, A.C. König ¹⁰⁵, S. König ⁸², T. Kono ^{65,s}, R. Konoplich ^{109,t},
 N. Konstantinidis ⁷⁷, R. Kopeliansky ¹⁵³, S. Koperny ^{38a}, L. Köpke ⁸²,

A.K. Kopp⁴⁸, K. Korcyl³⁹, K. Kordas¹⁵⁵, A. Korn⁷⁷, A.A. Korol^{108,c},
 I. Korolkov¹², E.V. Korolkova¹⁴⁰, V.A. Korotkov¹²⁹, O. Kortner¹⁰⁰,
 S. Kortner¹⁰⁰, V.V. Kostyukhin²¹, V.M. Kotov⁶⁴, A. Kotwal⁴⁵,
 C. Kourkoumelis⁹, V. Kouskoura¹⁵⁵, A. Koutsman^{160a},
 R. Kowalewski¹⁷⁰, T.Z. Kowalski^{38a}, W. Kozanecki¹³⁷, A.S. Kozhin¹²⁹,
 V. Kral¹²⁷, V.A. Kramarenko⁹⁸, G. Kramberger⁷⁴, D. Krasnoperov⁹⁷,
 M.W. Krasny⁷⁹, A. Krasznahorkay³⁰, J.K. Kraus²¹, A. Kravchenko²⁵,
 S. Kreiss¹⁰⁹, M. Kretz^{58c}, J. Kretzschmar⁷³, K. Kreuzfeldt⁵²,
 P. Krieger¹⁵⁹, K. Kroeninger⁵⁴, H. Kroha¹⁰⁰, J. Kroll¹²¹, J. Kroseberg²¹,
 J. Krstic^{13a}, U. Kruchonak⁶⁴, H. Krüger²¹, T. Kruker¹⁷, N. Krumnack⁶³,
 Z.V. Krumshteyn⁶⁴, A. Kruse¹⁷⁴, M.C. Kruse⁴⁵, M. Kruskal²²,
 T. Kubota⁸⁷, H. Kucuk⁷⁷, S. Kudah^{4a}, S. Kuehn⁴⁸, A. Kugel^{58c},
 A. Kuhl¹³⁸, T. Kuhl⁴², V. Kukhtin⁶⁴, Y. Kulchitsky⁹¹, S. Kuleshov^{32b},
 M. Kuna^{133a,133b}, J. Kunkle¹²¹, A. Kupco¹²⁶, H. Kurashige⁶⁶,
 Y.A. Kurochkin⁹¹, R. Kurumida⁶⁶, V. Kus¹²⁶, E.S. Kuwertz¹⁴⁸,
 M. Kuze¹⁵⁸, J. Kvita¹¹⁴, A. La Rosa⁴⁹, L. La Rotonda^{37a,37b},
 C. Lacasta¹⁶⁸, F. Lacava^{133a,133b}, J. Lacey²⁹, H. Lacker¹⁶, D. Lacour⁷⁹,
 V.R. Lacuesta¹⁶⁸, E. Ladygin⁶⁴, R. Lafaye⁵, B. Laforge⁷⁹, T. Lagouri¹⁷⁷,
 S. Lai⁴⁸, H. Laier^{58a}, L. Lambourne⁷⁷, S. Lammers⁶⁰, C.L. Lampen⁷,
 W. Lampl⁷, E. Lançon¹³⁷, U. Landgraf⁴⁸, M.P.J. Landon⁷⁵, V.S. Lang^{58a},
 A.J. Lankford¹⁶⁴, F. Lanni²⁵, K. Lantzsch³⁰, S. Laplace⁷⁹, C. Lapoire²¹,
 J.F. Laporte¹³⁷, T. Lari^{90a}, F. Lasagni Manghi^{20a,20b}, M. Lassnig³⁰,
 P. Laurelli⁴⁷, W. Lavrijsen¹⁵, A.T. Law¹³⁸, P. Laycock⁷³, O. Le Dortz⁷⁹,
 E. Le Guirriec⁸⁴, E. Le Menedeu¹², T. LeCompte⁶, F. Ledroit-Guillon⁵⁵,
 C.A. Lee¹⁵², H. Lee¹⁰⁶, J.S.H. Lee¹¹⁷, S.C. Lee¹⁵², L. Lee¹,
 G. Lefebvre⁷⁹, M. Lefebvre¹⁷⁰, F. Legger⁹⁹, C. Leggett¹⁵, A. Lehan⁷³,
 M. Lehmacher²¹, G. Lehmann Miotto³⁰, X. Lei⁷, W.A. Leight²⁹,
 A. Leisos¹⁵⁵, A.G. Leister¹⁷⁷, M.A.L. Leite^{24d}, R. Leitner¹²⁸,
 D. Lellouch¹⁷³, B. Lemmer⁵⁴, K.J.C. Leney⁷⁷, T. Lenz²¹, G. Lenzen¹⁷⁶,
 B. Lenzi³⁰, R. Leone⁷, S. Leone^{123a,123b}, C. Leonidopoulos⁴⁶,
 S. Leontsinis¹⁰, C. Leroy⁹⁴, C.G. Lester²⁸, C.M. Lester¹²¹,
 M. Levchenko¹²², J. Levêque⁵, D. Levin⁸⁸, L.J. Levinson¹⁷³, M. Levy¹⁸,
 A. Lewis¹¹⁹, G.H. Lewis¹⁰⁹, A.M. Leyko²¹, M. Leyton⁴¹, B. Li^{33b,u},
 B. Li⁸⁴, H. Li¹⁴⁹, H.L. Li³¹, L. Li⁴⁵, L. Li^{33e}, S. Li⁴⁵, Y. Li^{33c,v},
 Z. Liang¹³⁸, H. Liao³⁴, B. Liberti^{134a}, P. Lichard³⁰, K. Lie¹⁶⁶, J. Liebal²¹,
 W. Liebig¹⁴, C. Limbach²¹, A. Limosani⁸⁷, S.C. Lin^{152,w}, T.H. Lin⁸²,
 F. Linde¹⁰⁶, B.E. Lindquist¹⁴⁹, J.T. Linnemann⁸⁹, E. Lipeles¹²¹,

A. Lipniacka¹⁴, M. Lisovyi⁴², T.M. Liss¹⁶⁶, D. Lissauer²⁵, A. Lister¹⁶⁹,
 A.M. Litke¹³⁸, B. Liu¹⁵², D. Liu¹⁵², J.B. Liu^{33b}, K. Liu^{33b,x}, L. Liu⁸⁸,
 M. Liu⁴⁵, M. Liu^{33b}, Y. Liu^{33b}, M. Livan^{120a,120b}, S.S.A. Livermore¹¹⁹,
 A. Lleres⁵⁵, J. Llorente Merino⁸¹, S.L. Lloyd⁷⁵, F. Lo Sterzo¹⁵²,
 E. Lobodzinska⁴², P. Loch⁷, W.S. Lockman¹³⁸, F.K. Loebinger⁸³,
 A.E. Loevschall-Jensen³⁶, A. Loginov¹⁷⁷, T. Lohse¹⁶, K. Lohwasser⁴²,
 M. Lokajicek¹²⁶, V.P. Lombardo⁵, B.A. Long²², J.D. Long⁸⁸,
 R.E. Long⁷¹, L. Lopes^{125a}, D. Lopez Mateos⁵⁷, B. Lopez Paredes¹⁴⁰,
 I. Lopez Paz¹², J. Lorenz⁹⁹, N. Lorenzo Martinez⁶⁰, M. Losada¹⁶³,
 P. Loscutoff¹⁵, X. Lou⁴¹, A. Lounis¹¹⁶, J. Love⁶, P.A. Love⁷¹,
 A.J. Lowe^{144,f}, F. Lu^{33a}, N. Lu⁸⁸, H.J. Lubatti¹³⁹, C. Luci^{133a,133b},
 A. Lucotte⁵⁵, F. Luehring⁶⁰, W. Lukas⁶¹, L. Luminari^{133a},
 O. Lundberg^{147a,147b}, B. Lund-Jensen¹⁴⁸, M. Lungwitz⁸², D. Lynn²⁵,
 R. Lysak¹²⁶, E. Lytken⁸⁰, H. Ma²⁵, L.L. Ma^{33d}, G. Maccarrone⁴⁷,
 A. Macchiolo¹⁰⁰, J. Machado Miguens^{125a,125b}, D. Macina³⁰,
 D. Madaffari⁸⁴, R. Madar⁴⁸, H.J. Maddocks⁷¹, W.F. Mader⁴⁴,
 A. Madsen¹⁶⁷, M. Maeno⁸, T. Maeno²⁵, A. Maevskiy⁹⁸, E. Magradze⁵⁴,
 K. Mahboubi⁴⁸, J. Mahlstedt¹⁰⁶, S. Mahmoud⁷³, C. Maiani¹³⁷,
 C. Maidantchik^{24a}, A.A. Maier¹⁰⁰, A. Maio^{125a,125b,125d}, S. Majewski¹¹⁵,
 Y. Makida⁶⁵, N. Makovec¹¹⁶, P. Mal^{137,y}, B. Malaescu⁷⁹, Pa. Malecki³⁹,
 V.P. Maleev¹²², F. Malek⁵⁵, U. Mallik⁶², D. Malon⁶, C. Malone¹⁴⁴,
 S. Maltezos¹⁰, V.M. Malyshev¹⁰⁸, S. Malyukov³⁰, J. Mamuzic^{13b},
 B. Mandelli³⁰, L. Mandelli^{90a}, I. Mandić⁷⁴, R. Mandrysch⁶²,
 J. Maneira^{125a,125b}, A. Manfredini¹⁰⁰, L. Manhaes de Andrade Filho^{24b},
 J.A. Manjarres Ramos^{160b}, A. Mann⁹⁹, P.M. Manning¹³⁸,
 A. Manousakis-Katsikakis⁹, B. Mansoulie¹³⁷, R. Mantifel⁸⁶,
 L. Mapelli³⁰, L. March^{146c}, J.F. Marchand²⁹, G. Marchiori⁷⁹,
 M. Marcisovsky¹²⁶, C.P. Marino¹⁷⁰, M. Marjanovic^{13a}, C.N. Marques^{125a},
 F. Marroquim^{24a}, S.P. Marsden⁸³, Z. Marshall¹⁵, L.F. Marti¹⁷,
 S. Marti-Garcia¹⁶⁸, B. Martin³⁰, B. Martin⁸⁹, T.A. Martin¹⁷¹,
 V.J. Martin⁴⁶, B. Martin dit Latour¹⁴, H. Martinez¹³⁷, M. Martinez^{12,o},
 S. Martin-Haugh¹³⁰, A.C. Martyniuk⁷⁷, M. Marx¹³⁹, F. Marzano^{133a},
 A. Marzin³⁰, L. Masetti⁸², T. Mashimo¹⁵⁶, R. Mashinistov⁹⁵, J. Masik⁸³,
 A.L. Maslennikov^{108,c}, I. Massa^{20a,20b}, L. Massa^{20a,20b}, N. Massol⁵,
 P. Mastrandrea¹⁴⁹, A. Mastroberardino^{37a,37b}, T. Masubuchi¹⁵⁶,
 P. Mättig¹⁷⁶, J. Mattmann⁸², J. Maurer^{26a}, S.J. Maxfield⁷³,
 D.A. Maximov^{108,c}, R. Mazini¹⁵², L. Mazzaferro^{134a,134b},

G. Mc Goldrick¹⁵⁹, S.P. Mc Kee⁸⁸, A. McCarn⁸⁸, R.L. McCarthy¹⁴⁹,
 T.G. McCarthy²⁹, N.A. McCubbin¹³⁰, K.W. McFarlane^{56,*},
 J.A. Mcfayden⁷⁷, G. Mchedlidze⁵⁴, S.J. McMahon¹³⁰,
 R.A. McPherson^{170,k}, J. Mechnich¹⁰⁶, M. Medinnis⁴², S. Meehan³¹,
 S. Mehlhase⁹⁹, A. Mehta⁷³, K. Meier^{58a}, C. Meineck⁹⁹, B. Meirose⁸⁰,
 C. Melachrinou³¹, B.R. Mellado Garcia^{146c}, F. Meloni¹⁷,
 A. Mengarelli^{20a,20b}, S. Menke¹⁰⁰, E. Meoni¹⁶², K.M. Mercurio⁵⁷,
 S. Mergelmeyer²¹, N. Meric¹³⁷, P. Mermod⁴⁹, L. Merola^{103a,103b},
 C. Meroni^{90a}, F.S. Merritt³¹, H. Merritt¹¹⁰, A. Messina^{30,z}, J. Metcalfe²⁵,
 A.S. Mete¹⁶⁴, C. Meyer⁸², C. Meyer¹²¹, J-P. Meyer¹³⁷, J. Meyer³⁰,
 R.P. Middleton¹³⁰, S. Migas⁷³, L. Mijović²¹, G. Mikenberg¹⁷³,
 M. Mikestikova¹²⁶, M. Mikuž⁷⁴, A. Milic³⁰, D.W. Miller³¹, C. Mills⁴⁶,
 A. Milov¹⁷³, D.A. Milstead^{147a,147b}, D. Milstein¹⁷³, A.A. Minaenko¹²⁹,
 Y. Minami¹⁵⁶, I.A. Minashvili⁶⁴, A.I. Mincer¹⁰⁹, B. Mindur^{38a},
 M. Mineev⁶⁴, Y. Ming¹⁷⁴, L.M. Mir¹², G. Mirabelli^{133a}, T. Mitani¹⁷²,
 J. Mitrevski⁹⁹, V.A. Mitsou¹⁶⁸, S. Mitsui⁶⁵, A. Miucci⁴⁹,
 P.S. Miyagawa¹⁴⁰, J.U. Mjörnmark⁸⁰, T. Moa^{147a,147b}, K. Mochizuki⁸⁴,
 S. Mohapatra³⁵, W. Mohr⁴⁸, S. Molander^{147a,147b}, R. Moles-Valls¹⁶⁸,
 K. Mönig⁴², C. Monini⁵⁵, J. Monk³⁶, E. Monnier⁸⁴,
 J. Montejo Berlingen¹², F. Monticelli⁷⁰, S. Monzani^{133a,133b},
 R.W. Moore³, N. Morange⁶², D. Moreno⁸², M. Moreno Llácer⁵⁴,
 P. Morettini^{50a}, M. Morgenstern⁴⁴, M. Morii⁵⁷, S. Moritz⁸²,
 A.K. Morley¹⁴⁸, G. Mornacchi³⁰, J.D. Morris⁷⁵, L. Morvaj¹⁰²,
 H.G. Moser¹⁰⁰, M. Mosidze^{51b}, J. Moss¹¹⁰, K. Motohashi¹⁵⁸,
 R. Mount¹⁴⁴, E. Mountricha²⁵, S.V. Mouraviev^{95,*}, E.J.W. Moyses⁸⁵,
 S. Muanza⁸⁴, R.D. Mudd¹⁸, F. Mueller^{58a}, J. Mueller¹²⁴, K. Mueller²¹,
 T. Mueller²⁸, T. Mueller⁸², D. Muenstermann⁴⁹, Y. Munwes¹⁵⁴,
 J.A. Murillo Quijada¹⁸, W.J. Murray^{171,130}, H. Musheghyan⁵⁴,
 E. Musto¹⁵³, A.G. Myagkov^{129,aa}, M. Myska¹²⁷, O. Nackenhurst⁵⁴,
 J. Nadal⁵⁴, K. Nagai⁶¹, R. Nagai¹⁵⁸, Y. Nagai⁸⁴, K. Nagano⁶⁵,
 A. Nagarkar¹¹⁰, Y. Nagasaka⁵⁹, M. Nagel¹⁰⁰, A.M. Nairz³⁰,
 Y. Nakahama³⁰, K. Nakamura⁶⁵, T. Nakamura¹⁵⁶, I. Nakano¹¹¹,
 H. Namasivayam⁴¹, G. Nanava²¹, R. Narayan^{58b}, T. Nattermann²¹,
 T. Naumann⁴², G. Navarro¹⁶³, R. Nayyar⁷, H.A. Neal⁸⁸,
 P.Yu. Nechaeva⁹⁵, T.J. Neep⁸³, P.D. Nef¹⁴⁴, A. Negri^{120a,120b}, G. Negri³⁰,
 M. Negrini^{20a}, S. Nektarijevic⁴⁹, C. Nellist¹¹⁶, A. Nelson¹⁶⁴,
 T.K. Nelson¹⁴⁴, S. Nemecek¹²⁶, P. Nemethy¹⁰⁹, A.A. Nepomuceno^{24a},

M. Nessi ^{30,ab}, M.S. Neubauer ¹⁶⁶, M. Neumann ¹⁷⁶, R.M. Neves ¹⁰⁹,
 P. Nevski ²⁵, P.R. Newman ¹⁸, D.H. Nguyen ⁶, R.B. Nickerson ¹¹⁹,
 R. Nicolaidou ¹³⁷, B. Nicquevert ³⁰, J. Nielsen ¹³⁸, N. Nikiforou ³⁵,
 A. Nikiforov ¹⁶, V. Nikolaenko ^{129,aa}, I. Nikolic-Audit ⁷⁹, K. Nikolics ⁴⁹,
 K. Nikolopoulos ¹⁸, P. Nilsson ⁸, Y. Ninomiya ¹⁵⁶, A. Nisati ^{133a},
 R. Nisius ¹⁰⁰, T. Nobe ¹⁵⁸, L. Nodulman ⁶, M. Nomachi ¹¹⁷, I. Nomidis ²⁹,
 S. Norberg ¹¹², M. Nordberg ³⁰, O. Novgorodova ⁴⁴, S. Nowak ¹⁰⁰,
 M. Nozaki ⁶⁵, L. Nozka ¹¹⁴, K. Ntekas ¹⁰, G. Nunes Hanninger ⁸⁷,
 T. Nunnemann ⁹⁹, E. Nurse ⁷⁷, F. Nuti ⁸⁷, B.J. O'Brien ⁴⁶, F. O'grady ⁷,
 D.C. O'Neil ¹⁴³, V. O'Shea ⁵³, F.G. Oakham ^{29,e}, H. Oberlack ¹⁰⁰,
 T. Obermann ²¹, J. Ocariz ⁷⁹, A. Ochi ⁶⁶, I. Ochoa ⁷⁷, S. Oda ⁶⁹, S. Odaka ⁶⁵,
 H. Ogren ⁶⁰, A. Oh ⁸³, S.H. Oh ⁴⁵, C.C. Ohm ¹⁵, H. Ohman ¹⁶⁷,
 W. Okamura ¹¹⁷, H. Okawa ²⁵, Y. Okumura ³¹, T. Okuyama ¹⁵⁶,
 A. Olariu ^{26a}, A.G. Olchevski ⁶⁴, S.A. Olivares Pino ⁴⁶,
 D. Oliveira Damazio ²⁵, E. Oliver Garcia ¹⁶⁸, A. Olszewski ³⁹,
 J. Olszowska ³⁹, A. Onofre ^{125a,125e}, P.U.E. Onyisi ^{31,p}, C.J. Oram ^{160a},
 M.J. Oreglia ³¹, Y. Oren ¹⁵⁴, D. Orestano ^{135a,135b}, N. Orlando ^{72a,72b},
 C. Oropeza Barrera ⁵³, R.S. Orr ¹⁵⁹, B. Osculati ^{50a,50b}, R. Ospanov ¹²¹,
 G. Otero y Garzon ²⁷, H. Otono ⁶⁹, M. Ouchrif ^{136d}, E.A. Ouellette ¹⁷⁰,
 F. Ould-Saada ¹¹⁸, A. Ouraou ¹³⁷, K.P. Oussoren ¹⁰⁶, Q. Ouyang ^{33a},
 A. Ovcharova ¹⁵, M. Owen ⁸³, V.E. Ozcan ^{19a}, N. Ozturk ⁸, K. Pachal ¹¹⁹,
 A. Pacheco Pages ¹², C. Padilla Aranda ¹², M. Pagáčová ⁴⁸,
 S. Pagan Griso ¹⁵, E. Paganis ¹⁴⁰, C. Pahl ¹⁰⁰, F. Paige ²⁵, P. Pais ⁸⁵,
 K. Pajchel ¹¹⁸, G. Palacino ^{160b}, S. Palestini ³⁰, M. Palka ^{38b}, D. Pallin ³⁴,
 A. Palma ^{125a,125b}, J.D. Palmer ¹⁸, Y.B. Pan ¹⁷⁴, E. Panagiotopoulou ¹⁰,
 J.G. Panduro Vazquez ⁷⁶, P. Pani ¹⁰⁶, N. Panikashvili ⁸⁸, S. Panitkin ²⁵,
 D. Pantea ^{26a}, L. Paolozzi ^{134a,134b}, Th.D. Papadopoulou ¹⁰,
 K. Papageorgiou ¹⁵⁵, A. Paramonov ⁶, D. Paredes Hernandez ¹⁵⁵,
 M.A. Parker ²⁸, F. Parodi ^{50a,50b}, J.A. Parsons ³⁵, U. Parzefall ⁴⁸,
 E. Pasqualucci ^{133a}, S. Passaggio ^{50a}, A. Passeri ^{135a}, F. Pastore ^{135a,135b,*},
 Fr. Pastore ⁷⁶, G. Pásztor ²⁹, S. Pataria ¹⁷⁶, N.D. Patel ¹⁵¹, J.R. Pater ⁸³,
 S. Patricelli ^{103a,103b}, T. Pauly ³⁰, J. Pearce ¹⁷⁰, L.E. Pedersen ³⁶,
 M. Pedersen ¹¹⁸, S. Pedraza Lopez ¹⁶⁸, R. Pedro ^{125a,125b},
 S.V. Peleganchuk ¹⁰⁸, D. Pelikan ¹⁶⁷, H. Peng ^{33b}, B. Penning ³¹,
 J. Penwell ⁶⁰, D.V. Perepelitsa ²⁵, E. Perez Codina ^{160a},
 M.T. Pérez García-Estañ ¹⁶⁸, V. Perez Reale ³⁵, L. Perini ^{90a,90b},
 H. Pernegger ³⁰, S. Perrella ^{103a,103b}, R. Perrino ^{72a}, R. Peschke ⁴²,

V.D. Peshekhonov⁶⁴, K. Peters³⁰, R.F.Y. Peters⁸³, B.A. Petersen³⁰,
 T.C. Petersen³⁶, E. Petit⁴², A. Petridis^{147a,147b}, C. Petridou¹⁵⁵,
 E. Petrolu^{133a}, F. Petrucci^{135a,135b}, N.E. Pettersson¹⁵⁸, R. Pezoa^{32b},
 P.W. Phillips¹³⁰, G. Piacquadio¹⁴⁴, E. Pianori¹⁷¹, A. Picazio⁴⁹,
 E. Piccaro⁷⁵, M. Piccinini^{20a,20b}, R. Piegai²⁷, D.T. Pignotti¹¹⁰,
 J.E. Pilcher³¹, A.D. Pilkington⁷⁷, J. Pina^{125a,125b,125d},
 M. Pinamonti^{165a,165c,ac}, A. Pinder¹¹⁹, J.L. Pinfold³, A. Pingel³⁶,
 B. Pinto^{125a}, S. Pires⁷⁹, M. Pitt¹⁷³, C. Pizio^{90a,90b}, L. Plazak^{145a},
 M.-A. Pleier²⁵, V. Pleskot¹²⁸, E. Plotnikova⁶⁴, P. Plucinski^{147a,147b},
 S. Poddar^{58a}, F. Podlyski³⁴, R. Poettgen⁸², L. Poggioli¹¹⁶, D. Pohl²¹,
 M. Pohl⁴⁹, G. Polesello^{120a}, A. Policicchio^{37a,37b}, R. Polifka¹⁵⁹,
 A. Polini^{20a}, C.S. Pollard⁴⁵, V. Polychronakos²⁵, K. Pommès³⁰,
 L. Pontecorvo^{133a}, B.G. Pope⁸⁹, G.A. Popeneciu^{26b}, D.S. Popovic^{13a},
 A. Poppleton³⁰, X. Portell Bueso¹², S. Pospisil¹²⁷, K. Potamianos¹⁵,
 I.N. Potrap⁶⁴, C.J. Potter¹⁵⁰, C.T. Potter¹¹⁵, G. Poulard³⁰, J. Poveda⁶⁰,
 V. Pozdnyakov⁶⁴, P. Pralavorio⁸⁴, A. Pranko¹⁵, S. Prasad³⁰,
 R. Pravahan⁸, S. Prell⁶³, D. Price⁸³, J. Price⁷³, L.E. Price⁶, D. Prieur¹²⁴,
 M. Primavera^{72a}, M. Proissl⁴⁶, K. Prokofiev⁴⁷, F. Prokoshin^{32b},
 E. Protopapadaki¹³⁷, S. Protopopescu²⁵, J. Proudfoot⁶, M. Przybycien^{38a},
 H. Przysiezniak⁵, E. Ptacek¹¹⁵, D. Puddu^{135a,135b}, E. Pueschel⁸⁵,
 D. Puldon¹⁴⁹, M. Purohit^{25,ad}, P. Puzo¹¹⁶, J. Qian⁸⁸, G. Qin⁵³, Y. Qin⁸³,
 A. Quadt⁵⁴, D.R. Quarrie¹⁵, W.B. Quayle^{165a,165b},
 M. Queitsch-Maitland⁸³, D. Quilty⁵³, A. Qureshi^{160b}, V. Radeka²⁵,
 V. Radescu⁴², S.K. Radhakrishnan¹⁴⁹, P. Radloff¹¹⁵, P. Rados⁸⁷,
 F. Ragusa^{90a,90b}, G. Rahal¹⁷⁹, S. Rajagopalan²⁵, M. Rammensee³⁰,
 A.S. Randle-Conde⁴⁰, C. Rangel-Smith¹⁶⁷, K. Rao¹⁶⁴, F. Rauscher⁹⁹,
 T.C. Rave⁴⁸, T. Ravenscroft⁵³, M. Raymond³⁰, A.L. Read¹¹⁸,
 N.P. Readloff⁷³, D.M. Rebuffi^{120a,120b}, A. Redelbach¹⁷⁵, G. Redlinger²⁵,
 R. Reece¹³⁸, K. Reeves⁴¹, L. Rehnisch¹⁶, H. Reisin²⁷, M. Relich¹⁶⁴,
 C. Rembser³⁰, H. Ren^{33a}, Z.L. Ren¹⁵², A. Renaud¹¹⁶, M. Rescigno^{133a},
 S. Resconi^{90a}, O.L. Rezanova^{108,c}, P. Reznicek¹²⁸, R. Rezvani⁹⁴,
 R. Richter¹⁰⁰, M. Ridel⁷⁹, P. Rieck¹⁶, J. Rieger⁵⁴, M. Rijssenbeek¹⁴⁹,
 A. Rimoldi^{120a,120b}, L. Rinaldi^{20a}, E. Ritsch⁶¹, I. Riu¹², F. Rizatdinova¹¹³,
 E. Rizvi⁷⁵, S.H. Robertson^{86,k}, A. Robichaud-Veronneau⁸⁶,
 D. Robinson²⁸, J.E.M. Robinson⁸³, A. Robson⁵³, C. Roda^{123a,123b},
 L. Rodrigues³⁰, S. Roe³⁰, O. Røhne¹¹⁸, S. Rolli¹⁶², A. Romaniouk⁹⁷,
 M. Romano^{20a,20b}, E. Romero Adam¹⁶⁸, N. Rompotis¹³⁹, M. Ronzani⁴⁸,

L. Roos⁷⁹, E. Ros¹⁶⁸, S. Rosati^{133a}, K. Rosbach⁴⁹, M. Rose⁷⁶, P. Rose¹³⁸,
 P.L. Rosendahl¹⁴, O. Rosenthal¹⁴², V. Rossetti^{147a,147b}, E. Rossi^{103a,103b},
 L.P. Rossi^{50a}, R. Rosten¹³⁹, M. Rotaru^{26a}, I. Roth¹⁷³, J. Rothberg¹³⁹,
 D. Rousseau¹¹⁶, C.R. Royon¹³⁷, A. Rozanov⁸⁴, Y. Rozen¹⁵³, X. Ruan^{146c},
 F. Rubbo¹², I. Rubinskiy⁴², V.I. Rud⁹⁸, C. Rudolph⁴⁴, M.S. Rudolph¹⁵⁹,
 F. Rühr⁴⁸, A. Ruiz-Martinez³⁰, Z. Rurikova⁴⁸, N.A. Rusakovich⁶⁴,
 A. Ruschke⁹⁹, J.P. Rutherford⁷, N. Ruthmann⁴⁸, Y.F. Ryabov¹²²,
 M. Rybar¹²⁸, G. Rybkin¹¹⁶, N.C. Ryder¹¹⁹, A.F. Saavedra¹⁵¹,
 S. Sacerdoti²⁷, A. Saddique³, I. Sadeh¹⁵⁴, H.F.W. Sadrozinski¹³⁸,
 R. Sadykov⁶⁴, F. Safai Tehrani^{133a}, H. Sakamoto¹⁵⁶, Y. Sakurai¹⁷²,
 G. Salamanna^{135a,135b}, A. Salamon^{134a}, M. Saleem¹¹², D. Salek¹⁰⁶,
 P.H. Sales De Bruin¹³⁹, D. Salihagic¹⁰⁰, A. Salnikov¹⁴⁴, J. Salt¹⁶⁸,
 D. Salvatore^{37a,37b}, F. Salvatore¹⁵⁰, A. Salvucci¹⁰⁵, A. Salzburger³⁰,
 D. Sampsonidis¹⁵⁵, A. Sanchez^{103a,103b}, J. Sánchez¹⁶⁸,
 V. Sanchez Martinez¹⁶⁸, H. Sandaker¹⁴, R.L. Sandbach⁷⁵, H.G. Sander⁸²,
 M.P. Sanders⁹⁹, M. Sandhoff¹⁷⁶, T. Sandoval²⁸, C. Sandoval¹⁶³,
 R. Sandstroem¹⁰⁰, D.P.C. Sankey¹³⁰, A. Sansoni⁴⁷, C. Santoni³⁴,
 R. Santonico^{134a,134b}, H. Santos^{125a}, I. Santoyo Castillo¹⁵⁰, K. Sapp¹²⁴,
 A. Saponov⁶⁴, J.G. Saraiva^{125a,125d}, B. Sarrazin²¹, G. Sartisohn¹⁷⁶,
 O. Sasaki⁶⁵, Y. Sasaki¹⁵⁶, G. Sauvage^{5,*}, E. Sauvan⁵, P. Savard^{159,e},
 D.O. Savu³⁰, C. Sawyer¹¹⁹, L. Sawyer^{78,n}, D.H. Saxon⁵³, J. Saxon¹²¹,
 C. Sbarra^{20a}, A. Sbrizzi^{20a,20b}, T. Scanlon⁷⁷, D.A. Scannicchio¹⁶⁴,
 M. Scarcella¹⁵¹, V. Scarfone^{37a,37b}, J. Schaarschmidt¹⁷³, P. Schacht¹⁰⁰,
 D. Schaefer³⁰, R. Schaefer⁴², S. Schaepe²¹, S. Schaezel^{58b},
 U. Schäfer⁸², A.C. Schaffer¹¹⁶, D. Schaile⁹⁹, R.D. Schamberger¹⁴⁹,
 V. Scharf^{58a}, V.A. Schegelsky¹²², D. Scheirich¹²⁸, M. Schernau¹⁶⁴,
 M.I. Scherzer³⁵, C. Schiavi^{50a,50b}, J. Schieck⁹⁹, C. Schillo⁴⁸,
 M. Schioppa^{37a,37b}, S. Schlenker³⁰, E. Schmidt⁴⁸, K. Schmieden³⁰,
 C. Schmitt⁸², S. Schmitt^{58b}, B. Schneider¹⁷, Y.J. Schnellbach⁷³,
 U. Schnoor⁴⁴, L. Schoeffel¹³⁷, A. Schoening^{58b}, B.D. Schoenrock⁸⁹,
 A.L.S. Schorlemmer⁵⁴, M. Schott⁸², D. Schouten^{160a}, J. Schovancova²⁵,
 S. Schramm¹⁵⁹, M. Schreyer¹⁷⁵, C. Schroeder⁸², N. Schuh⁸²,
 M.J. Schultens²¹, H.-C. Schultz-Coulon^{58a}, H. Schulz¹⁶,
 M. Schumacher⁴⁸, B.A. Schumm¹³⁸, Ph. Schune¹³⁷,
 C. Schwanenberger⁸³, A. Schwartzman¹⁴⁴, T.A. Schwarz⁸⁸,
 Ph. Schwegler¹⁰⁰, Ph. Schwemling¹³⁷, R. Schwienhorst⁸⁹,
 J. Schwindling¹³⁷, T. Schwindt²¹, M. Schwoerer⁵, F.G. Sciacca¹⁷,

E. Scifo ¹¹⁶, G. Sciolla ²³, W.G. Scott ¹³⁰, F. Scuri ^{123a,123b}, F. Scutti ²¹,
 J. Searcy ⁸⁸, G. Sedov ⁴², E. Sedykh ¹²², S.C. Seidel ¹⁰⁴, A. Seiden ¹³⁸,
 F. Seifert ¹²⁷, J.M. Seixas ^{24a}, G. Sekhniaidze ^{103a}, S.J. Sekula ⁴⁰,
 K.E. Selbach ⁴⁶, D.M. Seliverstov ^{122,*}, G. Sellers ⁷³,
 N. Semprini-Cesari ^{20a,20b}, C. Serfon ³⁰, L. Serin ¹¹⁶, L. Serkin ⁵⁴,
 T. Serre ⁸⁴, R. Seuster ^{160a}, H. Severini ¹¹², T. Sfiligoj ⁷⁴, F. Sforza ¹⁰⁰,
 A. Sfyrla ³⁰, E. Shabalina ⁵⁴, M. Shamim ¹¹⁵, L.Y. Shan ^{33a}, R. Shang ¹⁶⁶,
 J.T. Shank ²², M. Shapiro ¹⁵, P.B. Shatalov ⁹⁶, K. Shaw ^{165a,165b},
 C.Y. Shehu ¹⁵⁰, P. Sherwood ⁷⁷, L. Shi ^{152,ae}, S. Shimizu ⁶⁶,
 C.O. Shimmin ¹⁶⁴, M. Shimojima ¹⁰¹, M. Shiyakova ⁶⁴, A. Shmeleva ⁹⁵,
 M.J. Shochet ³¹, D. Short ¹¹⁹, S. Shrestha ⁶³, E. Shulga ⁹⁷, M.A. Shupe ⁷,
 S. Shushkevich ⁴², P. Sicho ¹²⁶, O. Sidiropoulou ¹⁵⁵, D. Sidorov ¹¹³,
 A. Sidoti ^{133a}, F. Siegert ⁴⁴, Dj. Sijacki ^{13a}, J. Silva ^{125a,125d}, Y. Silver ¹⁵⁴,
 D. Silverstein ¹⁴⁴, S.B. Silverstein ^{147a}, V. Simak ¹²⁷, O. Simard ⁵,
 Lj. Simic ^{13a}, S. Simion ¹¹⁶, E. Simioni ⁸², B. Simmons ⁷⁷,
 R. Simoniello ^{90a,90b}, M. Simonyan ³⁶, P. Sinervo ¹⁵⁹, N.B. Sinev ¹¹⁵,
 V. Sipica ¹⁴², G. Siragusa ¹⁷⁵, A. Sircar ⁷⁸, A.N. Sisakyan ^{64,*},
 S.Yu. Sivoklokov ⁹⁸, J. Sjölin ^{147a,147b}, T.B. Sjursen ¹⁴, H.P. Skottowe ⁵⁷,
 K.Yu. Skovpen ¹⁰⁸, P. Skubic ¹¹², M. Slater ¹⁸, T. Slavicek ¹²⁷, K. Sliwa ¹⁶²,
 V. Smakhtin ¹⁷³, B.H. Smart ⁴⁶, L. Smestad ¹⁴, S.Yu. Smirnov ⁹⁷,
 Y. Smirnov ⁹⁷, L.N. Smirnova ^{98,af}, O. Smirnova ⁸⁰, K.M. Smith ⁵³,
 M. Smizanska ⁷¹, K. Smolek ¹²⁷, A.A. Snesarev ⁹⁵, G. Snidero ⁷⁵,
 S. Snyder ²⁵, R. Sobie ^{170,k}, F. Socher ⁴⁴, A. Soffer ¹⁵⁴, D.A. Soh ^{152,ae},
 C.A. Solans ³⁰, M. Solar ¹²⁷, J. Solc ¹²⁷, E.Yu. Soldatov ⁹⁷, U. Soldevila ¹⁶⁸,
 A.A. Solodkov ¹²⁹, A. Soloshenko ⁶⁴, O.V. Solovyanov ¹²⁹, V. Solovyev ¹²²,
 P. Sommer ⁴⁸, H.Y. Song ^{33b}, N. Soni ¹, A. Sood ¹⁵, A. Sopczak ¹²⁷,
 B. Sopko ¹²⁷, V. Sopko ¹²⁷, V. Sorin ¹², M. Sosebee ⁸, R. Soualah ^{165a,165c},
 P. Soueid ⁹⁴, A.M. Soukharev ^{108,c}, D. South ⁴², S. Spagnolo ^{72a,72b},
 F. Spanò ⁷⁶, W.R. Spearman ⁵⁷, F. Spettel ¹⁰⁰, R. Spighi ^{20a}, G. Spigo ³⁰,
 L.A. Spiller ⁸⁷, M. Spousta ¹²⁸, T. Spreitzer ¹⁵⁹, B. Spurlock ⁸,
 R.D. St. Denis ^{53,*}, S. Staerz ⁴⁴, J. Stahlman ¹²¹, R. Stamen ^{58a}, S. Stamm ¹⁶,
 E. Stanecka ³⁹, R.W. Stanek ⁶, C. Stanescu ^{135a}, M. Stanescu-Bellu ⁴²,
 M.M. Stanitzki ⁴², S. Stapnes ¹¹⁸, E.A. Starchenko ¹²⁹, J. Stark ⁵⁵,
 P. Staroba ¹²⁶, P. Starovoitov ⁴², R. Staszewski ³⁹, P. Stavina ^{145a,*},
 P. Steinberg ²⁵, B. Stelzer ¹⁴³, H.J. Stelzer ³⁰, O. Stelzer-Chilton ^{160a},
 H. Stenzel ⁵², S. Stern ¹⁰⁰, G.A. Stewart ⁵³, J.A. Stillings ²¹,
 M.C. Stockton ⁸⁶, M. Stoebe ⁸⁶, G. Stoica ^{26a}, P. Stolte ⁵⁴, S. Stonjek ¹⁰⁰,

A.R. Stradling⁸, A. Straessner⁴⁴, M.E. Stramaglia¹⁷, J. Strandberg¹⁴⁸,
 S. Strandberg^{147a,147b}, A. Strandlie¹¹⁸, E. Strauss¹⁴⁴, M. Strauss¹¹²,
 P. Strizenc^{145b}, R. Ströhmer¹⁷⁵, D.M. Strom¹¹⁵, R. Stroynowski⁴⁰,
 A. Strubig¹⁰⁵, S.A. Stucci¹⁷, B. Stugu¹⁴, N.A. Styles⁴², D. Su¹⁴⁴,
 J. Su¹²⁴, R. Subramaniam⁷⁸, A. Succurro¹², Y. Sugaya¹¹⁷, C. Suhr¹⁰⁷,
 M. Suk¹²⁷, V.V. Sulin⁹⁵, S. Sultansoy^{4c}, T. Sumida⁶⁷, S. Sun⁵⁷,
 X. Sun^{33a}, J.E. Sundermann⁴⁸, K. Suruliz¹⁴⁰, G. Susinno^{37a,37b},
 M.R. Sutton¹⁵⁰, Y. Suzuki⁶⁵, M. Svatos¹²⁶, S. Swedish¹⁶⁹,
 M. Swiatlowski¹⁴⁴, I. Sykora^{145a}, T. Sykora¹²⁸, D. Ta⁸⁹,
 C. Taccini^{135a,135b}, K. Tackmann⁴², J. Taenzer¹⁵⁹, A. Taffard¹⁶⁴,
 R. Tafirout^{160a}, N. Taiblum¹⁵⁴, H. Takai²⁵, R. Takashima⁶⁸, H. Takeda⁶⁶,
 T. Takeshita¹⁴¹, Y. Takubo⁶⁵, M. Talby⁸⁴, A.A. Talyshev^{108,c},
 J.Y.C. Tam¹⁷⁵, K.G. Tan⁸⁷, J. Tanaka¹⁵⁶, R. Tanaka¹¹⁶, S. Tanaka¹³²,
 S. Tanaka⁶⁵, A.J. Tanasijczuk¹⁴³, B.B. Tannenwald¹¹⁰, N. Tannoury²¹,
 S. Tapprogge⁸², S. Tarem¹⁵³, F. Tarrade²⁹, G.F. Tartarelli^{90a}, P. Tas¹²⁸,
 M. Tasevsky¹²⁶, T. Tashiro⁶⁷, E. Tassi^{37a,37b}, A. Tavares Delgado^{125a,125b},
 Y. Tayalati^{136d}, F.E. Taylor⁹³, G.N. Taylor⁸⁷, W. Taylor^{160b},
 F.A. Teischinger³⁰, M. Teixeira Dias Castanheira⁷⁵, P. Teixeira-Dias⁷⁶,
 K.K. Temming⁴⁸, H. Ten Kate³⁰, P.K. Teng¹⁵², J.J. Teoh¹¹⁷, S. Terada⁶⁵,
 K. Terashi¹⁵⁶, J. Terron⁸¹, S. Terzo¹⁰⁰, M. Testa⁴⁷, R.J. Teuscher^{159,k},
 J. Therhaag²¹, T. Theveneaux-Pelzer³⁴, J.P. Thomas¹⁸,
 J. Thomas-Wilsker⁷⁶, E.N. Thompson³⁵, P.D. Thompson¹⁸,
 P.D. Thompson¹⁵⁹, R.J. Thompson⁸³, A.S. Thompson⁵³,
 L.A. Thomsen³⁶, E. Thomson¹²¹, M. Thomson²⁸, W.M. Thong⁸⁷,
 R.P. Thun^{88,*}, F. Tian³⁵, M.J. Tibbetts¹⁵, V.O. Tikhomirov^{95,ag},
 Yu.A. Tikhonov^{108,c}, S. Timoshenko⁹⁷, E. Tiouchichine⁸⁴, P. Tipton¹⁷⁷,
 S. Tisserant⁸⁴, T. Todorov⁵, S. Todorova-Nova¹²⁸, B. Toggerson⁷,
 J. Tojo⁶⁹, S. Tokár^{145a}, K. Tokushuku⁶⁵, K. Tollefson⁸⁹, E. Tolley⁵⁷,
 L. Tomlinson⁸³, M. Tomoto¹⁰², L. Tompkins³¹, K. Toms¹⁰⁴,
 N.D. Topilin⁶⁴, E. Torrence¹¹⁵, H. Torres¹⁴³, E. Torró Pastor¹⁶⁸,
 J. Toth^{84,ah}, F. Touchard⁸⁴, D.R. Tovey¹⁴⁰, H.L. Tran¹¹⁶, T. Trefzger¹⁷⁵,
 L. Tremblet³⁰, A. Tricoli³⁰, I.M. Trigger^{160a}, S. Trincaz-Duvoid⁷⁹,
 M.F. Tripiana¹², W. Trischuk¹⁵⁹, B. Trocmé⁵⁵, C. Troncon^{90a},
 M. Trottier-McDonald¹⁵, M. Trovatelli^{135a,135b}, P. True⁸⁹,
 M. Trzebinski³⁹, A. Trzupek³⁹, C. Tsarouchas³⁰, J.C-L. Tseng¹¹⁹,
 P.V. Tsiarehka⁹¹, D. Tsionou¹³⁷, G. Tsipolitis¹⁰, N. Tsirintanis⁹,
 S. Tsiskaridze¹², V. Tsiskaridze⁴⁸, E.G. Tskhadadze^{51a}, I.I. Tsukerman⁹⁶,

V. Tsulaia¹⁵, S. Tsuno⁶⁵, D. Tsybychev¹⁴⁹, A. Tudorache^{26a},
 V. Tudorache^{26a}, A.N. Tuna¹²¹, S.A. Tupputi^{20a,20b}, S. Turchikhin^{98,af},
 D. Turecek¹²⁷, I. Turk Cakir^{4d}, R. Turra^{90a,90b}, P.M. Tuts³⁵,
 A. Tykhonov⁴⁹, M. Tylmad^{147a,147b}, M. Tyndel¹³⁰, K. Uchida²¹,
 I. Ueda¹⁵⁶, R. Ueno²⁹, M. Ughetto⁸⁴, M. Ugland¹⁴, M. Uhlenbrock²¹,
 F. Ukegawa¹⁶¹, G. Unal³⁰, A. Undrus²⁵, G. Unel¹⁶⁴, F.C. Ungaro⁴⁸,
 Y. Unno⁶⁵, C. Unverdorben⁹⁹, D. Urbaniec³⁵, P. Urquijo⁸⁷, G. Usai⁸,
 A. Usanova⁶¹, L. Vacavant⁸⁴, V. Vacek¹²⁷, B. Vachon⁸⁶, N. Valencic¹⁰⁶,
 S. Valentineti^{20a,20b}, A. Valero¹⁶⁸, L. Valery³⁴, S. Valkar¹²⁸,
 E. Valladolid Gallego¹⁶⁸, S. Vallecorsa⁴⁹, J.A. Valls Ferrer¹⁶⁸,
 W. Van Den Wollenberg¹⁰⁶, P.C. Van Der Deijl¹⁰⁶, R. van der Geer¹⁰⁶,
 H. van der Graaf¹⁰⁶, R. Van Der Leeuw¹⁰⁶, D. van der Ster³⁰,
 N. van Eldik³⁰, P. van Gemmeren⁶, J. Van Nieuwkoop¹⁴³,
 I. van Vulpen¹⁰⁶, M.C. van Woerden³⁰, M. Vanadia^{133a,133b},
 W. Vandelli³⁰, R. Vanguri¹²¹, A. Vaniachine⁶, P. Vankov⁴²,
 F. Vannucci⁷⁹, G. Vardanyan¹⁷⁸, R. Vari^{133a}, E.W. Varnes⁷, T. Varol⁸⁵,
 D. Varouchas⁷⁹, A. Vartapetian⁸, K.E. Varvell¹⁵¹, F. Vazeille³⁴,
 T. Vazquez Schroeder⁵⁴, J. Veatch⁷, F. Veloso^{125a,125c}, T. Velz²¹,
 S. Veneziano^{133a}, A. Ventura^{72a,72b}, D. Ventura⁸⁵, M. Venturi¹⁷⁰,
 N. Venturi¹⁵⁹, A. Venturini²³, V. Vercesi^{120a}, M. Verducci^{133a,133b},
 W. Verkerke¹⁰⁶, J.C. Vermeulen¹⁰⁶, A. Vest⁴⁴, M.C. Vetterli^{143,e},
 O. Viazlo⁸⁰, I. Vichou¹⁶⁶, T. Vickey^{146c,ai}, O.E. Vickey Boeriu^{146c},
 G.H.A. Viehhauser¹¹⁹, S. Viel¹⁶⁹, R. Vigne³⁰, M. Villa^{20a,20b},
 M. Villaplana Perez^{90a,90b}, E. Vilucchi⁴⁷, M.G. Vincter²⁹,
 V.B. Vinogradov⁶⁴, J. Virzi¹⁵, I. Vivarelli¹⁵⁰, F. Vives Vaque³,
 S. Vlachos¹⁰, D. Vladoiu⁹⁹, M. Vlasak¹²⁷, A. Vogel²¹, M. Vogel^{32a},
 P. Vokac¹²⁷, G. Volpi^{123a,123b}, M. Volpi⁸⁷, H. von der Schmitt¹⁰⁰,
 H. von Radziewski⁴⁸, E. von Toerne²¹, V. Vorobel¹²⁸, K. Vorobev⁹⁷,
 M. Vos¹⁶⁸, R. Voss³⁰, J.H. Vossebeld⁷³, N. Vranjes¹³⁷,
 M. Vranjes Milosavljevic^{13a}, V. Vrba¹²⁶, M. Vreeswijk¹⁰⁶, T. Vu Anh⁴⁸,
 R. Vuillermet³⁰, I. Vukotic³¹, Z. Vykydal¹²⁷, P. Wagner²¹, W. Wagner¹⁷⁶,
 H. Wahlberg⁷⁰, S. Wahrmund⁴⁴, J. Wakabayashi¹⁰², J. Walder⁷¹,
 R. Walker⁹⁹, W. Walkowiak¹⁴², R. Wall¹⁷⁷, P. Waller⁷³, B. Walsh¹⁷⁷,
 C. Wang^{152,aj}, C. Wang⁴⁵, F. Wang¹⁷⁴, H. Wang¹⁵, H. Wang⁴⁰, J. Wang⁴²,
 J. Wang^{33a}, K. Wang⁸⁶, R. Wang¹⁰⁴, S.M. Wang¹⁵², T. Wang²¹,
 X. Wang¹⁷⁷, C. Wanotayaroj¹¹⁵, A. Warburton⁸⁶, C.P. Ward²⁸,
 D.R. Wardrope⁷⁷, M. Warsinsky⁴⁸, A. Washbrook⁴⁶, C. Wasicki⁴²,

P.M. Watkins¹⁸, A.T. Watson¹⁸, I.J. Watson¹⁵¹, M.F. Watson¹⁸,
 G. Watts¹³⁹, S. Watts⁸³, B.M. Waugh⁷⁷, S. Webb⁸³, M.S. Weber¹⁷,
 S.W. Weber¹⁷⁵, J.S. Webster³¹, A.R. Weidberg¹¹⁹, P. Weigell¹⁰⁰,
 B. Weinert⁶⁰, J. Weingarten⁵⁴, C. Weiser⁴⁸, H. Weits¹⁰⁶, P.S. Wells³⁰,
 T. Wenaus²⁵, D. Wendland¹⁶, Z. Weng^{152,ae}, T. Wengler³⁰, S. Wenig³⁰,
 N. Wermes²¹, M. Werner⁴⁸, P. Werner³⁰, M. Wessels^{58a}, J. Wetter¹⁶²,
 K. Whalen²⁹, A. White⁸, M.J. White¹, R. White^{32b}, S. White^{123a,123b},
 D. Whiteson¹⁶⁴, D. Wicke¹⁷⁶, F.J. Wickens¹³⁰, W. Wiedenmann¹⁷⁴,
 M. Wielers¹³⁰, P. Wienemann²¹, C. Wiglesworth³⁶,
 L.A.M. Wiik-Fuchs²¹, P.A. Wijeratne⁷⁷, A. Wildauer¹⁰⁰, M.A. Wildt^{42,ak},
 H.G. Wilkens³⁰, J.Z. Will⁹⁹, H.H. Williams¹²¹, S. Williams²⁸,
 C. Willis⁸⁹, S. Willocq⁸⁵, A. Wilson⁸⁸, J.A. Wilson¹⁸,
 I. Wingerter-Seez⁵, F. Winklmeier¹¹⁵, B.T. Winter²¹, M. Wittgen¹⁴⁴,
 T. Wittig⁴³, J. Wittkowski⁹⁹, S.J. Wollstadt⁸², M.W. Wolter³⁹,
 H. Wolters^{125a,125c}, B.K. Wosiek³⁹, J. Wotschack³⁰, M.J. Woudstra⁸³,
 K.W. Wozniak³⁹, M. Wright⁵³, M. Wu⁵⁵, S.L. Wu¹⁷⁴, X. Wu⁴⁹, Y. Wu⁸⁸,
 E. Wulf³⁵, T.R. Wyatt⁸³, B.M. Wynne⁴⁶, S. Xella³⁶, M. Xiao¹³⁷,
 D. Xu^{33a}, L. Xu^{33b,al}, B. Yabsley¹⁵¹, S. Yacoob^{146b,am}, R. Yakabe⁶⁶,
 M. Yamada⁶⁵, H. Yamaguchi¹⁵⁶, Y. Yamaguchi¹¹⁷, A. Yamamoto⁶⁵,
 K. Yamamoto⁶³, S. Yamamoto¹⁵⁶, T. Yamamura¹⁵⁶, T. Yamanaka¹⁵⁶,
 K. Yamauchi¹⁰², Y. Yamazaki⁶⁶, Z. Yan²², H. Yang^{33e}, H. Yang¹⁷⁴,
 U.K. Yang⁸³, Y. Yang¹¹⁰, S. Yanush⁹², L. Yao^{33a}, W-M. Yao¹⁵,
 Y. Yasu⁶⁵, E. Yatsenko⁴², K.H. Yau Wong²¹, J. Ye⁴⁰, S. Ye²⁵,
 I. Yeletsikh⁶⁴, A.L. Yen⁵⁷, E. Yildirim⁴², M. Yilmaz^{4b},
 R. Yoosofmiya¹²⁴, K. Yorita¹⁷², R. Yoshida⁶, K. Yoshihara¹⁵⁶,
 C. Young¹⁴⁴, C.J.S. Young³⁰, S. Youssef²², D.R. Yu¹⁵, J. Yu⁸, J.M. Yu⁸⁸,
 J. Yu¹¹³, L. Yuan⁶⁶, A. Yurkewicz¹⁰⁷, I. Yusuff^{28,an}, B. Zabinski³⁹,
 R. Zaidan⁶², A.M. Zaitsev^{129,aa}, A. Zaman¹⁴⁹, S. Zambito²³,
 L. Zanello^{133a,133b}, D. Zanzi¹⁰⁰, C. Zeitnitz¹⁷⁶, M. Zeman¹²⁷, A. Zemla^{38a},
 K. Zengel²³, O. Zenin¹²⁹, T. Ženiš^{145a}, D. Zerwas¹¹⁶,
 G. Zevi della Porta⁵⁷, D. Zhang⁸⁸, F. Zhang¹⁷⁴, H. Zhang⁸⁹, J. Zhang⁶,
 L. Zhang¹⁵², X. Zhang^{33d}, Z. Zhang¹¹⁶, Z. Zhao^{33b}, A. Zhemchugov⁶⁴,
 J. Zhong¹¹⁹, B. Zhou⁸⁸, L. Zhou³⁵, N. Zhou¹⁶⁴, C.G. Zhu^{33d}, H. Zhu^{33a},
 J. Zhu⁸⁸, Y. Zhu^{33b}, X. Zhuang^{33a}, K. Zhukov⁹⁵, A. Zibell¹⁷⁵,
 D. Zieminska⁶⁰, N.I. Zimine⁶⁴, C. Zimmermann⁸², R. Zimmermann²¹,
 S. Zimmermann²¹, S. Zimmermann⁴⁸, Z. Zinonos⁵⁴, M. Ziolkowski¹⁴²,

G. Zobernig¹⁷⁴, A. Zoccoli^{20a,20b}, M. zur Nedden¹⁶, G. Zurzolo^{103a,103b},
V. Zutshi¹⁰⁷, L. Zwalinski³⁰

¹ Department of Physics, University of Adelaide, Adelaide, Australia

² Physics Department, SUNY Albany, Albany, NY, United States

³ Department of Physics, University of Alberta, Edmonton, AB, Canada

⁴ (a) Department of Physics, Ankara University, Ankara; (b) Department of Physics, Gazi University, Ankara;

(c) Division of Physics, TOBB University of Economics and Technology, Ankara; (d) Turkish Atomic Energy Authority, Ankara, Turkey

⁵ LAPP, CNRS/IN2P3 and Université de Savoie, Annecy-le-Vieux, France

⁶ High Energy Physics Division, Argonne National Laboratory, Argonne, IL, United States

⁷ Department of Physics, University of Arizona, Tucson, AZ, United States

⁸ Department of Physics, The University of Texas at Arlington, Arlington, TX, United States

⁹ Physics Department, University of Athens, Athens, Greece

¹⁰ Physics Department, National Technical University of Athens, Zografou, Greece

¹¹ Institute of Physics, Azerbaijan Academy of Sciences, Baku, Azerbaijan

¹² Institut de Física d'Altes Energies and Departament de Física de la Universitat Autònoma de Barcelona, Barcelona, Spain

¹³ (a) Institute of Physics, University of Belgrade, Belgrade; (b) Vinca Institute of Nuclear Sciences, University of Belgrade, Belgrade, Serbia

¹⁴ Department for Physics and Technology, University of Bergen, Bergen, Norway

¹⁵ Physics Division, Lawrence Berkeley National Laboratory and University of California, Berkeley, CA, United States

¹⁶ Department of Physics, Humboldt University, Berlin, Germany

¹⁷ Albert Einstein Center for Fundamental Physics and Laboratory for High Energy Physics, University of Bern, Bern, Switzerland

¹⁸ School of Physics and Astronomy, University of Birmingham, Birmingham, United Kingdom

¹⁹ (a) Department of Physics, Bogazici University, Istanbul; (b) Department of Physics, Dogus University, Istanbul;

(c) Department of Physics Engineering, Gaziantep University, Gaziantep, Turkey

²⁰ (a) INFN Sezione di Bologna; (b) Dipartimento di Fisica e Astronomia, Università di Bologna, Bologna, Italy

²¹ Physikalisches Institut, University of Bonn, Bonn, Germany

²² Department of Physics, Boston University, Boston, MA, United States

²³ Department of Physics, Brandeis University, Waltham, MA, United States

²⁴ (a) Universidade Federal do Rio De Janeiro COPPE/EE/IF, Rio de Janeiro; (b) Electrical Circuits Department, Federal University of Juiz de Fora (UFJF), Juiz de Fora; (c) Federal University of Sao Joao del Rei (UFSJ), Sao Joao del Rei; (d) Instituto de Física, Universidade de Sao Paulo, Sao Paulo, Brazil

²⁵ Physics Department, Brookhaven National Laboratory, Upton, NY, United States

²⁶ (a) National Institute of Physics and Nuclear Engineering, Bucharest; (b) National Institute for Research and Development of Isotopic and Molecular Technologies, Physics Department, Cluj Napoca; (c) University Politehnica Bucharest, Bucharest; (d) West University in Timisoara, Timisoara, Romania

²⁷ Departamento de Física, Universidad de Buenos Aires, Buenos Aires, Argentina

²⁸ Cavendish Laboratory, University of Cambridge, Cambridge, United Kingdom

²⁹ Department of Physics, Carleton University, Ottawa, ON, Canada

³⁰ CERN, Geneva, Switzerland

³¹ Enrico Fermi Institute, University of Chicago, Chicago, IL, United States

³² (a) Departamento de Física, Pontificia Universidad Católica de Chile, Santiago; (b) Departamento de Física, Universidad Técnica Federico Santa María, Valparaíso, Chile

³³ (a) Institute of High Energy Physics, Chinese Academy of Sciences, Beijing; (b) Department of Modern Physics, University of Science and Technology of China, Anhui; (c) Department of Physics, Nanjing University, Jiangsu;

(d) School of Physics, Shandong University, Shandong; (e) Physics Department, Shanghai Jiao Tong University, Shanghai, China

³⁴ Laboratoire de Physique Corpusculaire, Clermont Université and Université Blaise Pascal and CNRS/IN2P3, Clermont-Ferrand, France

³⁵ Nevis Laboratory, Columbia University, Irvington, NY, United States

³⁶ Niels Bohr Institute, University of Copenhagen, Kobenhavn, Denmark

- 37 (a) INFN Gruppo Collegato di Cosenza, Laboratori Nazionali di Frascati; (b) Dipartimento di Fisica, Università della Calabria, Rende, Italy
- 38 (a) AGH University of Science and Technology, Faculty of Physics and Applied Computer Science, Krakow; (b) Marian Smoluchowski Institute of Physics, Jagiellonian University, Krakow, Poland
- 39 The Henryk Niewodniczanski Institute of Nuclear Physics, Polish Academy of Sciences, Krakow, Poland
- 40 Physics Department, Southern Methodist University, Dallas, TX, United States
- 41 Physics Department, University of Texas at Dallas, Richardson, TX, United States
- 42 DESY, Hamburg and Zeuthen, Germany
- 43 Institut für Experimentelle Physik IV, Technische Universität Dortmund, Dortmund, Germany
- 44 Institut für Kern- und Teilchenphysik, Technische Universität Dresden, Dresden, Germany
- 45 Department of Physics, Duke University, Durham, NC, United States
- 46 SUPA – School of Physics and Astronomy, University of Edinburgh, Edinburgh, United Kingdom
- 47 INFN Laboratori Nazionali di Frascati, Frascati, Italy
- 48 Fakultät für Mathematik und Physik, Albert-Ludwigs-Universität, Freiburg, Germany
- 49 Section de Physique, Université de Genève, Geneva, Switzerland
- 50 (a) INFN Sezione di Genova; (b) Dipartimento di Fisica, Università di Genova, Genova, Italy
- 51 (a) E. Andronikashvili Institute of Physics, Iv. Javakhishvili Tbilisi State University, Tbilisi; (b) High Energy Physics Institute, Tbilisi State University, Tbilisi, Georgia
- 52 II Physikalisches Institut, Justus-Liebig-Universität Giessen, Giessen, Germany
- 53 SUPA – School of Physics and Astronomy, University of Glasgow, Glasgow, United Kingdom
- 54 II Physikalisches Institut, Georg-August-Universität, Göttingen, Germany
- 55 Laboratoire de Physique Subatomique et de Cosmologie, Université Grenoble-Alpes, CNRS/IN2P3, Grenoble, France
- 56 Department of Physics, Hampton University, Hampton, VA, United States
- 57 Laboratory for Particle Physics and Cosmology, Harvard University, Cambridge, MA, United States
- 58 (a) Kirchhoff-Institut für Physik, Ruprecht-Karls-Universität Heidelberg, Heidelberg; (b) Physikalisches Institut, Ruprecht-Karls-Universität Heidelberg, Heidelberg; (c) ZITI Institut für technische Informatik, Ruprecht-Karls-Universität Heidelberg, Mannheim, Germany
- 59 Faculty of Applied Information Science, Hiroshima Institute of Technology, Hiroshima, Japan
- 60 Department of Physics, Indiana University, Bloomington, IN, United States
- 61 Institut für Astro- und Teilchenphysik, Leopold-Franzens-Universität, Innsbruck, Austria
- 62 University of Iowa, Iowa City, IA, United States
- 63 Department of Physics and Astronomy, Iowa State University, Ames, IA, United States
- 64 Joint Institute for Nuclear Research, JINR Dubna, Dubna, Russia
- 65 KEK, High Energy Accelerator Research Organization, Tsukuba, Japan
- 66 Graduate School of Science, Kobe University, Kobe, Japan
- 67 Faculty of Science, Kyoto University, Kyoto, Japan
- 68 Kyoto University of Education, Kyoto, Japan
- 69 Department of Physics, Kyushu University, Fukuoka, Japan
- 70 Instituto de Física La Plata, Universidad Nacional de La Plata and CONICET, La Plata, Argentina
- 71 Physics Department, Lancaster University, Lancaster, United Kingdom
- 72 (a) INFN Sezione di Lecce; (b) Dipartimento di Matematica e Fisica, Università del Salento, Lecce, Italy
- 73 Oliver Lodge Laboratory, University of Liverpool, Liverpool, United Kingdom
- 74 Department of Physics, Jožef Stefan Institute and University of Ljubljana, Ljubljana, Slovenia
- 75 School of Physics and Astronomy, Queen Mary University of London, London, United Kingdom
- 76 Department of Physics, Royal Holloway University of London, Surrey, United Kingdom
- 77 Department of Physics and Astronomy, University College London, London, United Kingdom
- 78 Louisiana Tech University, Ruston, LA, United States
- 79 Laboratoire de Physique Nucléaire et de Hautes Energies, UPMC and Université Paris-Diderot and CNRS/IN2P3, Paris, France
- 80 Fysiska institutionen, Lunds universitet, Lund, Sweden
- 81 Departamento de Física Teórica C-15, Universidad Autónoma de Madrid, Madrid, Spain
- 82 Institut für Physik, Universität Mainz, Mainz, Germany
- 83 School of Physics and Astronomy, University of Manchester, Manchester, United Kingdom
- 84 CPPM, Aix-Marseille Université and CNRS/IN2P3, Marseille, France
- 85 Department of Physics, University of Massachusetts, Amherst, MA, United States

- 86 *Department of Physics, McGill University, Montreal, QC, Canada*
- 87 *School of Physics, University of Melbourne, Victoria, Australia*
- 88 *Department of Physics, The University of Michigan, Ann Arbor, MI, United States*
- 89 *Department of Physics and Astronomy, Michigan State University, East Lansing, MI, United States*
- 90 ^(a) *INFN Sezione di Milano;* ^(b) *Dipartimento di Fisica, Università di Milano, Milano, Italy*
- 91 *B.I. Stepanov Institute of Physics, National Academy of Sciences of Belarus, Minsk, Belarus*
- 92 *National Scientific and Educational Centre for Particle and High Energy Physics, Minsk, Belarus*
- 93 *Department of Physics, Massachusetts Institute of Technology, Cambridge, MA, United States*
- 94 *Group of Particle Physics, University of Montreal, Montreal, QC, Canada*
- 95 *P.N. Lebedev Institute of Physics, Academy of Sciences, Moscow, Russia*
- 96 *Institute for Theoretical and Experimental Physics (ITEP), Moscow, Russia*
- 97 *National Research Nuclear University MEPhI, Moscow, Russia*
- 98 *D.V. Skobeltsyn Institute of Nuclear Physics, M.V. Lomonosov Moscow State University, Moscow, Russia*
- 99 *Fakultät für Physik, Ludwig-Maximilians-Universität München, München, Germany*
- 100 *Max-Planck-Institut für Physik (Werner-Heisenberg-Institut), München, Germany*
- 101 *Nagasaki Institute of Applied Science, Nagasaki, Japan*
- 102 *Graduate School of Science and Kobayashi–Maskawa Institute, Nagoya University, Nagoya, Japan*
- 103 ^(a) *INFN Sezione di Napoli;* ^(b) *Dipartimento di Fisica, Università di Napoli, Napoli, Italy*
- 104 *Department of Physics and Astronomy, University of New Mexico, Albuquerque, NM, United States*
- 105 *Institute for Mathematics, Astrophysics and Particle Physics, Radboud University Nijmegen/Nikhef, Nijmegen, Netherlands*
- 106 *Nikhef National Institute for Subatomic Physics and University of Amsterdam, Amsterdam, Netherlands*
- 107 *Department of Physics, Northern Illinois University, DeKalb, IL, United States*
- 108 *Budker Institute of Nuclear Physics, SB RAS, Novosibirsk, Russia*
- 109 *Department of Physics, New York University, New York, NY, United States*
- 110 *Ohio State University, Columbus, OH, United States*
- 111 *Faculty of Science, Okayama University, Okayama, Japan*
- 112 *Homer L. Dodge Department of Physics and Astronomy, University of Oklahoma, Norman, OK, United States*
- 113 *Department of Physics, Oklahoma State University, Stillwater, OK, United States*
- 114 *Palacký University, RCPTM, Olomouc, Czech Republic*
- 115 *Center for High Energy Physics, University of Oregon, Eugene, OR, United States*
- 116 *LAL, Université Paris-Sud and CNRS/IN2P3, Orsay, France*
- 117 *Graduate School of Science, Osaka University, Osaka, Japan*
- 118 *Department of Physics, University of Oslo, Oslo, Norway*
- 119 *Department of Physics, Oxford University, Oxford, United Kingdom*
- 120 ^(a) *INFN Sezione di Pavia;* ^(b) *Dipartimento di Fisica, Università di Pavia, Pavia, Italy*
- 121 *Department of Physics, University of Pennsylvania, Philadelphia, PA, United States*
- 122 *Petersburg Nuclear Physics Institute, Gatchina, Russia*
- 123 ^(a) *INFN Sezione di Pisa;* ^(b) *Dipartimento di Fisica E. Fermi, Università di Pisa, Pisa, Italy*
- 124 *Department of Physics and Astronomy, University of Pittsburgh, Pittsburgh, PA, United States*
- 125 ^(a) *Laboratorio de Instrumentacao e Fisica Experimental de Particulas – LIP, Lisboa;* ^(b) *Faculdade de Ciências, Universidade de Lisboa, Lisboa;* ^(c) *Department of Physics, University of Coimbra, Coimbra;* ^(d) *Centro de Física Nuclear da Universidade de Lisboa, Lisboa;* ^(e) *Departamento de Física, Universidade do Minho, Braga;* ^(f) *Departamento de Física Teórica y del Cosmos and CAFPE, Universidad de Granada, Granada (Spain);* ^(g) *Dep. Física and CEFITEC of Faculdade de Ciências e Tecnologia, Universidade Nova de Lisboa, Caparica, Portugal*
- 126 *Institute of Physics, Academy of Sciences of the Czech Republic, Praha, Czech Republic*
- 127 *Czech Technical University in Prague, Praha, Czech Republic*
- 128 *Faculty of Mathematics and Physics, Charles University in Prague, Praha, Czech Republic*
- 129 *State Research Center Institute for High Energy Physics, Protvino, Russia*
- 130 *Particle Physics Department, Rutherford Appleton Laboratory, Didcot, United Kingdom*
- 131 *Physics Department, University of Regina, Regina, SK, Canada*
- 132 *Ritsumeikan University, Kusatsu, Shiga, Japan*
- 133 ^(a) *INFN Sezione di Roma;* ^(b) *Dipartimento di Fisica, Sapienza Università di Roma, Roma, Italy*
- 134 ^(a) *INFN Sezione di Roma Tor Vergata;* ^(b) *Dipartimento di Fisica, Università di Roma Tor Vergata, Roma, Italy*
- 135 ^(a) *INFN Sezione di Roma Tre;* ^(b) *Dipartimento di Matematica e Fisica, Università Roma Tre, Roma, Italy*

- 136 (a) *Faculté des Sciences Ain Chock, Réseau Universitaire de Physique des Hautes Energies – Université Hassan II, Casablanca*; (b) *Centre National de l’Energie des Sciences Techniques Nucleaires, Rabat*; (c) *Faculté des Sciences Semlalia, Université Cadi Ayyad, LPHEA-Marrakech*; (d) *Faculté des Sciences, Université Mohamed Premier and LPTPM, Oujda*; (e) *Faculté des sciences, Université Mohammed V-Agdal, Rabat, Morocco*
- 137 *DSM/IRFU (Institut de Recherches sur les Lois Fondamentales de l’Univers), CEA Saclay (Commissariat à l’Energie Atomique et aux Energies Alternatives), Gif-sur-Yvette, France*
- 138 *Santa Cruz Institute for Particle Physics, University of California Santa Cruz, Santa Cruz, CA, United States*
- 139 *Department of Physics, University of Washington, Seattle, WA, United States*
- 140 *Department of Physics and Astronomy, University of Sheffield, Sheffield, United Kingdom*
- 141 *Department of Physics, Shinshu University, Nagano, Japan*
- 142 *Fachbereich Physik, Universität Siegen, Siegen, Germany*
- 143 *Department of Physics, Simon Fraser University, Burnaby, BC, Canada*
- 144 *SLAC National Accelerator Laboratory, Stanford, CA, United States*
- 145 (a) *Faculty of Mathematics, Physics & Informatics, Comenius University, Bratislava*; (b) *Department of Subnuclear Physics, Institute of Experimental Physics of the Slovak Academy of Sciences, Kosice, Slovak Republic*
- 146 (a) *Department of Physics, University of Cape Town, Cape Town*; (b) *Department of Physics, University of Johannesburg, Johannesburg*; (c) *School of Physics, University of the Witwatersrand, Johannesburg, South Africa*
- 147 (a) *Department of Physics, Stockholm University*; (b) *The Oskar Klein Centre, Stockholm, Sweden*
- 148 *Physics Department, Royal Institute of Technology, Stockholm, Sweden*
- 149 *Departments of Physics & Astronomy and Chemistry, Stony Brook University, Stony Brook, NY, United States*
- 150 *Department of Physics and Astronomy, University of Sussex, Brighton, United Kingdom*
- 151 *School of Physics, University of Sydney, Sydney, Australia*
- 152 *Institute of Physics, Academia Sinica, Taipei, Taiwan*
- 153 *Department of Physics, Technion: Israel Institute of Technology, Haifa, Israel*
- 154 *Raymond and Beverly Sackler School of Physics and Astronomy, Tel Aviv University, Tel Aviv, Israel*
- 155 *Department of Physics, Aristotle University of Thessaloniki, Thessaloniki, Greece*
- 156 *International Center for Elementary Particle Physics and Department of Physics, The University of Tokyo, Tokyo, Japan*
- 157 *Graduate School of Science and Technology, Tokyo Metropolitan University, Tokyo, Japan*
- 158 *Department of Physics, Tokyo Institute of Technology, Tokyo, Japan*
- 159 *Department of Physics, University of Toronto, Toronto, ON, Canada*
- 160 (a) *TRIUMF, Vancouver, BC*; (b) *Department of Physics and Astronomy, York University, Toronto, ON, Canada*
- 161 *Faculty of Pure and Applied Sciences, University of Tsukuba, Tsukuba, Japan*
- 162 *Department of Physics and Astronomy, Tufts University, Medford, MA, United States*
- 163 *Centro de Investigaciones, Universidad Antonio Narino, Bogota, Colombia*
- 164 *Department of Physics and Astronomy, University of California Irvine, Irvine, CA, United States*
- 165 (a) *INFN Gruppo Collegato di Udine, Sezione di Trieste, Udine*; (b) *ICTP, Trieste*; (c) *Dipartimento di Chimica, Fisica e Ambiente, Università di Udine, Udine, Italy*
- 166 *Department of Physics, University of Illinois, Urbana, IL, United States*
- 167 *Department of Physics and Astronomy, University of Uppsala, Uppsala, Sweden*
- 168 *Instituto de Física Corpuscular (IFIC) and Departamento de Física Atómica, Molecular y Nuclear and Departamento de Ingeniería Electrónica and Instituto de Microelectrónica de Barcelona (IMB-CNM), University of Valencia and CSIC, Valencia, Spain*
- 169 *Department of Physics, University of British Columbia, Vancouver, BC, Canada*
- 170 *Department of Physics and Astronomy, University of Victoria, Victoria, BC, Canada*
- 171 *Department of Physics, University of Warwick, Coventry, United Kingdom*
- 172 *Waseda University, Tokyo, Japan*
- 173 *Department of Particle Physics, The Weizmann Institute of Science, Rehovot, Israel*
- 174 *Department of Physics, University of Wisconsin, Madison, WI, United States*
- 175 *Fakultät für Physik und Astronomie, Julius-Maximilians-Universität, Würzburg, Germany*
- 176 *Fachbereich C Physik, Bergische Universität Wuppertal, Wuppertal, Germany*
- 177 *Department of Physics, Yale University, New Haven, CT, United States*
- 178 *Yerevan Physics Institute, Yerevan, Armenia*
- 179 *Centre de Calcul de l’Institut National de Physique Nucléaire et de Physique des Particules (IN2P3), Villeurbanne, France*

- a* Also at Department of Physics, King's College London, London, United Kingdom.
- b* Also at Institute of Physics, Azerbaijan Academy of Sciences, Baku, Azerbaijan.
- c* Also at Novosibirsk State University, Novosibirsk, Russia.
- d* Also at Particle Physics Department, Rutherford Appleton Laboratory, Didcot, United Kingdom.
- e* Also at TRIUMF, Vancouver, BC, Canada.
- f* Also at Department of Physics, California State University, Fresno, CA, United States.
- g* Also at Department of Physics, University of Fribourg, Fribourg, Switzerland.
- h* Also at Tomsk State University, Tomsk, Russia.
- i* Also at CPPM, Aix-Marseille Université and CNRS/IN2P3, Marseille, France.
- j* Also at Università di Napoli Parthenope, Napoli, Italy.
- k* Also at Institute of Particle Physics (IPP), Canada.
- l* Also at Department of Physics, St. Petersburg State Polytechnical University, St. Petersburg, Russia.
- m* Also at Chinese University of Hong Kong, China.
- n* Also at Louisiana Tech University, Ruston, LA, United States.
- o* Also at Institutio Catalana de Recerca i Estudis Avancats, ICREA, Barcelona, Spain.
- p* Also at Department of Physics, The University of Texas at Austin, Austin, TX, United States.
- q* Also at Institute of Theoretical Physics, Iliia State University, Tbilisi, Georgia.
- r* Also at CERN, Geneva, Switzerland.
- s* Also at O Chadai Academic Production, Ochanomizu University, Tokyo, Japan.
- t* Also at Manhattan College, New York, NY, United States.
- u* Also at Institute of Physics, Academia Sinica, Taipei, Taiwan.
- v* Also at LAL, Université Paris-Sud and CNRS/IN2P3, Orsay, France.
- w* Also at Academia Sinica Grid Computing, Institute of Physics, Academia Sinica, Taipei, Taiwan.
- x* Also at Laboratoire de Physique Nucléaire et de Hautes Energies, UPMC and Université Paris-Diderot and CNRS/IN2P3, Paris, France.
- y* Also at School of Physical Sciences, National Institute of Science Education and Research, Bhubaneswar, India.
- z* Also at Dipartimento di Fisica, Sapienza Università di Roma, Roma, Italy.
- aa* Also at Moscow Institute of Physics and Technology State University, Dolgoprudny, Russia.
- ab* Also at Section de Physique, Université de Genève, Geneva, Switzerland.
- ac* Also at International School for Advanced Studies (SISSA), Trieste, Italy.
- ad* Also at Department of Physics and Astronomy, University of South Carolina, Columbia, SC, United States.
- ae* Also at School of Physics and Engineering, Sun Yat-sen University, Guangzhou, China.
- af* Also at Faculty of Physics, M.V. Lomonosov Moscow State University, Moscow, Russia.
- ag* Also at National Research Nuclear University MEPhI, Moscow, Russia.
- ah* Also at Institute for Particle and Nuclear Physics, Wigner Research Centre for Physics, Budapest, Hungary.
- ai* Also at Department of Physics, Oxford University, Oxford, United Kingdom.
- aj* Also at Department of Physics, Nanjing University, Jiangsu, China.
- ak* Also at Institut für Experimentalphysik, Universität Hamburg, Hamburg, Germany.
- al* Also at Department of Physics, The University of Michigan, Ann Arbor, MI, United States.
- am* Also at Discipline of Physics, University of KwaZulu-Natal, Durban, South Africa.
- an* Also at University of Malaya, Department of Physics, Kuala Lumpur, Malaysia.
- * Deceased.